Characterization of Silicon Photomultiplier Readout Designs for Use in Positron

Emission Tomography Systems

by

Chen-Yi Liu

A thesis submitted to the Faculty of Graduate Studies of

the University of Manitoba

in partial fulfillment of the requirements of the degree of

MASTER OF SCIENCE

Department of Physics and Astronomy

University of Manitoba

Winnipeg, Manitoba, Canada

II

Abstract

Geiger-mode avalanche photodiodes, or silicon photomultipliers, are promising light sensors for the next generation Positron Emission Tomography (PET) scanners. The sensor is being used in the scanner's gamma ray detector to measure scintillation light. This thesis describes the test results of three gamma ray detectors that utilize silicon photomultipliers. The first one is a commercial detector, and the other two are custom made. The detectors are tested for their 511 keV photon energy and timing resolution, as well as their ability to measure light from small scintillator crystals. The two custom made detectors had smaller active area, but outperformed the commercial detector in energy resolution. The introduction of buffer amplifiers improved the timing resolution of one detector. All three detectors had their crystal decoding ability limited by signal multiplexing and the sensor's dark noise. Finally, a detector design was proposed for the PET system being developed in our group.

Acknowledgment

Table of Contents

VIII

List of Figures

XII

XVI

discriminator (CFD). The CFD produces at its output a trigger pulse when the input pulse reaches a certain fraction of its maximum amplitude. Although the pulses shown here have a negative polarity, it is customary to call the leading edge the 'rising' edge, and the tail part the 'falling' edge.

1   Introduction

Silicon Photomultipliers (SiPMs), also known as Geiger-mode avalanche photodiodes, have gained popularity recently in the field of nuclear medicine imaging. The SiPM is a semiconductor based high sensitivity photon sensor. It is seen as the successor to the photomultiplier tube, which until now has enjoyed many decades of near monopoly as the photo detector used in radioisotope imaging.

The SiPM is superior to the photomultiplier tube in several ways. Among them is its tolerance of strong magnetic fields up to several Tesla. Unlike photomultiplier tubes, the charge carriers in SiPM only travel a very short distance, basically the thickness of the diode, which is a distance too small for the Lorentz force to have an effect on the performance of SiPM. With this interesting feature it is possible to integrate Positron Emission Tomography (PET) with Magnetic Resonance Imaging (MRI) to form a combined system commonly known as PET/MRI.

A complete PET system, be it with MRI or not, will consist of hundreds of these SiPMs. In a system with this many detectors, it is essential to use some form of multiplexing to reduce the number of channels digitized. While many multiplexing techniques can be immediately borrowed from photomultiplier based scanners, multiplexing signals from SiPMs does present its own set of challenges. The purpose of this project is to characterize the performance of three multiplexing techniques when applied to SiPM signals.

In chapter 2, readers will find background information related to this project. The first part of the project evaluates the performance of a commercial detector system that uses a

unique multiplexing strategy. A description of the system as well as the results of the evaluation can be found in Chapter 3 of this thesis. Chapter 4 describes a multiplexing circuit board that was designed and built as part of this thesis project and the subsequent performance measurements done. After the evaluation of the first circuit board, a second version of the multiplexing circuit was designed and built that incorporated some modifications aimed at improving its performance. The description of this second circuit board and the results of the evaluation are summarized in Chapter 5. Chapter 6 summarizes the findings in this project and discusses possible future directions.

2 Background Information

2.1 Introduction to PET imaging

2.1.1 Concept of radiotracer imaging

Positron Emission Tomography (PET) is an imaging modality in nuclear medicine. To perform the scan, a radiotracer is injected into the test subject and the emissions from the radioactive decay are detected by the PET system to determine the biodistribution of the radiotracer. The radiotracer in PET contains a positron emitting isotope which decays through the emission of a positron. Shortly after the release, the positron will annihilate with an electron to produce a pair of 511 keV annihilation photons travelling nearly antiparallel to each other (Figure 2-1). By detecting these two annihilation photons, the PET system produces a map of the distribution of the tracer.
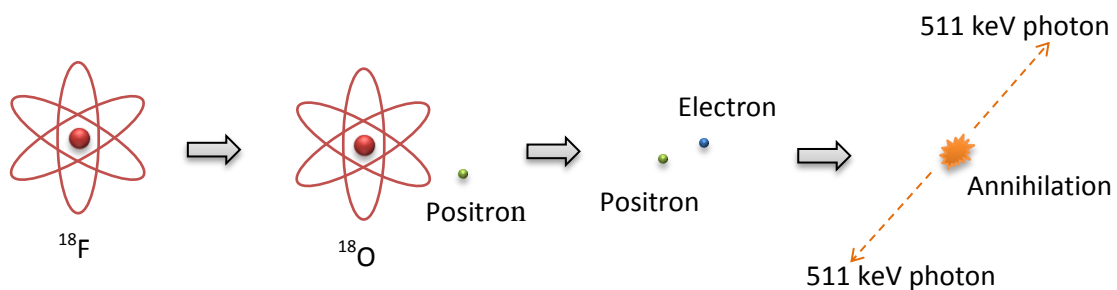
Figure 2-1 Radioactive decay through the emission of a positron and the subsequent positron-electron annihilation.

Some of the isotopes that can be used for PET include ^{11}C, ^{13}N, ^{15}O, and ^{18}F [1]. These isotopes can be integrated into a molecule designed to probe a specific feature in an organism. One example of these tracer molecules is fluorodeoxyglucose labelled with ^{18}F (^{18}F-FDG). FDG is a glucose analogue and can be used to measure glucose metabolism of an organ in the body [2].

2.1.2 PET/MRI

The advantage of PET over other diagnostic imaging modalities is its ability to measure physiological functions with very high sensitivity. In addition to the glucose metabolism mentioned above, biological processes such as ligand-receptor binding and gene expression can also be measured with PET [3][4]. The sensitive nature of the radiation detector allows PET to measure molecular concentrations down to a nanomolar scale [5]. Therefore, a change in physiological function can be measured with very little amount of tracer.

However, PET is not designed to image the anatomical structure of the body. To obtain structural images, people often turn to x-ray, Computed Tomography (CT) or Magnetic Resonance Imaging (MRI). Combined PET/CT scanners are very well established nowadays, but PET/MRI systems are less common. As a combined system, the PET component will augment the wide range of applications available from MRI [6].

2.1.3 PET system design

To detect the 511 keV annihilation photons, a PET system is built up of an array of gamma ray detectors. One way to arrange these detectors is to put them in a hollow cylinder within which the test subject can be placed (Figure 2-2). This arrangement facilitates the simultaneous capture of the pair of 511 keV photons from the positron-electron annihilation.
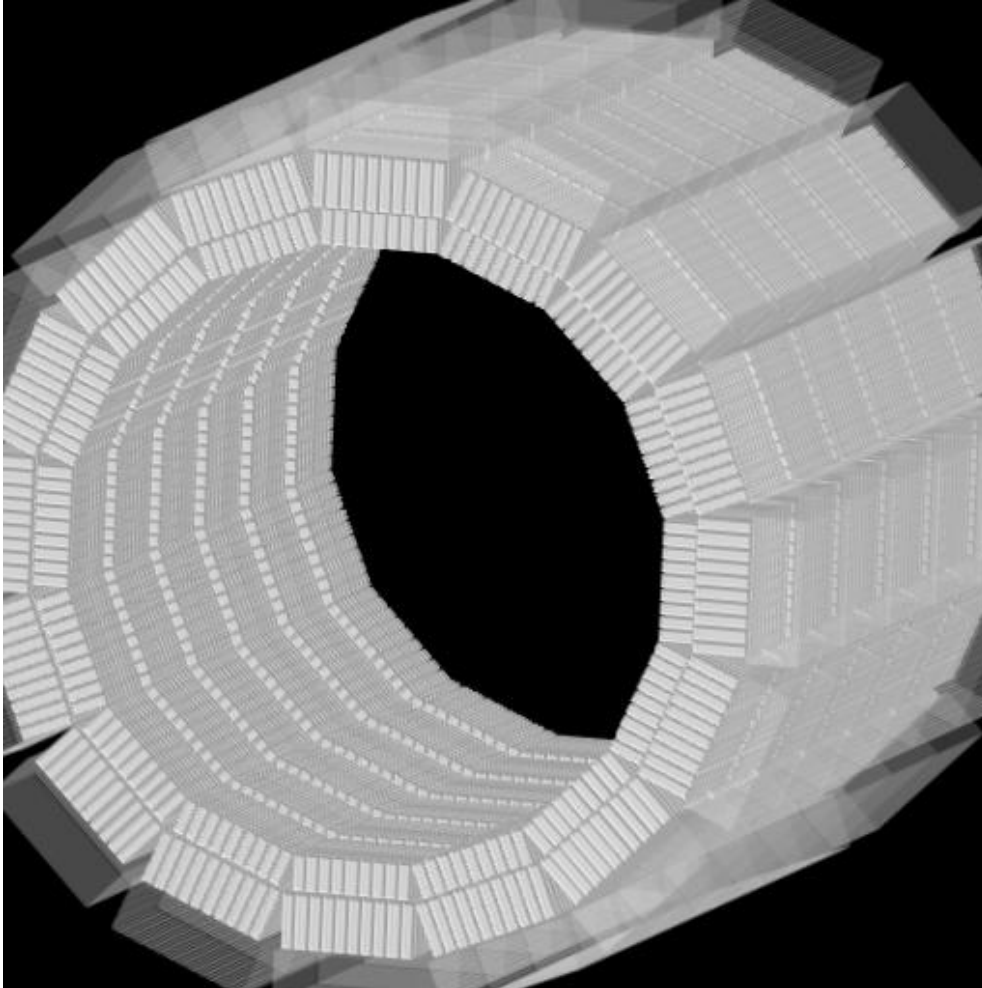
Figure 2-2 The gamma ray detectors in a PET system are often arranged in a hollow cylindrical form. In this drawing, there are 16 detector modules in a ring, and there are 6 rings in total. The white rectangles in the two inner layers represent the scintillator crystals, and the semi-transparent boxes on the outer layer represent the light detector. The object to be imaged, not shown here, will be placed inside the cylinder. (Drawing provided by Dr. Xuezhu Zhang)

The coincidence electronics in the system compares the arrival time of all 511 keV photons (Figure 2-3). If any two photons arrive within a short time period of each other, the electronics will designate this as a valid coincidence event. After collecting multiple annihilation events from all pairs of detectors, the computer produces a three dimensional image of the distribution of the radiotracer.
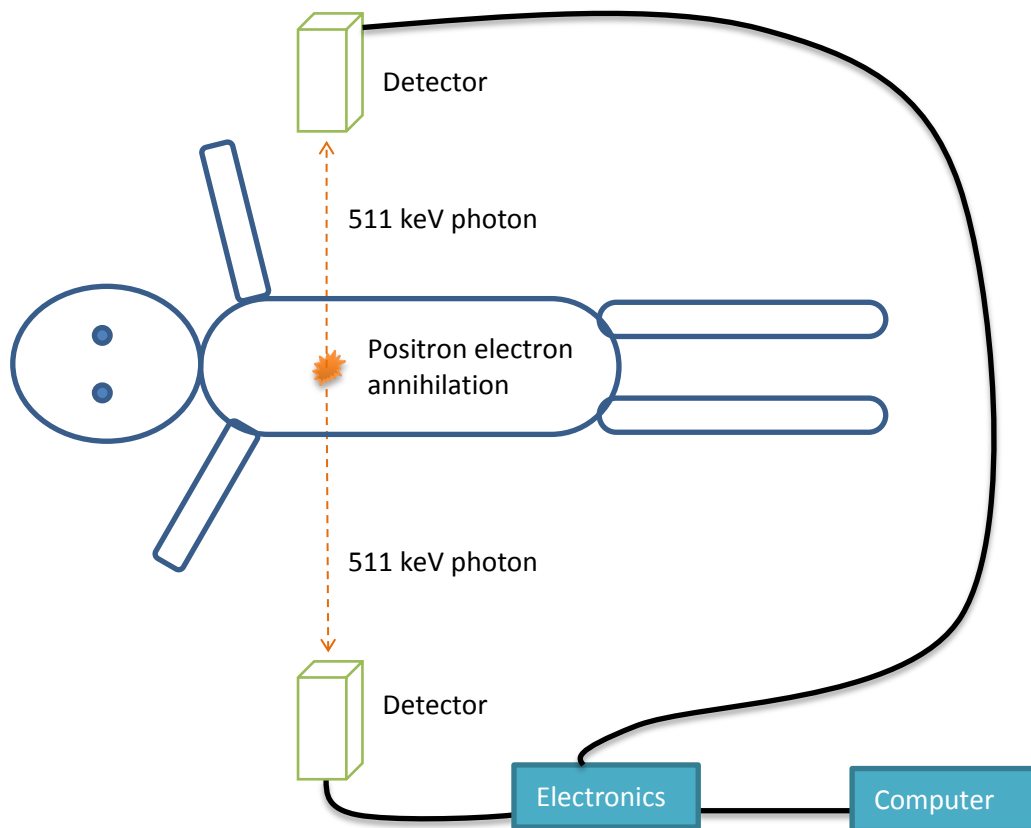
Figure 2-3 Two detectors capture the pair of 511 keV photons from the positron-electron annihilation in the test subject.

2.1.4 Event types in PET

There are three basic event types in PET: trues, scatters, and randoms. In a true event, the pair of 511 keV photons are captured by detectors on opposite sides of the hollow cylinder (Figure 2-4). The PET system determines a line of response (LOR) based on the location of these two detectors. In a scatter event, the 511 keV photon may scatter off an electron while travelling out of the test subject. The scattered photon can reach a detector along the deflected path, resulting in an LOR mispositioned from the true LOR. The third event type, random coincidence, occurs when the system detects two 511 keV photons from two separate annihilations. The resulting LOR is also not representative of the distribution of the radiotracer.

6
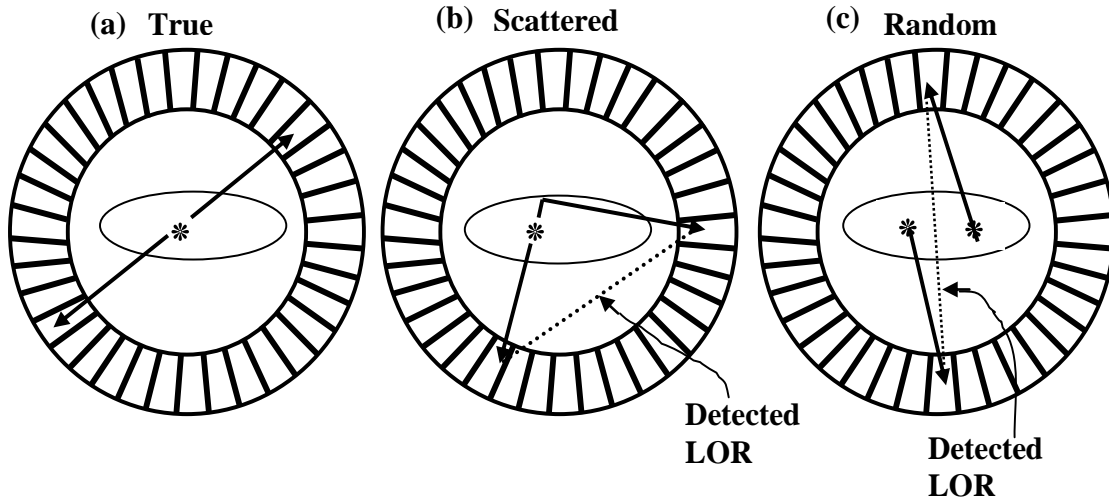
Figure 2-4 (a) The two 511 keV photons fly in opposite directions. (b) When a photon is scattered before reaching the detector, the LOR no longer yields the correct location of the radiotracer. (c) The LOR of a random coincidence. (Figure courtesy of Dr. Fazal Ur-Rehman)

2.2 Detectors for PET imaging

2.2.1 Overview of scintillation detectors

A PET detector is usually made of a scintillator crystal coupled to a light sensor. The purpose of the scintillator crystal is to convert the annihilation photon energy into visible light (Figure 2-5). Since the light produced by the scintillator is quite faint, a very sensitive light sensor is needed. A commonly used light sensor is the photomultiplier tube. However, since photomultiplier tubes do not work well in the presence of strong magnetic fields like those found in a Magnetic Resonance Imaging (MRI) scanner, solid state sensors such as SiPMs are a better alternative when building a combined PET/MRI system [7][8]. Thus the detector under investigation in this project will be made up of scintillator crystals coupled to silicon photomultipliers (SiPMs).
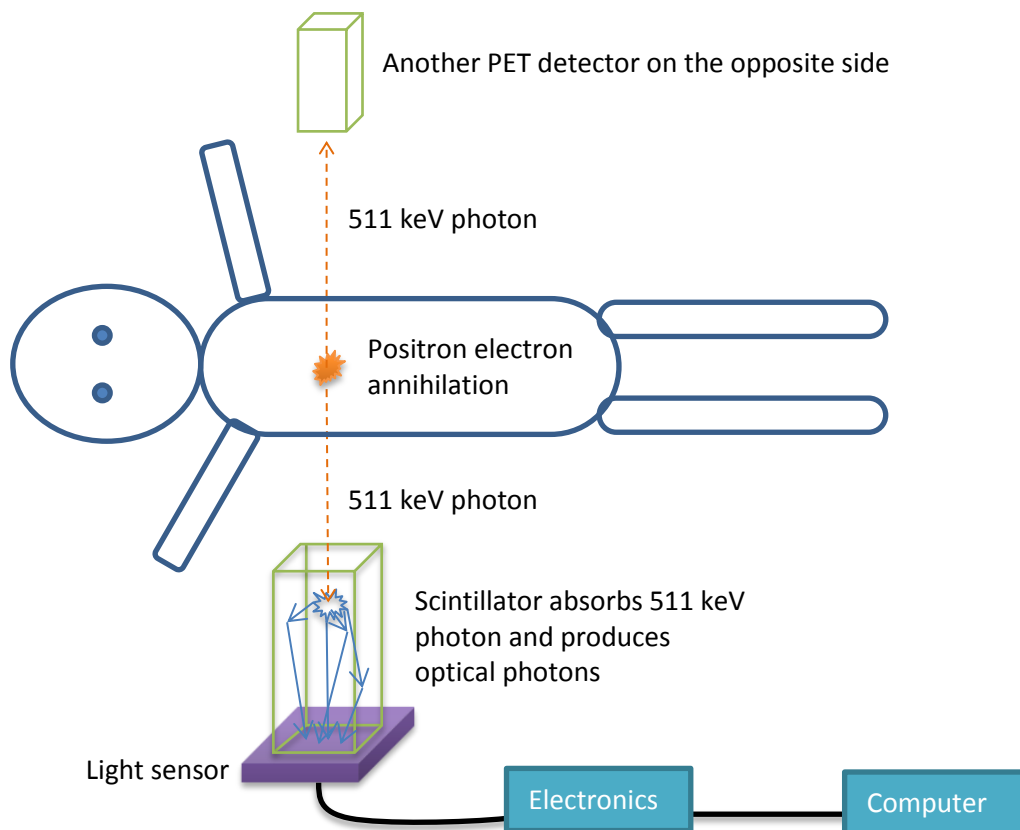
Figure 2-5 The interaction of the 511 keV photon with the scintillator crystal generates a flash of visible light.

2.2.2 Photon interactions in matter

The detection of the 511 keV photon relies on its interaction with a material. For high energy photons such as a 511 keV photon, the two principle modes of interaction with matter is through the photoelectric effect and Compton scattering [5].

A photoelectric interaction occurs when the entire energy of the photon is given to an inner shell electron of an atom. The energy is used to eject this electron from the atom [5]. Deprived of its energy, the photon disappears.

8

Compton scattering is the collision of the photon with a free electron in the material [5]. In the collision process, the photon transfers part of its energy to the electron and gets deflected.

In materials of low atomic number, it is more likely that Compton scattering will occur than the photoelectric effect. The electrons are loosely bound to the nucleus, lending themselves available for Compton scattering. For materials with high effective atomic number, there are more bound electrons and the photoelectric effect dominates. Because the photoelectric effect is a complete absorption of the photon energy, it is the preferred mode of interaction in the detection of gamma rays. We want to capture the entire gamma photon and measure its energy. Thus, in choosing a scintillator, we want to use one that contains high atomic weight elements. Some of the elements used in high energy photon scintillator include iodine, caesium, lanthanum, gadolinium, lutetium, and bismuth.

2.2.3   Scintillators for PET imaging

When the annihilation photon interacts with the scintillator crystal, by photoelectric absorption or Compton scattering, the interaction excites electrons in the crystal lattice from the valence band to the conduction band (Figure 2-6). The resulting electrons drift in the lattice until they encounter an activator site, typically a trace element doped in the crystal. At the activator site the electrons fall through the transition states of the doped element and, in the process, emit optical photons [9]. The more energy the high energy photon deposits in the crystal, the more electrons are bumped to the conduction band and more optical photons are released from the crystal. Therefore, one can measure, based on the brightness of this scintillation light, the energy deposited by the high energy photon.

Conduction band

Excited
states
(impurity)

Forbidden
Energy Gap

Scintillation
photon

Ground state
(impurity)
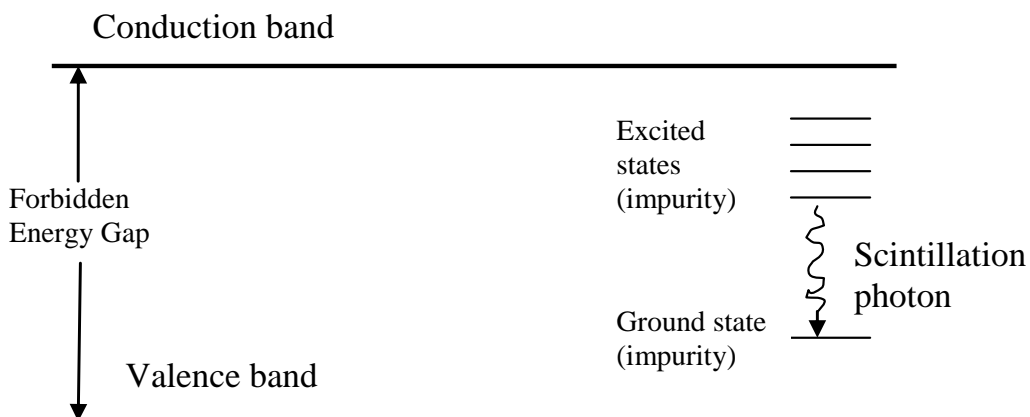
Valence band

Figure 2-6 After the electrons are pumped to the conduction band, they travel to an impurity site to fall back to the valence band. As they fall, they release optical photons. (Figure courtesy of Dr. Fazal Ur-Rehman)

Sometimes the gamma photon may deposit only part of its energy through Compton scattering with an electron in the crystal. When this happens, less energy is converted to optical photons. The light sensor measures a weaker light signal than for a full energy deposition event. This phenomenon accounts for the lower energy events that appear in the energy spectrum of the 511 keV photon.

There are several scintillators that can be used to detect 511 keV photons. Scintillators that can be used include NaI:Tl, $Bi_4Ge_3O_{12}$, Lu_2SiO_5:Ce, $(Lu_{1-x}Y_x)_2SiO_5$:Ce, $LaBr_3$:Ce [9][10][11]. These scintillators differ in their density, effective atomic number, light yield per MeV of gamma photon, peak emission wavelength, and scintillation decay time.

The scintillator crystal of our choice is cerium doped lutetium yttrium oxyorthosilicate, $(Lu_{1-x}Y_x)_2SiO_5$:Ce, (LYSO:Ce). It is suitable for use in PET because of its high density (7.2g/cm^3), which is good for stopping the 511 keV photon [12]. LYSO is also relatively efficient at converting a gamma photon to optical photons. Approximately 12000 visible light photons are created from a single 511 keV photon [12]. Lastly, the scintillation decay time is short (42ns), allowing imaging at a very high count rate and

10

with good timing resolution, both of which are favourable characteristics in a PET system

[12]. Figure 2-7 is a photograph of an LYSO crystal.
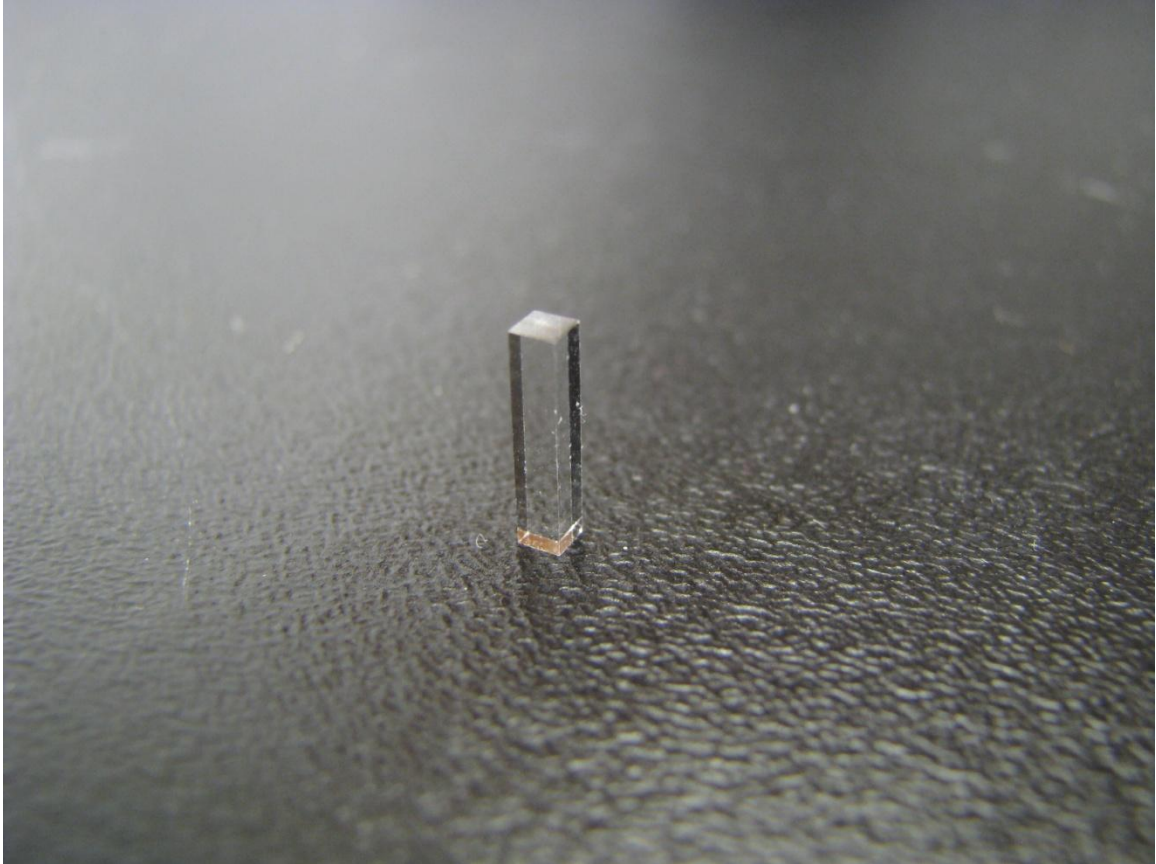
Figure 2-7 An LYSO scintillator crystal. The dimensions of this crystal are 2 mm × 2 mm × 10 mm.

2.2.4 Photodetectors for PET

2.2.4.1 Photomultiplier Tube

Photomultiplier tubes are very sensitive light detectors. They consist of a

photocathode, a series of dynodes, and an anode. The photocathode detects an optical

photon and ejects an electron through the photoelectric effect [5]. The dynodes use an

electric potential to accelerate the photoelectron to very high speed, so that the impact of

the photoelectron on the following dynode will create even more electrons. In the cascade of electrons through the dynode chain, the original photoelectron is multiplied. By the time the electron cloud reaches the anode, there will be roughly $10^6 - 10^7$ electrons for each initial photoelectron, giving a strong current pulse at the output of the photomultiplier tube. Because the electrons fly from one dynode to the next in the vacuum tube, their flight trajectories change in the presence of a strong magnetic field, rendering the photomultiplier tube inoperable.

2.2.4.2 Avalanche Photodiode

In addition to photomultiplier tubes, photodiodes can be used to detect visible light. Conventional photodiodes rely on the photon energy to create electron-hole pairs in the semiconductor crystal and then output the charge. The signal, therefore, is rather weak. The avalanche photodiode is designed to mitigate this weak signal problem. When a high voltage is applied to an avalanche photodiode, the photon generated electron-hole pairs are accelerated by the high electric field in the semiconductor [9]. In the acceleration process, the charge carriers collide with other electrons to create even more charge carriers. Thus, the output signal from an avalanche photodiode is much larger than that of a conventional photodiode. The gain of the avalanche photodiode is about 10^3 [13].

2.2.4.3 Silicon photomultiplier (SiPM), Geiger-Mode Avalanche Photodiode

Geiger-mode avalanche photodiodes, commonly called silicon photomultipliers (SiPMs), are being investigated for PET applications due to their favourable characteristics. SiPMs are better than avalanche photodiodes in several ways, including high gain ($10^5 - 10^7$), good timing performance, and low operating bias voltage [14]. The

insensitivity of SiPMs to strong magnetic fields also allows the integration of PET and MRI [15].

A single SiPM is made up of many, up to several thousand, Geiger-mode avalanche photodiodes as microcells. The size of a microcell can be as small as 20×25 μm^2 to as large as 70×70 μm^2 [16]. These microcells are biased with a voltage that is above the breakdown voltage of the photodiode. When an optical photon hits an individual microcell, it generates a photoelectron which in turn initiates a Geiger discharge in that cell. A Geiger discharge is an avalanche current having the same magnitude regardless of the number of the initial photoelectrons. Since all the microcells are connected in parallel, the output signal of a SiPM is proportional to the number of microcells that fire. When the number of incoming optical photons is low, then the number of microcells firing is proportional to the number of incident photons. Because of this, some SiPM manufacturers market their products as photon counters. The relationship between the number of firing microcells, N_{fired}, and the number of incident photons, N_{photon}, can be described by the equation [14]

$$N_{fired} = N_{total} \times (1 - e^{\frac{-N_{photon} \times PDE}{N_{total}}}) \quad . \qquad (2.1)$$

Here N_{total} is the total number of microcells that are exposed to the crystal, and PDE is the photon detection efficiency of the sensor. The relationship between N_{fired} and N_{photon} is roughly linear when $N_{photon} \times PDE \ll N_{total}$, but becomes nonlinear when the light beam gets more intense, i.e. when multiple photons strike a single microcell at any given time. Then the SiPM becomes saturated. Therefore, the SiPM is better suited for detecting low intensity light sources and not bright ones. Care must be taken when

measuring scintillation light to ensure the SiPM does not saturate. Or if one desires, a calibration of signal amplitude vs. gamma ray energy can be made to compensate for the saturation effect.

Unfortunately, the SiPM does have some shortcomings. In the absence of light, the microcells in a SiPM will spontaneously fire due to thermally generated charge carriers in the sensitive region of the semiconductor. This dark firing rate can be a few MHz per mm^2 of detector surface area at room temperature and increases with temperature [15]. The rate also increases with the bias voltage on the diode, as stronger electric fields make the spontaneous generation of charge carriers more likely to happen. The disadvantage of this dark firing current is that it hinders one from using a SiPM to detect a single photon, as one cannot tell whether the signal is coming from a photon or from a spontaneously generated charge carrier. This is less of a concern in PET as a scintillation event produces enough photons to outnumber the thermal electrons. Thus, the output signal is proportional to the intensity of the scintillation light. Alternatively, one can cool the SiPM to reduce the magnitude of the dark current.

Another characteristic of SiPMs is that the gain varies with temperature and bias voltage [17]. The gain of a SiPM depends on the overbias voltage, which is the difference between the applied voltage and the breakdown voltage of the SiPM, $V_{overbias} = V_{applied} - V_{breakdown}$. As the breakdown voltage of a p-n junction increases with temperature, the overbias voltage actually drops [18]. This is something that can affect the performance of a SiPM, and a calibration curve can be calculated to predict the performance under different temperatures and bias voltages. Alternatively, one can monitor the temperature

and continuously adjust the applied bias voltage to ensure that the over bias voltage stays

constant [17].

There are multiple vendors of SiPMs. One company that manufactures and sells

SiPMs is the company SensL in Cork, Ireland. One of their products, and the one used in

this project, is the SPMArray4 (Figure 2-8). The SPMArray4 is a packaged

semiconductor device containing a 4×4 array of SiPMs; each SiPM pixel is 3.17 mm $\times$

3.17 mm consisting of 3640 microcells with 35µm cell size. There are 20 pins on the

back side of this chip – 16 pins are the signal outputs of the 16 SiPMs, and 4 pins are the

bias voltage lines for each row of SiPM. There is a <0.5mm thick epoxy covering the

SiPMs on the front to protect the sensors and to provide a smooth surface for coupling to

scintillator crystals (Figure 2-9). SensL recommended a bias voltage of 30.2 V for this

particular product.
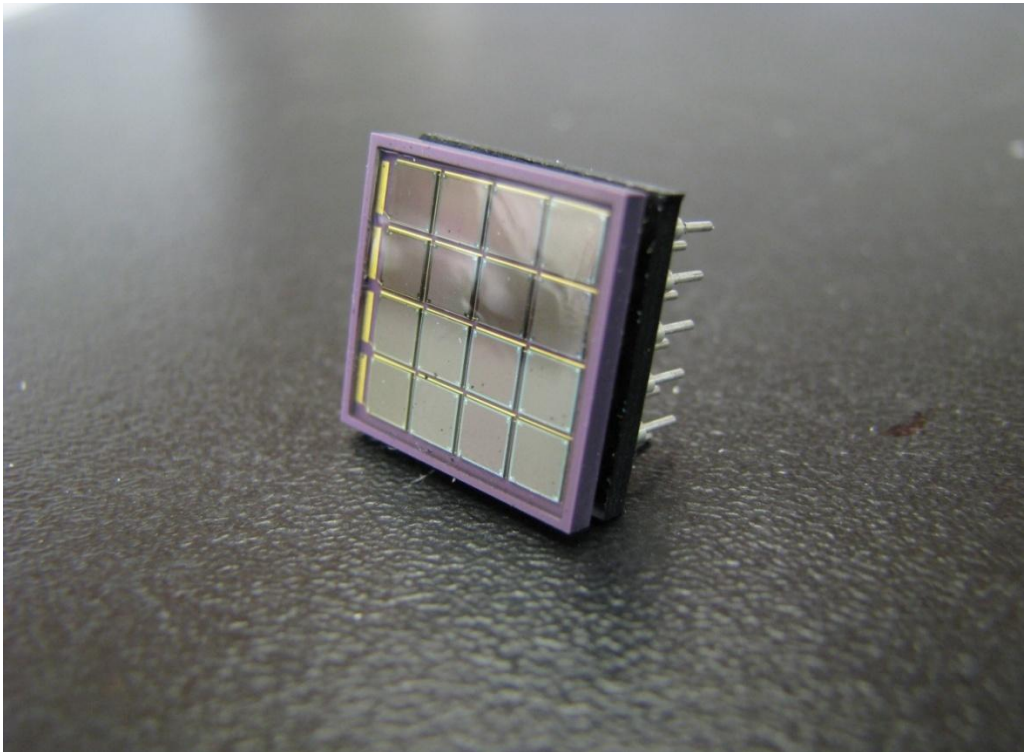
Figure 2-8 The SensL SPMArray4, consisting of a 4 × 4 array of SiPMs.
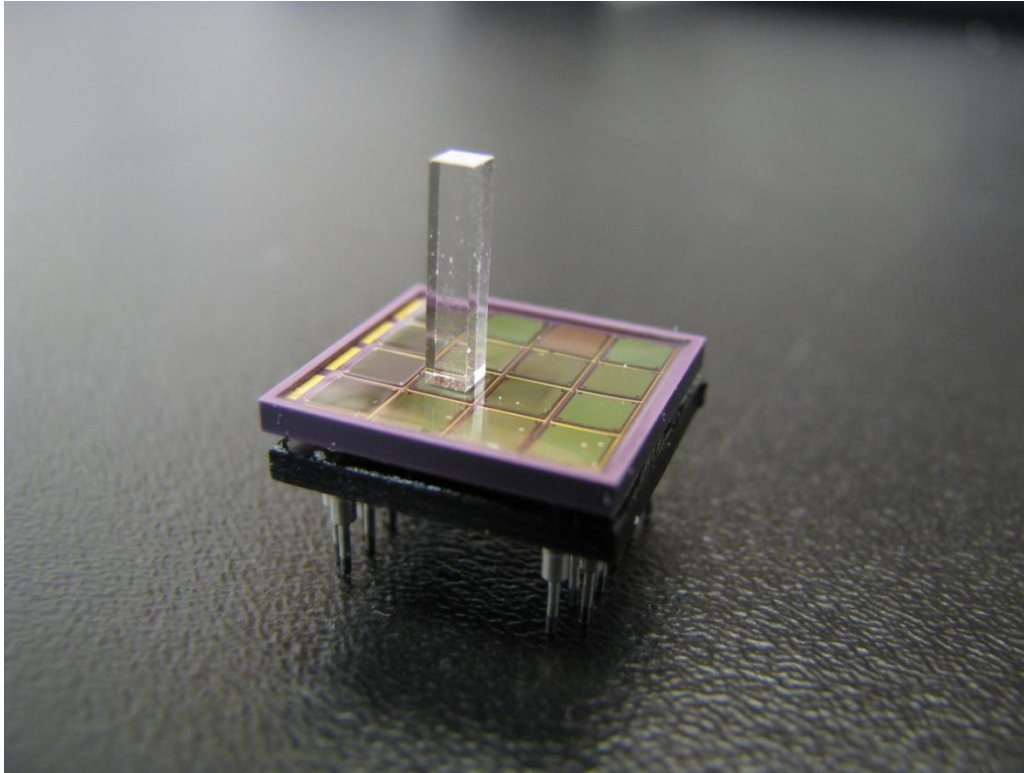
Figure 2-9 An LYSO crystal sitting on top of one SiPM in the SensL SPMArray4.
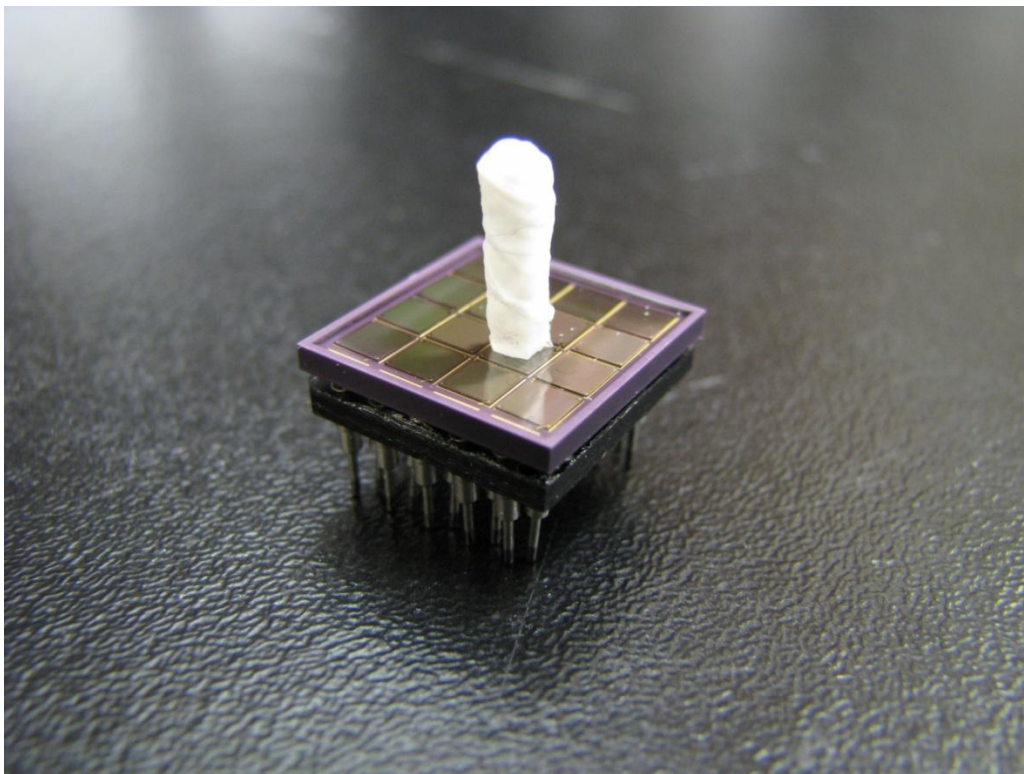
Figure 2-10 The crystal is wrapped in a reflective material (Teflon) on all sides that are not touching the SiPM. The reflector traps the scintillation light so that all the light will go towards the SiPM.

16

Since only one side of the rectangular crystal is coupled to the SiPM, it is common to attach reflective material to all other sides of the crystal to concentrate light towards the SiPM. Figure 2-10 shows a crystal wrapped in white Teflon tape.

Figure 2-11 gives an example of the shape of the SiPM signal when reading out a LYSO scintillator crystal. The output current from the SiPM is converted to a voltage signal by a 50Ω resistor to ground. The pulse peak amplitude correlates with the intensity of the light produced by the scintillator. The pulses have a rise time of around 50 ns and a decay time of around 350 ns.
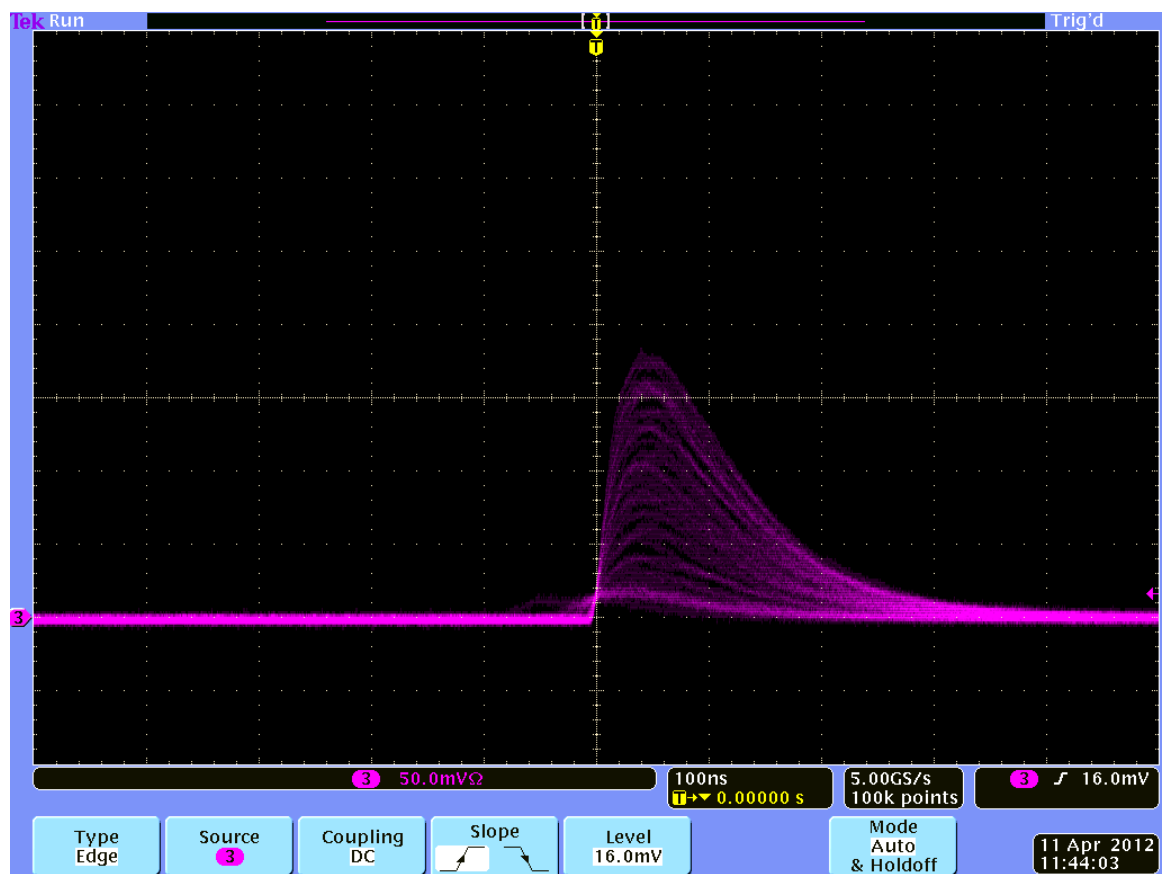
Figure 2-11 Example of SiPM signals when reading out the light from an LYSO scintillator. This snapshot shows pulses of different heights superimposed on one another. The signal is amplified with a non-inverting op-amp with a gain of one.

2.3 Detector performance

2.3.1 Introduction

The performance of the gamma ray detector ultimately determines the quality of the PET image. The three performance measures we are interested in are energy resolution, timing resolution, and spatial resolution.

2.3.2 Energy resolution

The energy resolution of a detector is the precision with which the energy deposited in the crystal can be measured. This is critical because the detector needs to be able to tell whether the incoming gamma photon has been scattered while travelling out of the test subject. A scattered gamma photon travels in a different direction from its original path and so needs to be treated differently by the PET system.

It is possible to identify, by measuring their energy, photons that have been scattered. This is because when a gamma photon scatters off an electron in the test subject, part of the photon's energy is transferred to the electron. Depending on the scattering angle, a different amount of energy is transferred. The energy of the scattered photon is given by the following equation [19].

$$E_{scattered} = \frac{511 \text{ keV}}{2 - \cos\theta} \tag{2.2}$$

In this equation, $E_{scattered}$ is the energy of the scattered photon, and θ is the angle difference in photon trajectory before and after the scatter (Figure 2-12). A gamma ray detector with a good energy resolution is able to distinguish a photon that has been scattered from one that has not.

18

Scattered γ-photon = hύ

Incident γ-photon = hυ

θ

φ

Recoil electron
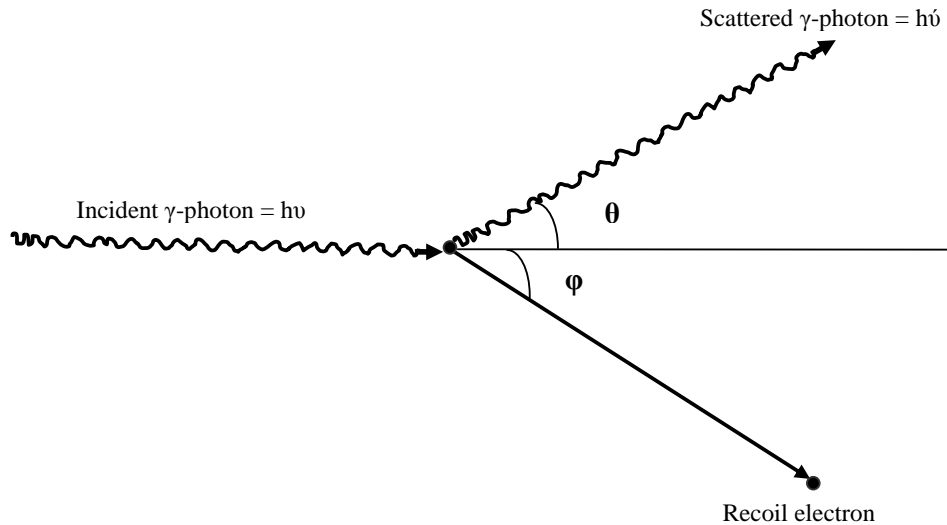
Figure 2-12 In Compton scattering, the photon transfers some of its energy to the electron. Conservation of momentum requires the photon to change direction. (Figure courtesy of Dr. Fazal Ur-Rehman)

The energy resolution of a detector is measured by obtaining an energy spectrum of the 511 keV photon. For an ideal detector with perfect energy resolution, the spectrum is a sharp delta function-like peak at 511 keV (Figure 2-13). However, it is also possible that some of the 511 keV photons will go through Compton scattering instead of photoelectric absorption inside the scintillator crystal, thus depositing only a fraction of its energy in the crystal. This phenomenon accounts for the lower energy events that appear in the energy spectrum of the 511 keV photon. The energy spectrum is therefore made up of a photopeak at 511 keV and a broad Compton plateau at the low energy end of the spectrum.

19
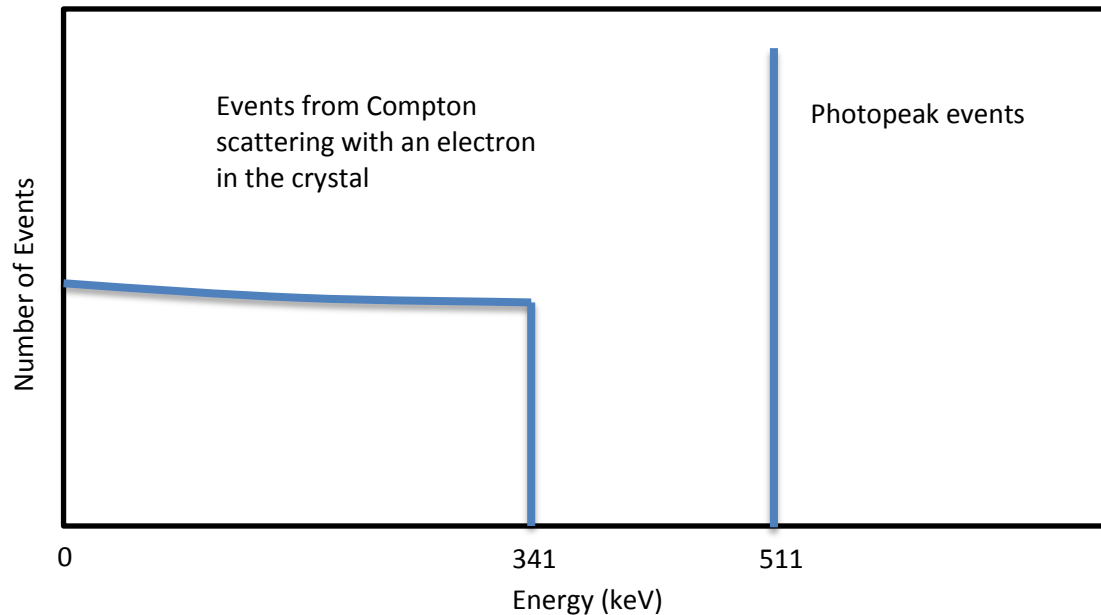
Figure 2-13 This diagram shows how the energy spectrum of the 511 keV photon would appear if the energy resolution were a perfect 0%. The photopeak would be a sharp delta function at 511 keV, which contains all the events when the entire energy of the gamma photon is deposited in the scintillator crystal. If the photon deposits only part of its energy by going through Compton scattering with an electron in the crystal, the events would fall in the Compton curve running from 0 to 341 keV, the minimum and maximum amount of energy a photon can impart on an electron through one scatter. It is possible for a gamma photon to undergo multiple Compton scatters and this accounts for the extension of the Compton region toward 511 keV in a real spectrum.

For several reasons, the 511 keV photopeak measured by a scintillator detector is not a sharp peak. The first reason is that the scintillator crystal has limited conversion efficiency. The number of optical photons produced by the scintillator crystal is not the same every time for a given gamma photon energy, thus contributing uncertainty to the measured energy value. In addition, not every photon produced by the scintillator is detected by the light sensor. Some of them are absorbed by the scintillator crystal itself; others may be absorbed by the packaging material of the light sensor. The sensor also has a photon detection efficiency of less than 100%. All these factors are subject to statistical fluctuation. As a result, the output signal of the light sensor has slightly different

20

amplitude each time a 511 keV photon is detected. If we plot the distribution of the signal amplitude of the 511 keV photon, we will get a Gaussian shaped distribution instead of a delta function (Figure 2-14).

The energy resolution of a gamma ray detector is defined as the full-width-at-half-maximum of the photopeak divided by the peak position:

$$Energy\ resolution\ (\%) = \frac{\Delta E}{E},\qquad\qquad(2.3)$$

where ΔE is the full-width-at-half-maximum of the peak, and E is the peak position. The value is usually less than one and is often reported as a percentage. If we assume that the number of detected optical photons follows a Poisson distribution, ΔE increases as $\sqrt{E}$. Therefore, the energy resolution is proportional to $\frac{1}{\sqrt{E}}$. Higher energy gamma photons have a smaller, better value for energy resolution [9]. Since the photon of interest in PET is the 511 keV annihilation photon, the energy resolution reported for a PET detector is normally given at 511 keV.
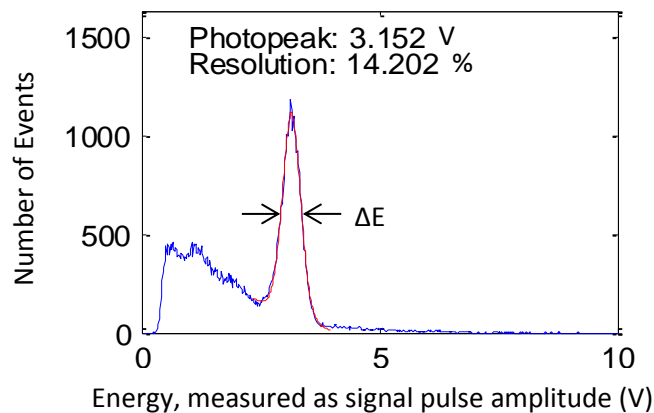
Figure 2-14 A real energy spectrum of the 511 keV photon. The photopeak is highlighted in red.

When measuring the energy resolution of a PET detector, a 511 keV radiation source is placed in front of the detector. Ideally, there will be nothing between the source and the detector so there is very little chance that the gamma photon will be scattered before reaching the detector. As a result, the Compton scattering events observed in the energy spectrum are scattered mainly by electrons in the scintillator crystal.

2.3.3 Timing resolution

The timing resolution of a detector refers to its ability to accurately record the gamma photon arrival time. PET systems rely on simultaneously detecting the two 511 keV photons from a positron-electron annihilation to calculate the distribution of the radiotracer. Therefore, it is crucial for the system to be able to determine among many gamma photons which two come from the same annihilation event. The system achieves this by identifying pairs of 511 keV photons that arrive within a narrow timing window of typically a few nanoseconds. A good timing resolution increases the chance of the system correctly identifying photons from the same annihilation. A poor timing resolution results in more random events being recorded by the system (Figure 2-4 c).

A detector with an ideal timing resolution will be able to measure the precise time the gamma photon arrives at the detector. If we sort all the events in a histogram according their arrival times, the histogram will be a sharp delta-function like peak (Figure 2-15). In a real detector, there is always some uncertainty as to the exact time the gamma photon arrives. When the gamma photon interacts with the scintillator crystal, it takes a while for the crystal to release optical photons, leading to a non-instantaneous signal rise time. The optical photons themselves also spend time travelling and being reflected by the reflective material surrounding the crystal. Once the light sensor captures the optical

22

photons and creates an output signal, there will be some variation in the electronic signal

due to electronic noise in the equipment. The electronics will have a finite bandwidth,

sometimes slowing the rising edge of the pulse. The combination of these factors causes

the detector to have a limited temporal resolution. It has been shown that with low noise

high speed electronics, it is possible to achieve 0.1 ns temporal resolution with LYSO

scintillator crystal coupled to a SiPM [20]. If we again plot the events as a histogram

based on the measured gamma photon arrival time, we would get a Gaussian shaped

temporal response rather than a delta function-like line (Figure 2-16). The timing

resolution is defined as the full-width-at-half-maximum of this temporal response curve,

Δt.
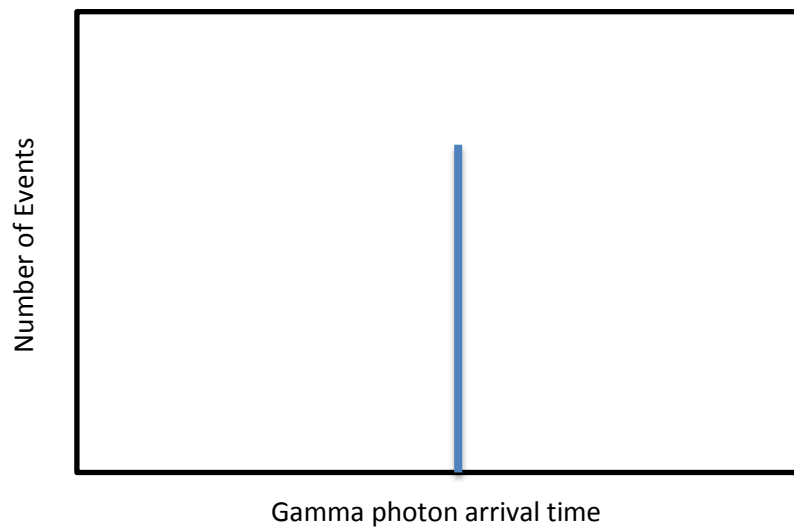
Figure 2-15 An ideal timing spectrum of a detector. The photon arrival time at one detector is always a fixed amount from the arrival time of the other photon at another detector.
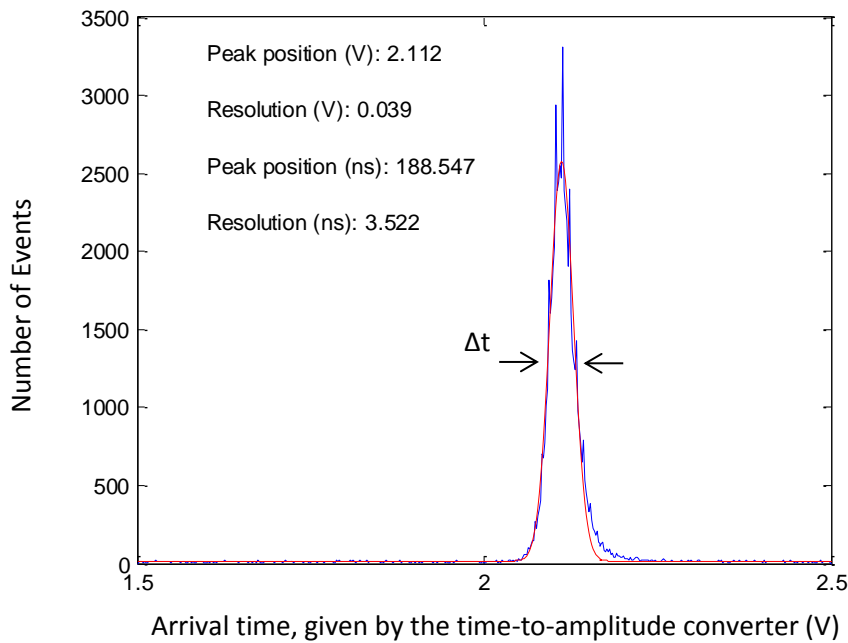
Figure 2-16 A real timing spectrum. The scintillation events are sorted into a histogram based on arrival time. The signal given by the time-to-amplitude converter is an analog voltage pulse, from which we can back calculate the arrival time in nanoseconds.

2.3.4 Spatial resolution

2.3.4.1 Introduction

A PET detector is usually a few centimeters in size. Therefore, to achieve a spatial resolution of a few millimeters or less, the detector needs some mechanism to determine where inside the detector module the gamma photon is captured. There are two primary types of detector structure, monolithic and pixelated. They have different characteristic spatial resolution and will be discussed in the following two sections.

2.3.4.2 Monolithic crystal

When a gamma photon interacts with the crystal, the scintillation light spreads onto multiple light sensors. Depending on the position of interaction, different amounts of

24

light shine on different sensors. Then the light distribution can be used to calculate the

gamma ray interaction position (Figure 2-17).
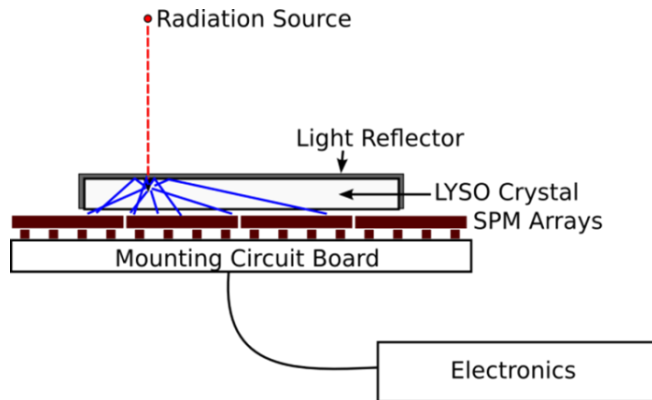
Figure 2-17 The scintillation light falls on the array of SiPM sensors below the crystal. Sensors closest to the location of interaction will receive more light than other sensors will.

2.3.4.3 Pixilated crystals

Sometimes it is also helpful to segment the scintillator crystal into smaller optically

isolated sections to reduce the extent of the light spread. For instance, each section can be

one square millimeter in cross sectional area. By determining which section absorbs the

511 keV photon, the detector module can provide a resolution the same size as the area of

each small section (Figure 2-18).
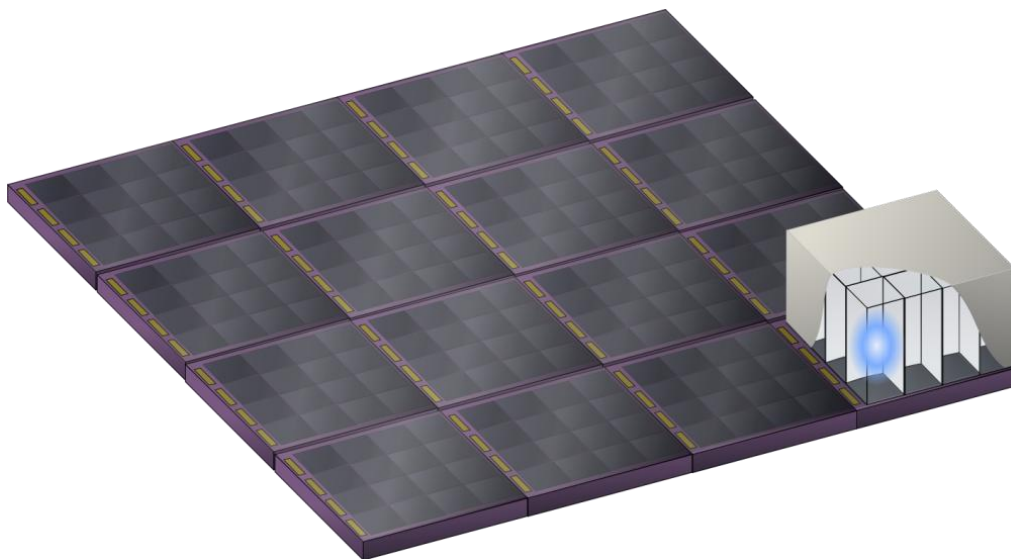
Figure 2-18 A crystal block that is made up of smaller optically isolated elements. The elements can be any size, but in this picture, the crystal element size is designed to be the same as one SiPM pixel. Almost all the light produced by one element will fall on the SiPM directly beneath the crystal. But because of a thin layer of epoxy coating on the surface of the SiPM array, some light will inevitably spread to adjacent SiPMs.

Before a detector can be used, a calibration needs to be done to correlate the detector output signal to the physical location of the pixelated elements. To do that, the detector is uniformly irradiated with a 511 keV source. After collecting the scintillation events of the 511 keV photons, the position of each event is calculated. Based on their positions, the events are sorted into a flood histogram. A flood histogram is a 2D image whose pixel value represents the number of events that occurred at that point. The histogram also nicely demonstrates the detector's ability to distinguish scintillation events that occur in different crystals. A good flood histogram will show distinct clusters of events that correspond to the individual crystal elements in the scintillator block. Figure 2-19 is an example of a good flood histogram showing the 16 clusters of events obtained with a 4×4 array of pixelated crystals. The flood histogram is cut into smaller sections with each section corresponding to a crystal element (Figure 2-20). The segmentation map is stored

in the PET system. During a PET scan, whenever there is a new event, the system will
use the map to determine in which crystal the new event comes from.
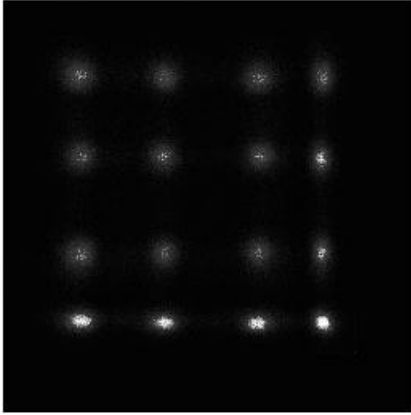
Figure 2-19 An example of a flood histogram of a gamma ray detector based on pixelated crystals. The brightness of the image corresponds to the number of events at that location.
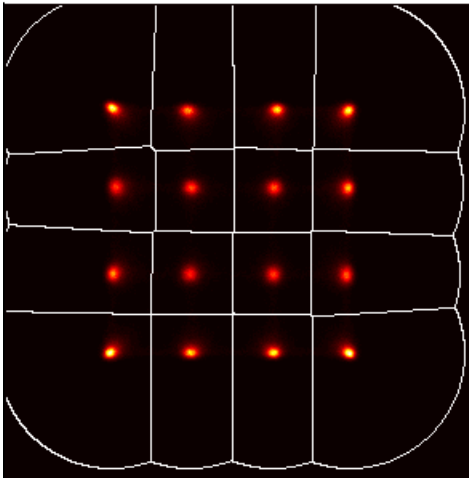
Figure 2-20 A segmented flood histogram.

2.4   Approaches to signal readout

2.4.1   Introduction

A complete PET system will consist of many gamma ray detectors. The total number
of SiPMs in the system can be up to several hundred. It is possible to read the signal from
the SiPMs individually, but the total number of data channels in the system will be large.
This adds complexity and cost. For example, without any multiplexing, a recently built

small animal PET scanner with 13.6 cm ring diameter and 3.2 cm axial field of view will have 768 data channels to process. However, with multiplexing, the system only needs to process 24 channels [21].

2.4.2 No multiplexing

It is possible to build a PET scanner without multiplexing the detector signals. One of the ways to build such a system is to miniaturize the electronic circuitry into an application specific integrated circuit (ASIC). This approach has been described by Llosa et al. who used a custom built ASIC to individually read out 16 SiPMs [22]. Each data channel in the chip consists of a preamplifier, discriminator, and pulse shaper. The advantage of having individual readout is that unlike in a multiplexing method, there will be very little interference between the signals from different SiPMs. On the system level, the scanner will also be able to handle a stronger radioactive source and a higher count rate because the signal from each SiPM is processed simultaneously and independently.

Another advantage of individual readout is that the timing resolution of the gamma ray detector will be better, as signal multiplexing may worsen the timing precision of the detector. According to Seifert et al. the timing resolution of a SiPM based scintillation detector can be as good as 0.1 ns when read out individually [23].

2.4.3 Row/column readout

Even though individual readout gives good timing performance and using an ASIC can significantly reduce the physical size of the electronic system, the number of channels for an entire system is still going to be overwhelmingly large. Therefore, several

groups have experimented with signal multiplexing techniques to reduce the number of readout channels.

One multiplexing method accomplishes this by chaining together the outputs of SiPMs of the same row and column [24][25]. Then the signals from all the rows/columns are summed with differential gains into two op-amps such that the ratio of the two op-amp outputs is determined by which row/column the signal comes from, and the sum of these two signals is the amplitude of the original pulse (Figure 2-21).
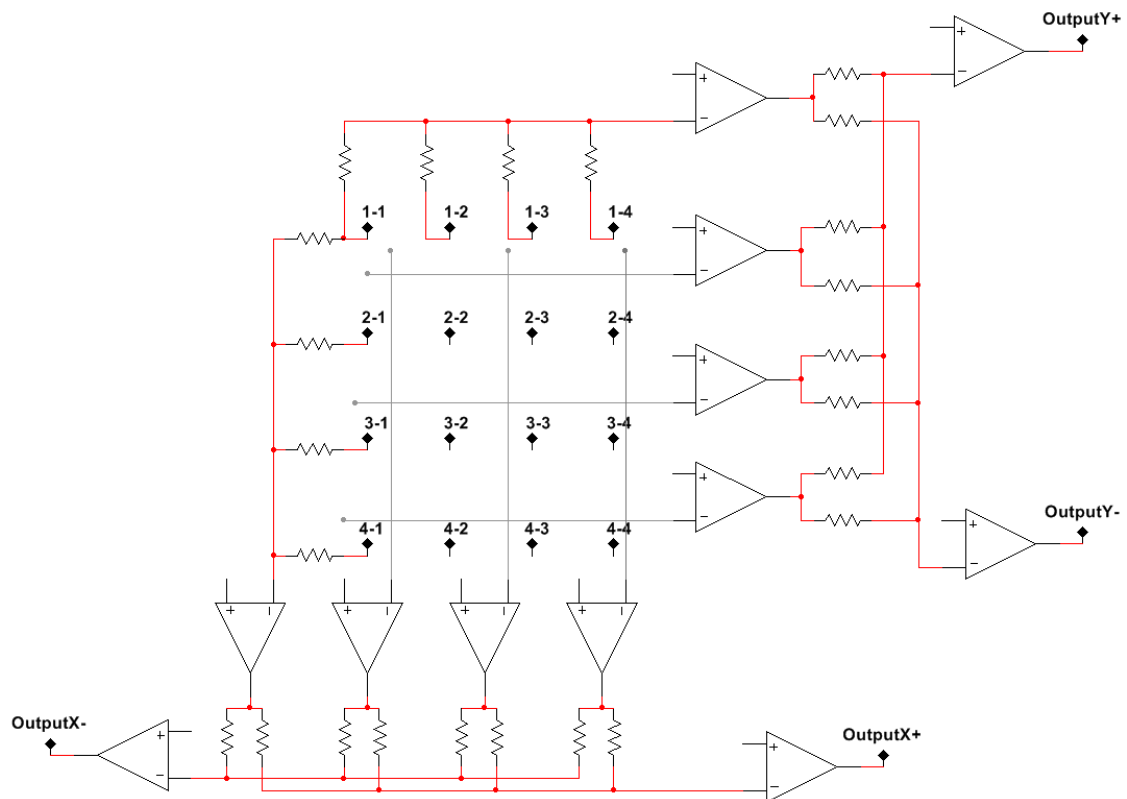
Figure 2-21 A circuit for multiplexing 16 SiPM signals (1-1, 1-2, 1-3, ..., 4-4) to four outputs X+, X-, Y+, Y-. The gray lines are abbreviations of the resistors for the rest of the rows/columns.

The calculation of the ratio and the sum of these two signals can be done easily in software. In total, there will be four analog outputs from a detector module with a two

29

dimensional SiPM array. If the original array had 16 SiPMs, this approach would reduce the output channels by a factor of 4 (16÷4=4). If more SiPMs are combined to form a bigger array, the channel reduction ratio will be even higher. This multiplexing method was originally designed for the multi-anode photomultiplier tubes [25], but Majewski et al. and Wang et al. have successfully used it to multiplex SiPM signals [26] [27].

The row/column summing involves an operational amplifier for each row and column. If space and power consumption is a concern, then the multiplexing method discussed in the following subsection will be more suitable than this row/column summing.

2.4.4   Charge division network

Another way to multiplex signals is to use the DPC (discretized proportional counter) circuit [28]. The circuit is made up of a network of resistors to divide the electrical charges from the SiPM into 4 outputs (Figure 2-22). Any current coming from the input nodes (1-1 to 4-4 in Figure 2-22) flows through a series of resistors. The resistor network acts as a charge divider, splitting the current into four unequal proportions. The relative signal amplitudes at these outputs indicate the location of SiPM while the sum of the 4 signals gives the amplitude of the original SiPM signal (Equations 2.4 to 2.6).

$$x = \frac{(C + D) - (A + B)}{A + B + C + D} \tag{2.4}$$

$$y = \frac{(A + C) - (B + D)}{A + B + C + D} \tag{2.5}$$

$$SiPM\ output = A + B + C + D \tag{2.6}$$

The A, B, C, and D are the signal levels at the four outputs of the charge division resistor network.
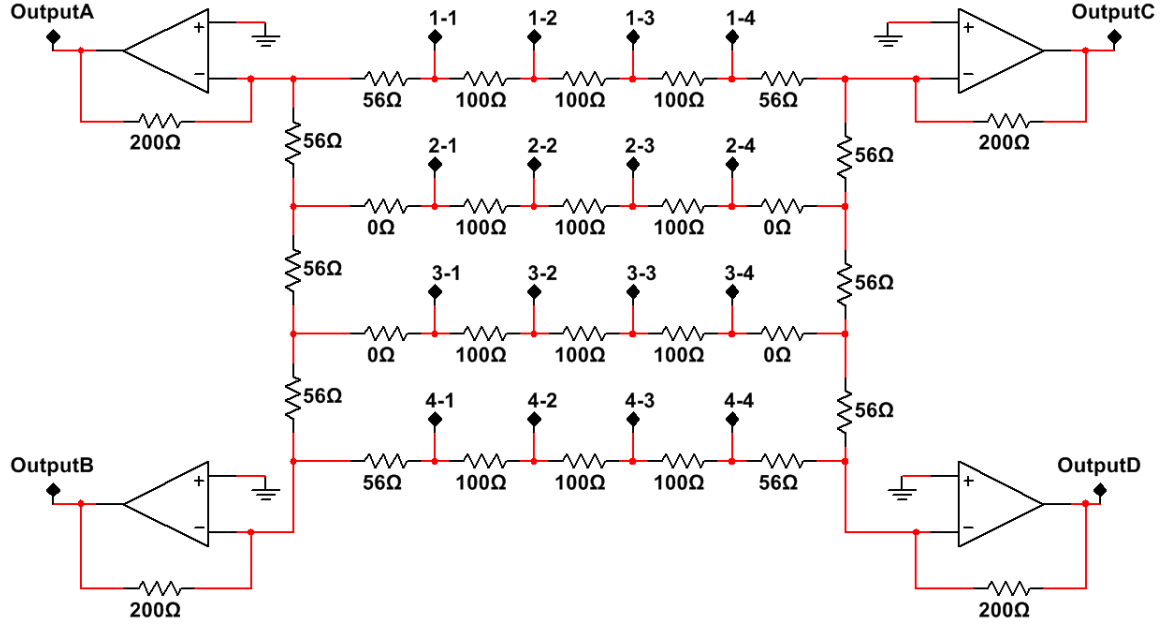
Figure 2-22 An example of a DPC circuit that can accommodate an array of 4 × 4 SiPMs.

This approach was initially developed for the multi-anode photomultiplier tubes as well, but Song et al. and Nakamori et al. have applied this technique to SiPMs [29] [30]. When applied to a 4×4 SiPM array, this technique also reduces the number of output channels by 4 times.

The downside of using a DPC circuit is that the resistance in the circuit will combine with the intrinsic capacitance in the SiPM to form an RC low pass filter, which lengthens the rise time of the signal pulse. The slower rising pulse will degrade the timing resolution. One way to circumvent this problem is to isolate the SiPM output from the DPC circuit with a current-current converter as described by Janecek et al. [31]. This way, the SiPM capacitance does not couple with the resistors in the DPC circuit, and the short signal rise time of SiPM is preserved.

31

2.4.5 Multiplexing beyond a 4 × 4 array

There have been reports on multiplexing SiPM arrays larger than the popular 4×4 format. Wang et al. have applied the row/column summing to an 8×8, and Majewski et al. to a 12×12 SiPM array [26] [27]. They reported that this multiplexing method gives good energy resolution and ability to resolve small crystals.

Others have reported that the charge division network also gives promising results. Yoon et al. and Xu et al. have used this approach to multiplex an 8×8 or a 12×12 array of SiPMs [21] [32].

In addition to these two methods, SensL has also developed a multiplexing scheme that is especially suited to multiplex a large number of SiPMs. The detail of their setup will be discussed in the next chapter.

A detector with a larger area is useful because it means that the entire PET system can be made up of fewer detector modules and fewer analog channels. However, every SiPM produces dark current noise. Combining SiPM signals will certainly combine their noise as well, leading to a poorer detector performance. The impact of dark current noise on detector performance will be examined in the next three chapters.

3 SensL SPMMatrix

3.1 Introduction

The first part of the project is to characterize the commercial device SPMMatrix, which was designed and manufactured by SensL. The SPMMatrix contains 256 SiPMs and employs a unique multiplexing scheme, which will be described in this chapter. The SPMMatrix system also has a complete set of readout electronics with a USB interface for control and data acquisition. A piece of software was written to communicate with the device and to process the acquired data. This chapter summarizes the system's energy resolution and ability to resolve crystals in a pixelated scintillator array.

3.2 Device description

The detector head consists of a 4×4 array of SensL SPMArray4 detectors, giving a total of 256 SiPM pixels arranged in a 16×16 array with a total active area of 61.3 mm $\times$ 61.3 mm (Figure 3-1).
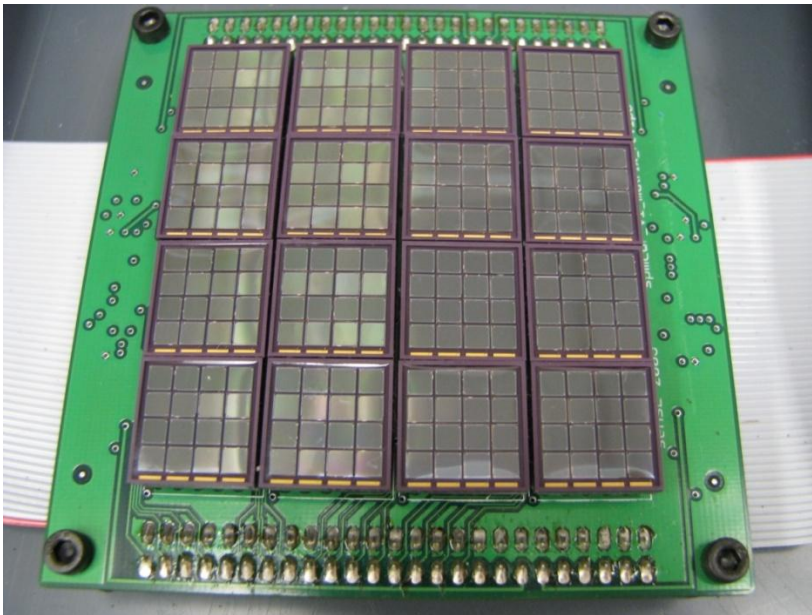
Figure 3-1 Close up photograph of the SiPMs in SensL SPMMatrix.

The SPMMatrix unit includes all the electronics required to read out the detectors, with 32 channels of shaping and analog to digital converter (ADC) along with a field-programmable gate array (FPGA) based data acquisition board (Figure 3-2). The ADC samples the signal pulse at its peak and then passes the digital value to the FPGA. The FPGA sends data to the host computer via a universal serial bus (USB) cable. The current version of the firmware on the FPGA does not allow timing measurement, so the timing resolution of this system is not tested.
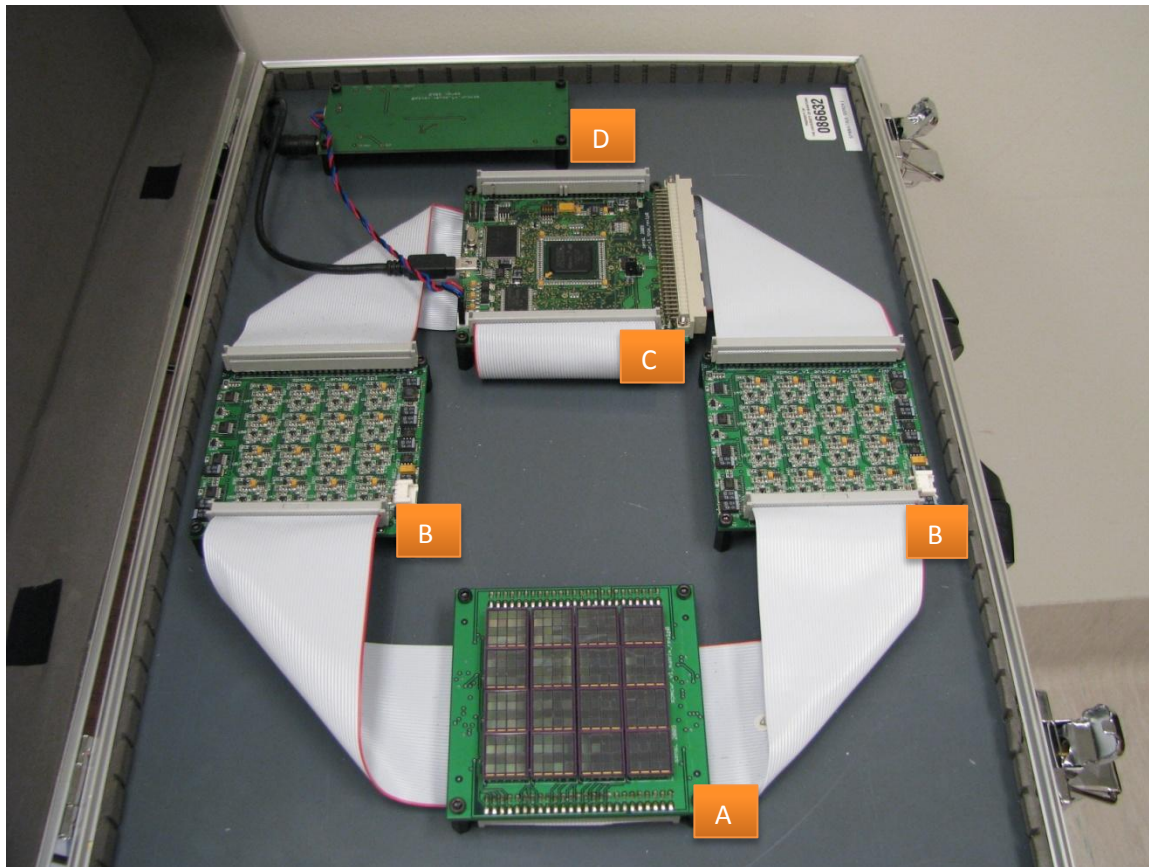
Figure 3-2 SensL SPMMatrix and the associated electronics. A) the detector head B) two boards housing the analog to digital converters C) The controller board with an FPGA in the middle. D) power supply.

SensL provides a device driver in the form of a dynamically linked library, MatrixAPI.dll. A C program was written in LabWindows/CVI (National Instruments, Austin, TX) to communicate with the SPMMatrix via this MatrixAPI.dll (Figure 3-3). The program provides a graphical user interface to control the SPMMatrix as well as to retrieve and process the incoming SiPM data.
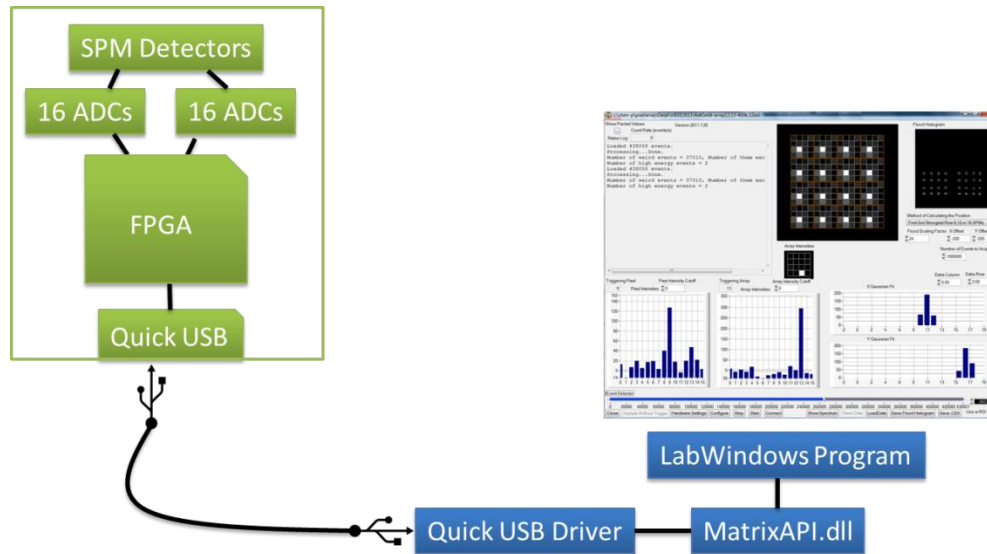
Figure 3-3 A block diagram of the data acquisition process, depicting how the various components are connected to each other. The green line encircles the components in the SPMMatrix, and the blue pieces are software on the host computer.

The signals from the 256 SiPM pixels are multiplexed to 32 analog channels according to an array/pixel summing strategy. Due to the way signals are multiplexed, the 32 channels are divided into two groups. Sixteen of the channels, A0…A15, are the array channels where each channel is the sum of the 16 pixels in an array (Figure 3-4). The other sixteen channels, P0…P15, are the pixel channels, where pixels of the same relative position in an array are summed (Figure 3-5). This multiplexing scheme requires a more complex position decoding software than the traditional row/column multiplexing designs described in section 2.4.
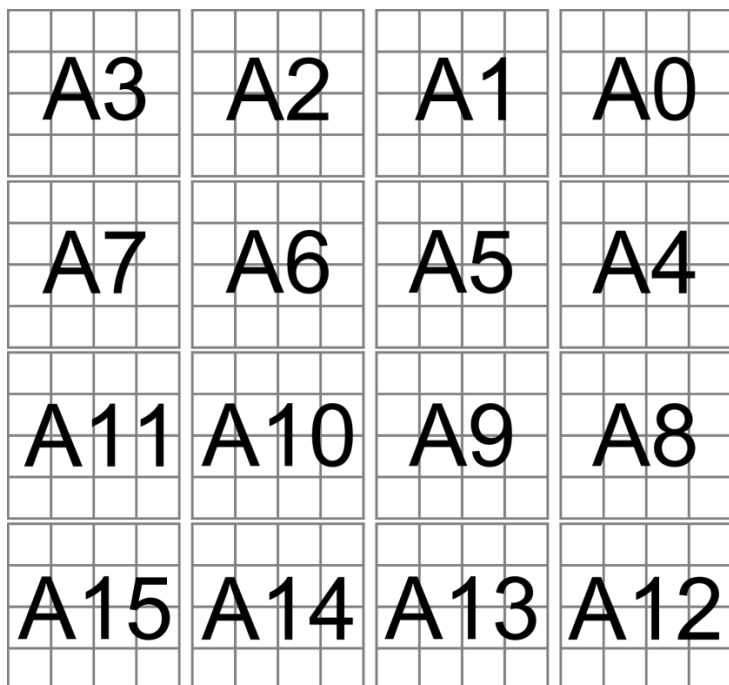
Figure 3-4 An array channel provides the signal sum of all pixels in that array. For example, channel A0 is the sum of all 16 SiPM pixels in the top right corner. Channels A0 to A15 represent signals from the sixteen arrays.
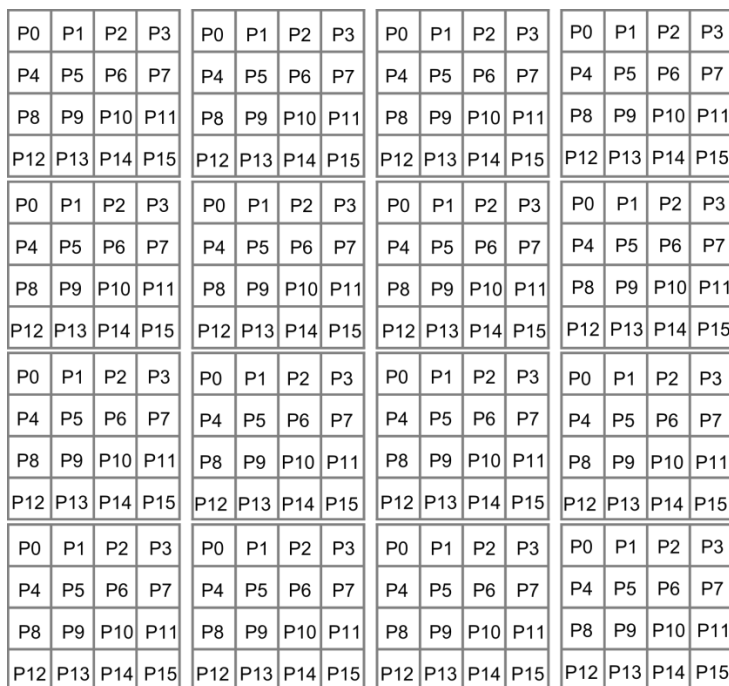
Figure 3-5 A pixel channel gives the sum of pixels that are at the same relative position in their respective arrays. For instance, all SiPM pixels labelled P0 in this diagram are summed into pixel channel P0.

3.3 Event positioning method

The position of a scintillation event can be estimated by the array channel ADC values. A large ADC value indicates that the light source is above that particular array. But to get a more precise position within the array, we will need to use the pixel channel data. The position within the array is calculated by putting the 16 pixel channel ADC values into a centre of mass formula, Equations (3.1) and (3.2).

$$x = \frac{\sum_{i=1}^{4} \sum_{j=1}^{4} P_{i,j} \times j}{\sum_{i=1}^{4} \sum_{j=1}^{4} P_{i,j}} \tag{3.1}$$

$$y = \frac{\sum_{i=1}^{4} \sum_{j=1}^{4} P_{i,j} \times i}{\sum_{i=1}^{4} \sum_{j=1}^{4} P_{i,j}} \tag{3.2}$$

In these equations, $P_{i,j}$ is the ADC value of the pixel in the ith row and the jth column.
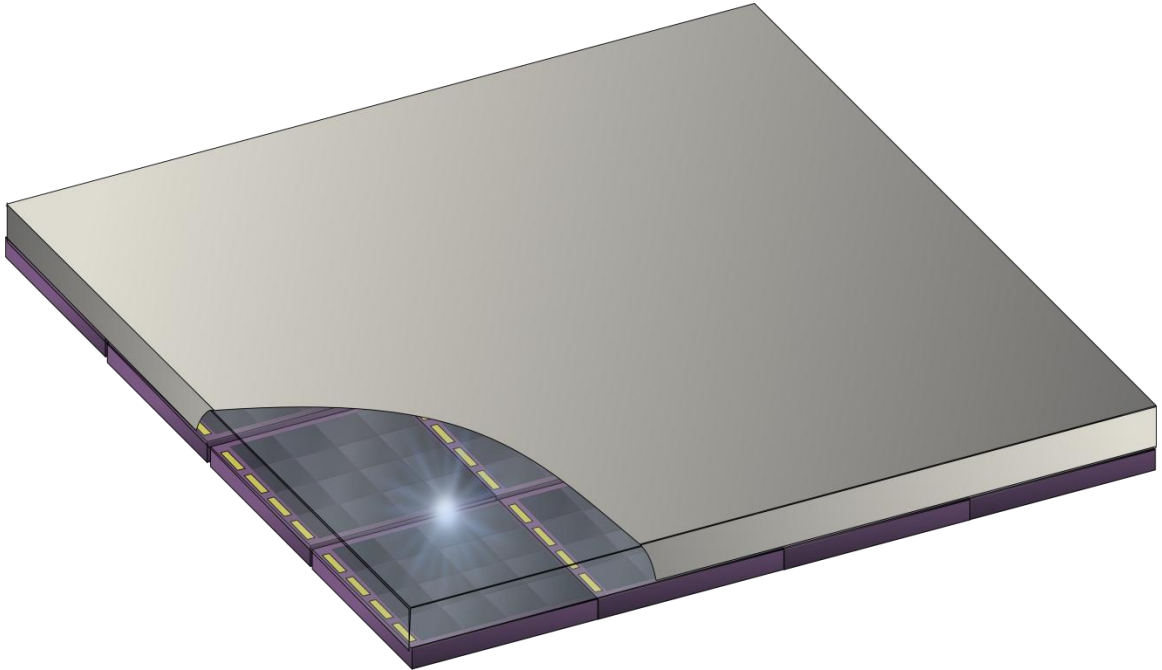
Figure 3-6 A large scintillator crystal slab sitting on top of the SPMMatrix. The crystal is covered with a reflective material and the material is torn at one corner to show the scintillation light shining on the SiPMs below.

This centre of mass formula will not work when the light spreads across many arrays, as will happen for the scintillator slab shown in Figure 3-6. The formula works well only if light falls on only one SiPM array at a time, like for the setup in Figure 3-7. However, there is still another problem that exists even in discrete crystal blocks. It is possible to have simultaneous scintillation events in different crystals, and this will pose a challenge in event positioning, sometimes making it an impossible task to do. This is because all arrays share the same 16 pixel channels, and hence critical information is lost in this mixing process. As long as the radiation source has a weak activity, the chance of this happening is small.

The testing of the SPMMatrix was done using only one scintillator array block at a time (Figure 3-8). A ^{68}Ge 511 keV source was used to flood irradiate the crystals. The scintillation events were sorted into a flood histogram based on their calculated position. Figure 3-9 is the flood histogram obtained with the setup shown in Figure 3-8.
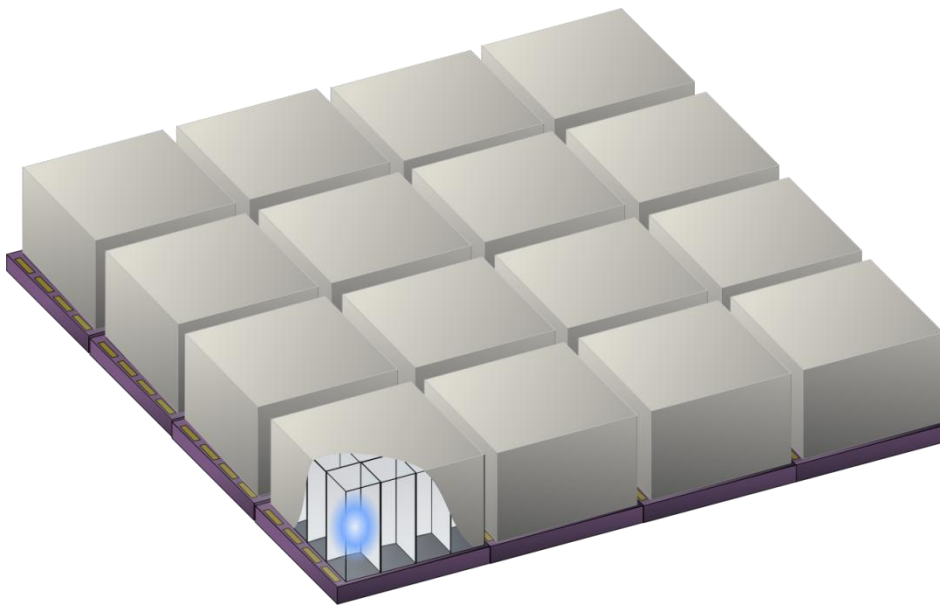
Figure 3-7 The SiPM arrays in the SPMMatrix are filled with discrete crystal array blocks. The scintillation light is confined within an array.
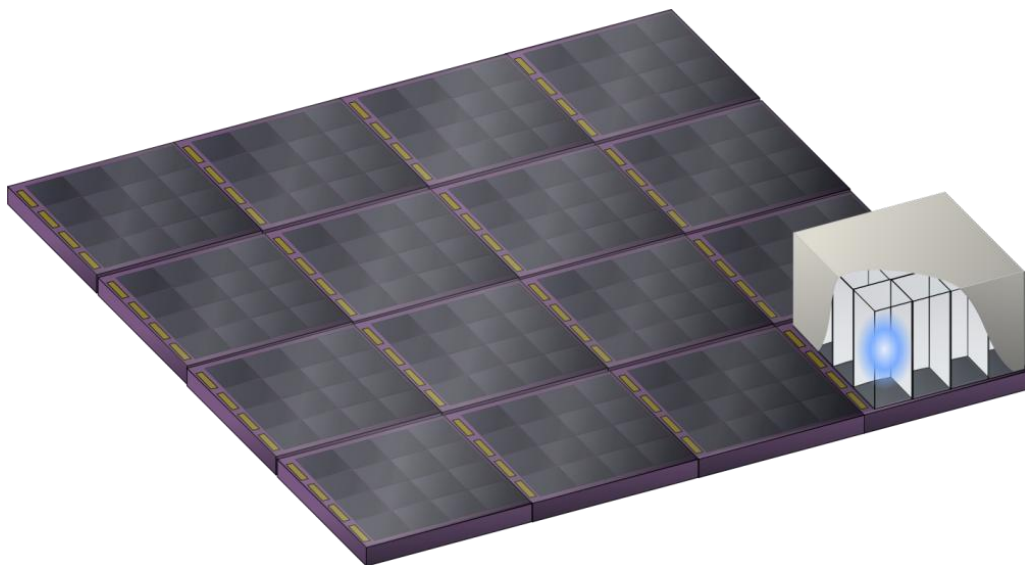
Figure 3-8 A 4 × 4 array of LYSO crystal sitting on top of a SiPM array. There is exactly one crystal per SiPM. The crystals are bonded together by a specular reflector, and the top and four sides of the block are covered with reflector as well. The blue scintillation light is collected by the SiPM under the crystal.
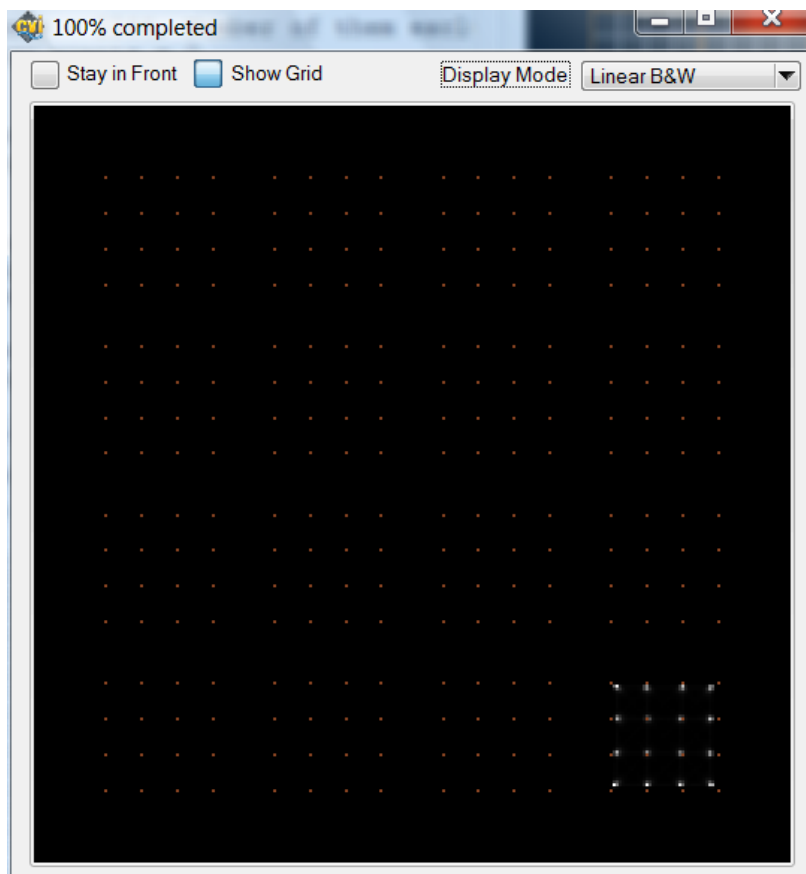
Figure 3-9 The flood histogram of a 4 × 4 crystal array. The white dots are where the events are located. The brightness of the dot is proportional to the number of events at that location. The brown dots are drawn on top of the flood image to show the centre location of each SiPM.

3.4 Improving the accuracy of the positioning algorithm

Even though reasonably good position accuracy can be achieved by entering the 16 pixel ADC values into the centre of mass formula, there are a couple of problems with this approach. In pixelated scintillator arrays, the scintillation light will only illuminate a small area. Most of the light falls on only a 2×2 or a 3×3 array of SiPMs. Therefore, to calculate position, using 4 or 9 pixel ADC values may be sufficient; there is no need to use all 16. The dark firing current from other arrays contribute a significant amount of noise to the pixel channels. SiPM pixels far away from the light source will contain mostly just noise. Therefore, incorporating those pixels that receive very little light will introduce extra noise but little useful information.

A better approach is to weight the pixel ADC values before entering them in the centre of mass formula. SiPM pixels that are close to the light source should receive more weight than those that are far away. This gives preference to pixel values that have higher signal to noise ratios. The result of switching to this approach is a significant improvement in positioning accuracy and better crystal identification in the flood histogram.

The weight applied to the pixels follows a 2D symmetric Gaussian distribution. The centre of the Gaussian curve is at the current estimate of the location of the light source. The optimal standard deviation is found to depend on the amount of light spread, and the centre-to-centre distance between adjacent SiPM pixels seems to be a suitable value for this detector setup. Although not examined, many other apodization functions can also be used in place of the Gaussian function as the weight function.

The revised centre of mass formula with weight factors is shown below.

$$w(i,j) = e^{-\frac{(j-x_{old})^2+(i-y_{old})^2}{2\sigma^2}} \tag{3.3}$$

$$x_{new} = \frac{\sum_{i=1}^{4}\sum_{j=1}^{4} w(i,j) \times P_{i,j} \times j}{\sum_{i=1}^{4}\sum_{j=1}^{4} w(i,j) \times P_{i,j}} \tag{3.4}$$

$$y_{new} = \frac{\sum_{i=1}^{4}\sum_{j=1}^{4} w(i,j) \times P_{i,j} \times i}{\sum_{i=1}^{4}\sum_{j=1}^{4} w(i,j) \times P_{i,j}} \tag{3.5}$$

In these equations, $w(i,j)$ is the weight factor, σ is the standard deviation of the Gaussian curve centered at (x_{old}, y_{old}), and $P_{i,j}$ is the ADC value of the pixel in the ith row and jth column.

The position calculation procedure is as follows:

1. Identify, by looking at the array ADC channels, the array in which the event occurred.

2. Estimate the position of the light source using the original centre of mass formula.

3. Apply weight factors to all 16 pixels using Equation (3.3). The Gaussian curve is centered at (x_{old}, y_{old}). Pixels closer to the scintillation event receive more weight than those far away from the event.

4. Calculate a new position, (x_{new}, y_{new}), with the new weighted values using Equations (3.4) and (3.5).

5. Check if the position meets the convergence criterion in Equation (3.6). If it does, terminate the iteration. If the criterion is not met, let (x_{old}, y_{old})=(x_{new}, y_{new}), and repeat steps 3 to 5.

$$((x_{new} - x_{old})^2 + (y_{new} - y_{old})^2) \leq 0.0001 \tag{3.6}$$

For 97.8% of the events, the position coordinates converge within 10 iterations. Very few events, 0.2%, required more than 20 iterations.

The following figures, Figure 3-11 – Figure 3-16, show the flood histograms of various crystal array types. These include:

1. 4×4 array with crystal size 3.17 mm × 3.17 mm × 10 mm.

2. 10×10 array with crystal size 1.5 mm × 1.5 mm × 10 mm.

3. 7×7/8×8 dual layer array with crystal size 1.67 mm × 1.67 mm × 4 mm for the top 7 × 7 array and 1.67 mm × 1.67 mm × 6 mm for the bottom 8 × 8 array (Figure 3-10). This double layer construction provides depth of interaction information, which can be used by the PET system to improve image spatial resolution.
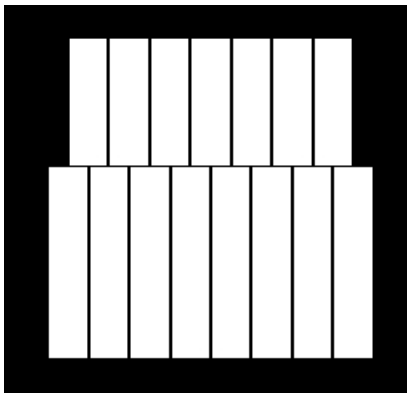
Figure 3-10 The 7×7/8×8 dual layer array. (Drawing provided by Dr. Xuezhu Zhang)

Each array is shown twice, once using the iterative weighted centre of mass formula, and once using the conventional centre of mass formula. For every type of scintillator array, the weighted centre of mass version always gives a much better flood histogram, with all the clusters clearly visible.

42
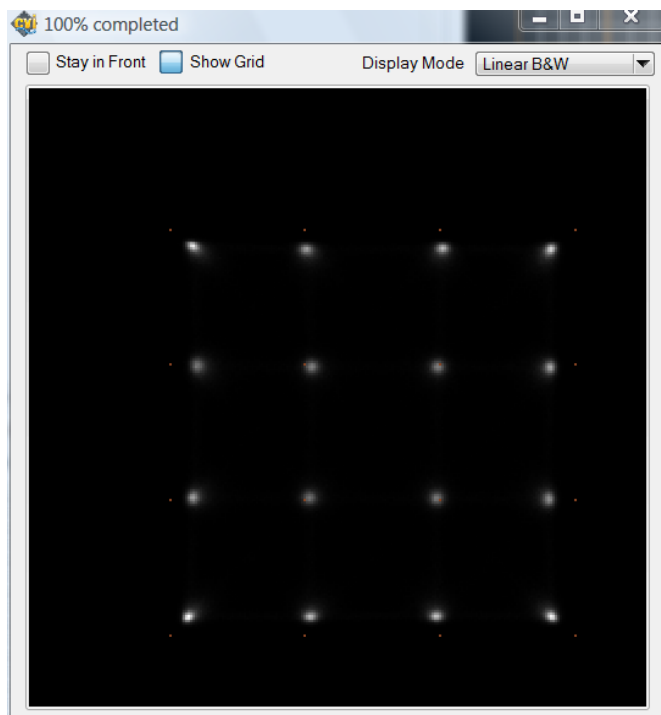
Figure 3-11 A zoomed in version of the flood histogram in Figure 3-9. The position is calculated using the weighted centre of mass formula.
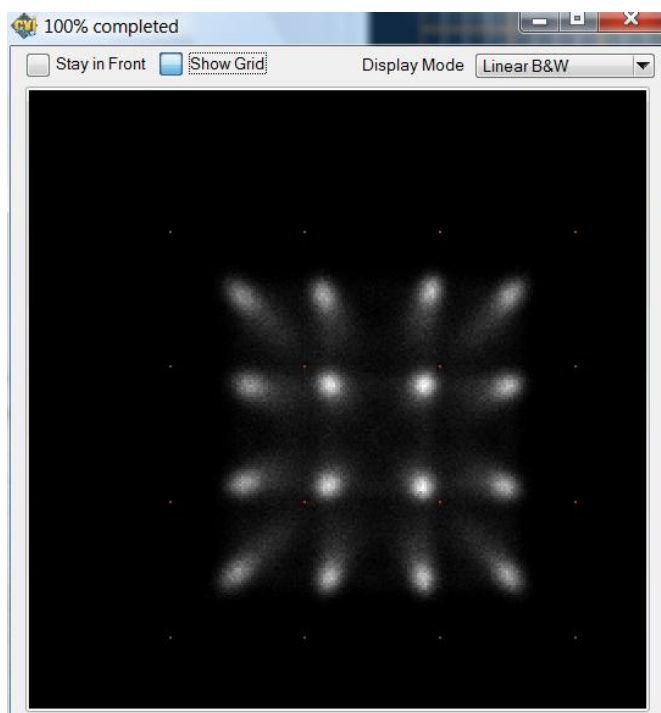
Figure 3-12 This is the same data set as the one in Figure 3-11, but the position is calculated using the conventional centre of mass formula. Without applying the Gaussian mask, the calculated position is heavily influenced by the SiPMs that do not receive a lot of light, hence the smearing of the dots towards the centre of the array.
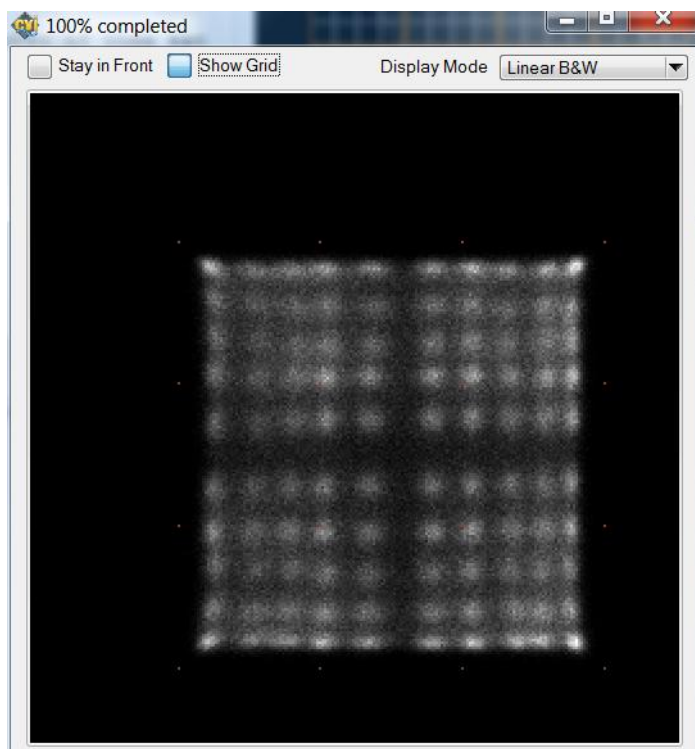
Figure 3-13 The flood histogram recorded by placing a 10 × 10 array of LYSO scintillator crystals on one SiPM array.
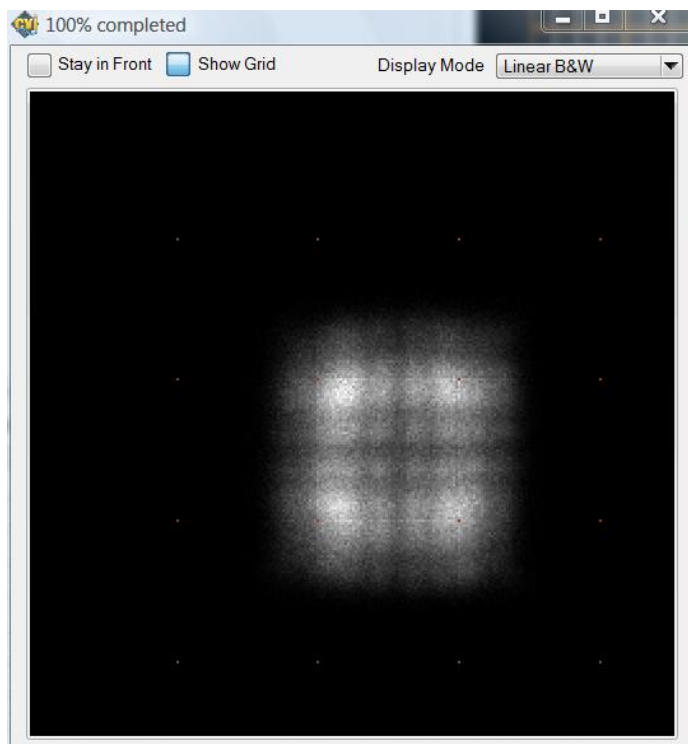
Figure 3-14 The same data set from Figure 3-13 calculated using the conventional centre of mass formula. The individual crystals are indistinguishable.
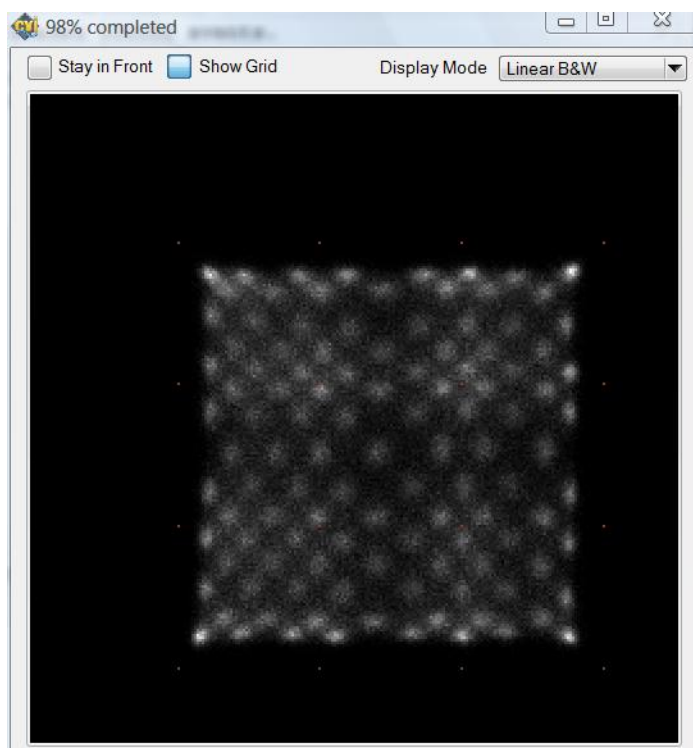
Figure 3-15 The flood image of a 7 × 7/8 × 8 dual layer crystal array. The position calculation was done using the weighted centre of mass method.
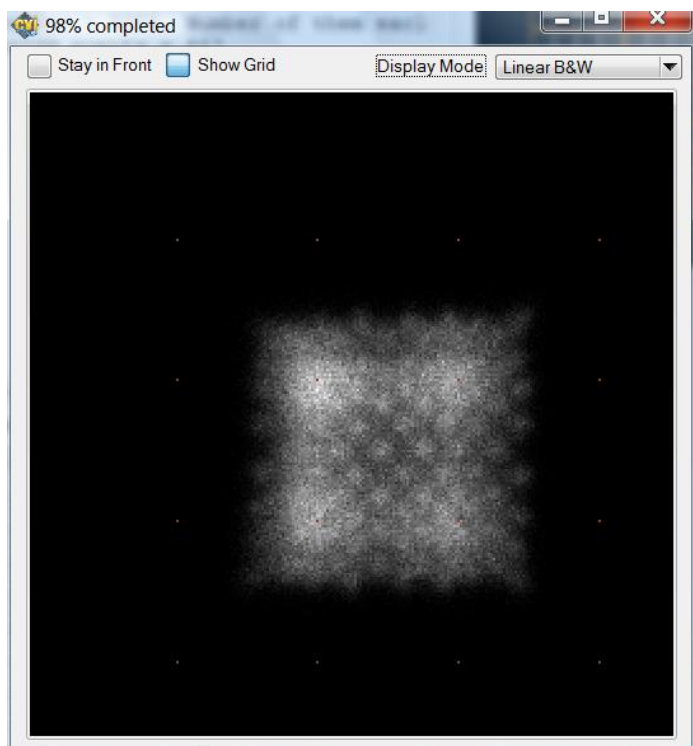
Figure 3-16 The same dual layer crystal array data set calculated using the conventional centre of mass formula.

3.5 Crystal between arrays

So far all data shown are for crystals that are situated above a single SPMArray4 chip. Even if all the SiPM arrays are occupied with crystals, this will still leave large gaps between arrays, as shown in Figure 3-7. To obtain better gamma-ray detection efficiency, it is beneficial to fill the space above the inter-chip area with scintillator crystals to capture gamma photons that just happen to pass through those areas. Populating the gaps with crystals will require the ability to measure light coming from those areas. Because the edges of the SPMArray4 chip are insensitive to light, it is necessary to elevate the crystal with a transparent material of about $1 - 2$ mm thick (see Figure 3-17 for example). This transparent material will act as a light diffuser or a light guide to spread light to the sensitive area of the chip.

Identifying which SiPM arrays the light went to is relatively easy. This can be done by identifying which 2 or 4 arrays that have the largest signal amplitude. If only 2 arrays have significant signal, then the crystal is most likely sitting above the gap between those 2 arrays, and if 4 arrays have significant signal, then the crystal is probably sitting at the corner between those 4 arrays. The difficult part, however, is locating the exact position of the scintillation within the gap.

The amount of light that finally reaches the sensor is small, so the signal is weak and noisy. In this case, using the pixel channels like before to position the event will not give an accurate result. It was found that it is better to use instead the values of the array channels to calculate the position. The centre of mass formula can also be applied to the array channel values to get the event's position. The advantage of using the array channels is that, at most, only 4 ADC values are needed. Using the pixel channel data

46

would require more. As discussed previously, the fewer values included in the calculation, the less influence there will be from the dark firing noise from the other arrays.

The following is the result of decoding a 4×4 array of scintillator crystals above the corner of four SiPM arrays. In these tests, a glass microscope slide of 1 mm thickness was inserted between the scintillator and the light sensor (Figure 3-17). The small space between the scintillator and the glass, as well as the space between the glass and the sensor, are filled with optical grease (Dow Corning Q2-3067 optical couplant). This prevents the extreme change in refractive index at the boundaries if the air gap were to be left unfilled. Filling the air gap with optical grease facilitates the movement of optical photons from the scintillator to the sensor. Figure 3-18 to Figure 3-20 show the results of reading scintillator crystals above the non-sensitive gap between arrays.
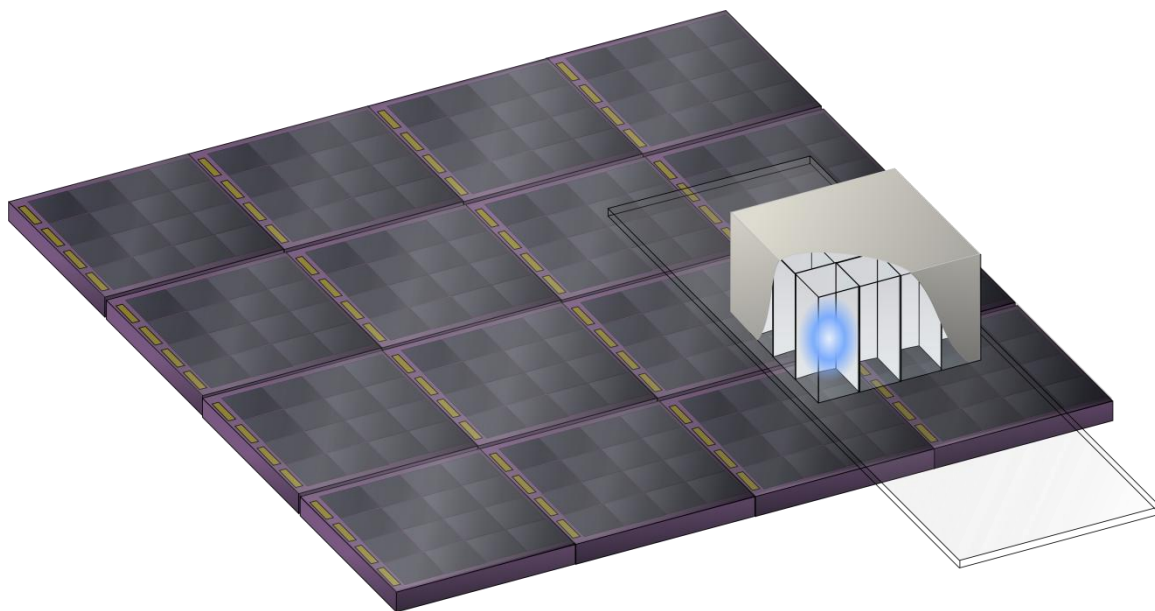
Figure 3-17 A 4 × 4 crystal array sitting between four SiPM arrays. The crystal block is positioned so that the second column and the third row of crystals are directly above the dead space between sensors. A glass microscope slide helps spread out light from these crystals.
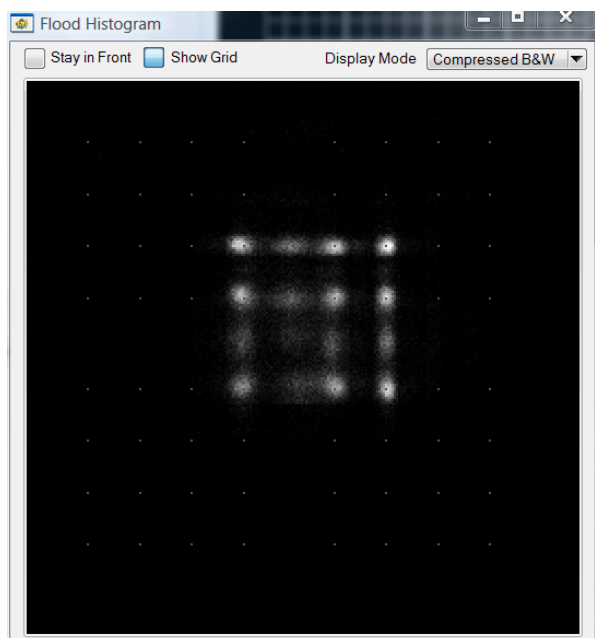
Figure 3-18 A 4 × 4 crystal array sitting between four SiPM arrays. The second column and the third row of crystals are directly above the dead space between sensors. Because a lot of light is lost, the SiPM signal is relatively noisy. Therefore, the calculated position is not very accurate for events in those crystals. This leads to a larger spread in those event clusters.

48
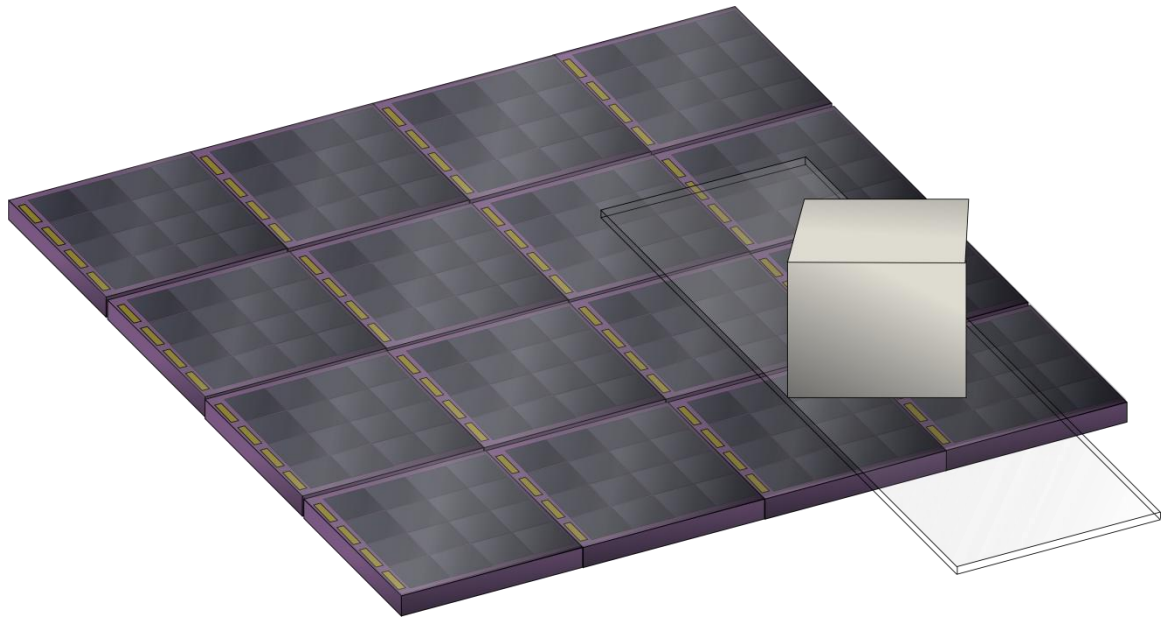
Figure 3-19 The same 4 × 4 scintillator array rotated by 45°.
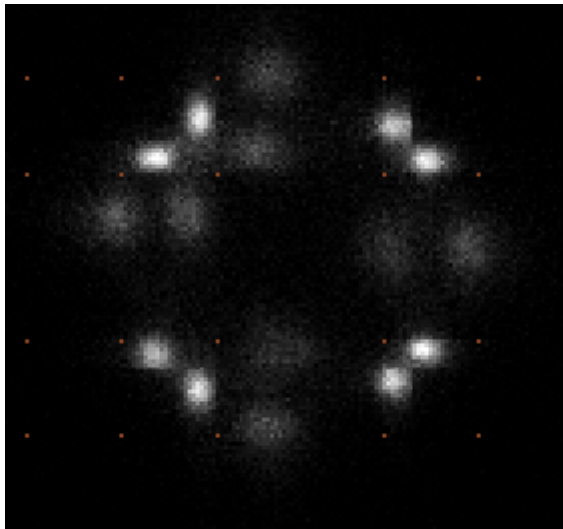
Figure 3-20 The same 4 × 4 array rotated by 45°. There is a distortion in the flood image, likely caused by an uneven spread of light. In spite of the distortion, all sixteen crystals are distinct.

3.6 Energy resolution of the system

To measure the energy resolution, one 4×4 array of LYSO crystals was coupled with optical grease to one of the SPMArray4 detectors in the device. The crystals were flood irradiated with a ^{68}Ge radioactive source. The events were sorted into a flood histogram. The flood histogram was segmented using a custom Matlab script (Mathworks Inc., Natick, MA) developed in the lab to separate events from different crystals. Figure 3-21 shows the flood histogram after segmentation. The segmentation mechanism first identifies all the bright spots in the flood histogram. Then it draws the crystal boundaries along the midway points between bright spots.
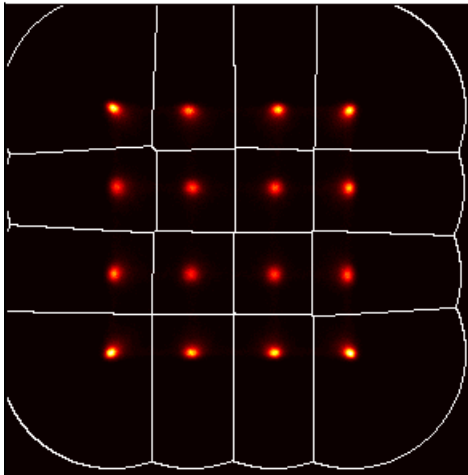
Figure 3-21 A segmented flood histogram. The white lines delineate the boundaries between events from different crystals. All events within any section are assumed to originate from the same crystal.

For every crystal, the Matlab script creates an energy spectrum of the 511 keV photons from the ^{68}Ge source and then calculates the photopeak position and energy resolution.

We investigated two methods of obtaining the energy information from the 32 channels of data [33]. The first method uses the maximum ADC value of the array

50

channels, A0…A15, as the value for energy. The second method uses the pixel channel data and sums the ADC value of the strongest pixel together with its 8 neighbouring pixels. For the second method, the addition of neighboring pixels is necessary because even though there is a one to one coupling between the crystal and the SiPM, the epoxy layer on the detector surface allows some light to spread across multiple pixels. The true energy will only be recovered if the ADC values of the neighbouring pixels are added to the strongest pixel.
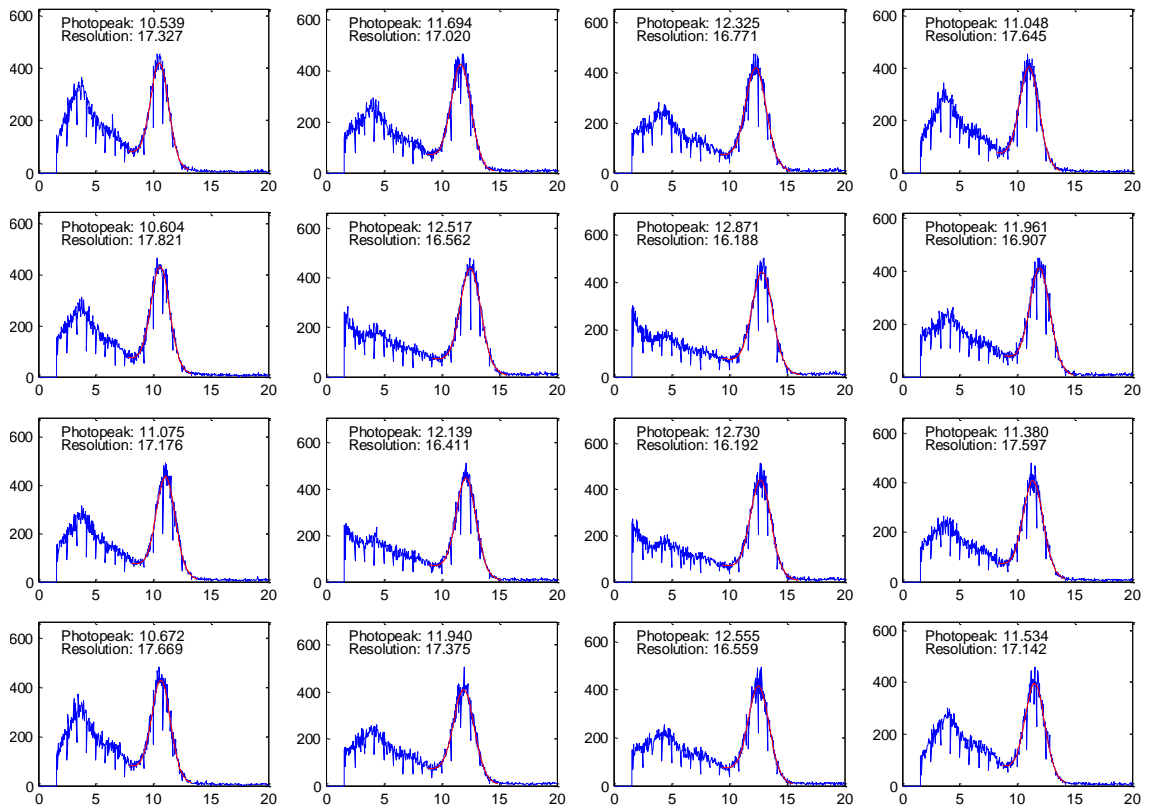
Figure 3-22 The energy spectra of the 511 keV photon measured by each of the 16 crystals. The energy values are calculated using the array channel ADC data. The blue curve is the measured energy spectrum, and the red curve is a Gaussian fit to the 511 keV photopeak. The x-axis represents energy, but the numbers here are not calibrated. The y-axis represents the number of events. The energy resolution reported here is the full-width-at-half-maximum of the fitted curve divided by the peak centroid. Energy resolution is in percentage.
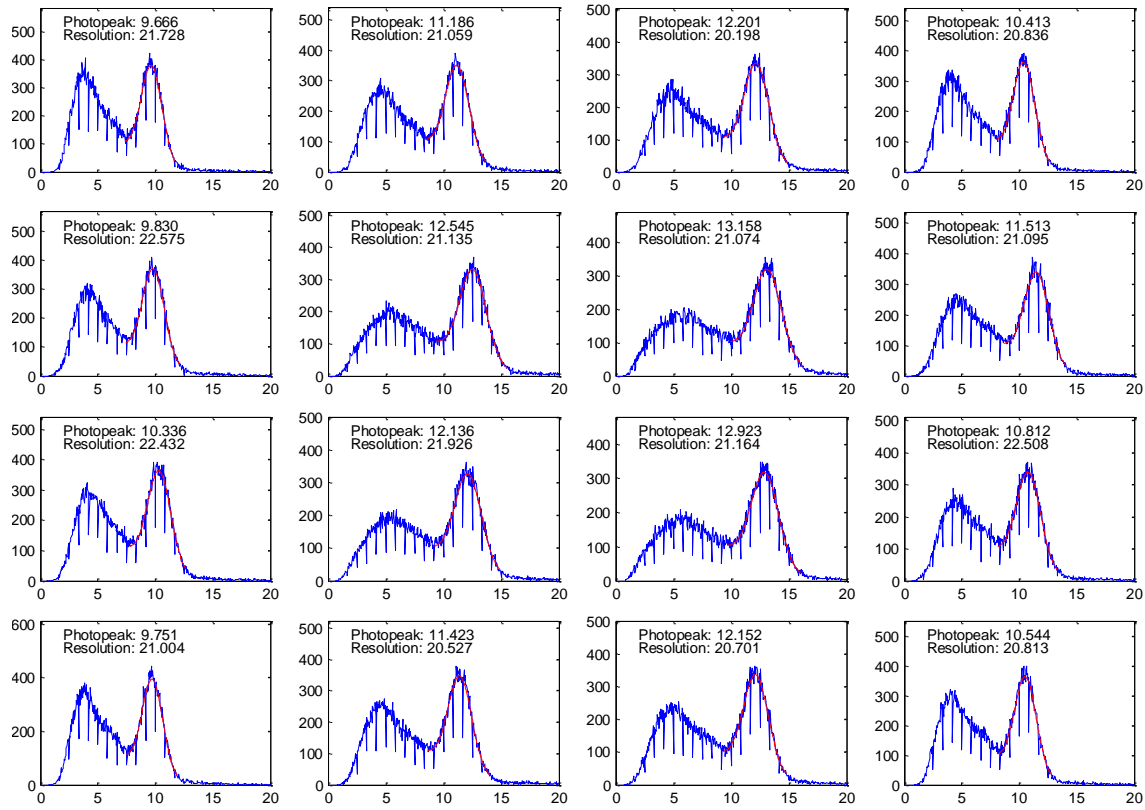
Figure 3-23 The same data set as in Figure 3-22, but the energy is calculated using the pixel ADC values.

Figure 3-22 shows the energy spectra calculated using the array channel data. The average energy resolution is 17.1±0.6%. In comparison, Figure 3-23 shows the energy spectra for the same data set but calculated using the pixel channel data. The average energy resolution is 21.5±0.7%. It is clear from these two figures that the energy resolution is better if the energy values were obtained from the array channel. It appears that the dark current noise from the other arrays is the cause of the worse energy resolution when using the pixel channel data. Since a pixel channel ADC value represents a sum of 16 pixels, one from each of the 16 arrays. This approach of calculating energy incorporates the dark noise of 144 SiPM pixels, where as one array ADC value contains noise from only 16 pixels.

52

3.7   Interference between signals

The SPMMatrix allows individual adjustment of each SPMArray4 detector's bias voltage. Since the dark current increases with the bias voltage, we can change the amount of dark current noise and look at its effect. Again, a 4×4 LYSO crystal array was placed on top of one SPMArray4, while leaving all the other SiPMs without crystals (Figure 3-8). Then the bias voltage of the array with crystals was turned to maximum (36.3 V), while leaving the other arrays at the minimum permitted by the device driver (33.0 V). After one data collection, the bias voltage on the idle arrays was turned up to the same maximum value 36.3 V to collect another set of data. It is important to note that the bias voltage setting quoted here is a nominal value provide by the driver and is not the same as the actual bias voltage applied to the detector. To get the actual voltage on the detector, one needs to measure the current consumed by the bias power line, a measurement not performed in this test.

The histograms of these two setups show a difference in quality (Figure 3-24 and Figure 3-25). When the amount of dark current noise from the idle arrays increased as their bias voltage was increased, the crystal blobs in the flood histogram grew bigger.
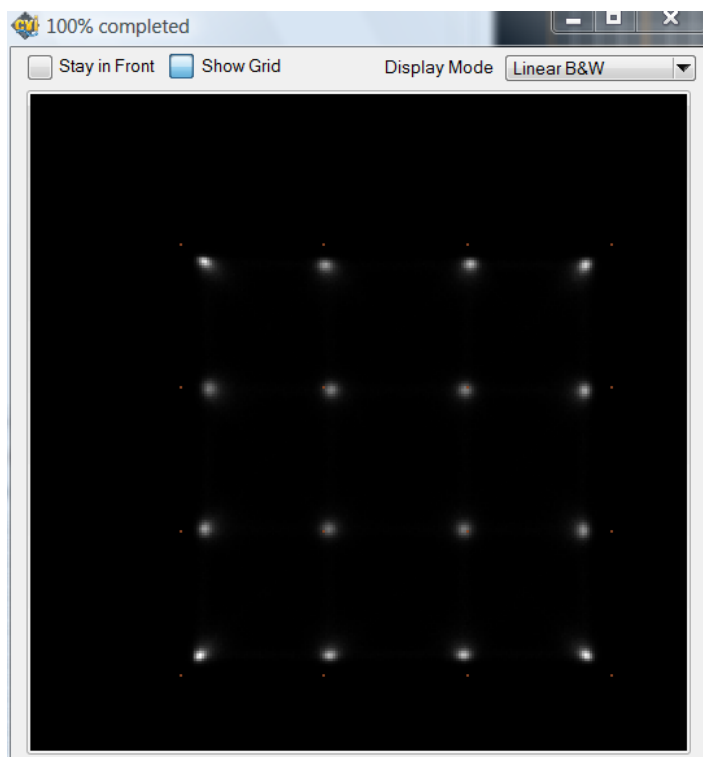
Figure 3-24 Only the array under the crystal is set at 36.3 V. All the others are set to the minimum 33 V.
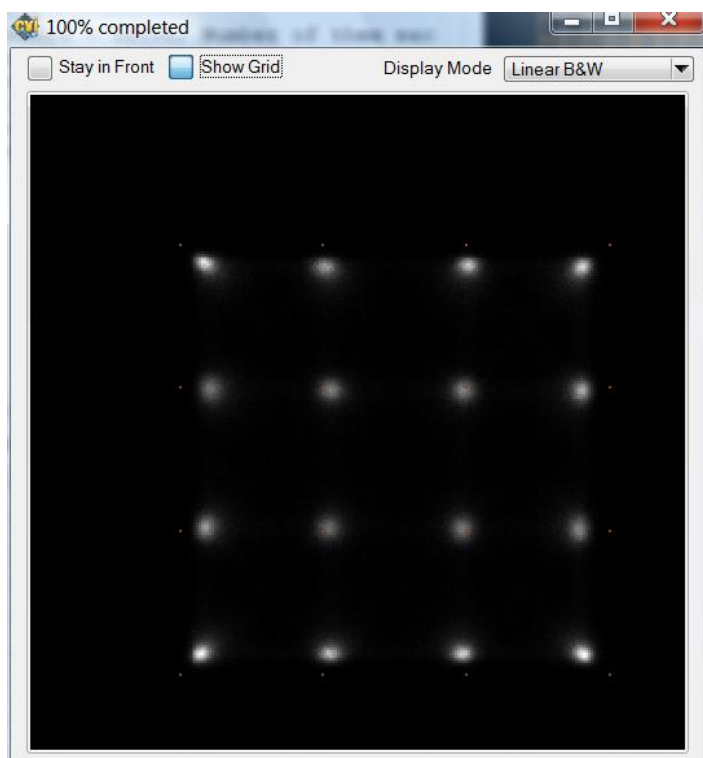
Figure 3-25 All the SiPM arrays are on maximum bias voltage 36.3 V. The increased dark noise from the other SiPM arrays reduced the accuracy of the calculated position, but the separation between crystal elements is large enough to make every element distinct.

54

A similar experiment was done using the 7×7/8×8 scintillator array. In this case, the crystals became indistinguishable as dark noise from the other arrays increased (Figure 3-26 and Figure 3-27). This poses a challenge in turning the SPMMatrix into a high spatial resolution detector. In normal operating condition, all the SiPM arrays should have the same bias voltage to give each sensor the same response characteristics. This means if we were to use the SPMMatrix as a PET detector, we would need to use crystal arrays with fewer crystal elements, and the detector will have a poor spatial resolution. The interference of dark current noise is a disadvantage of multiplexing.
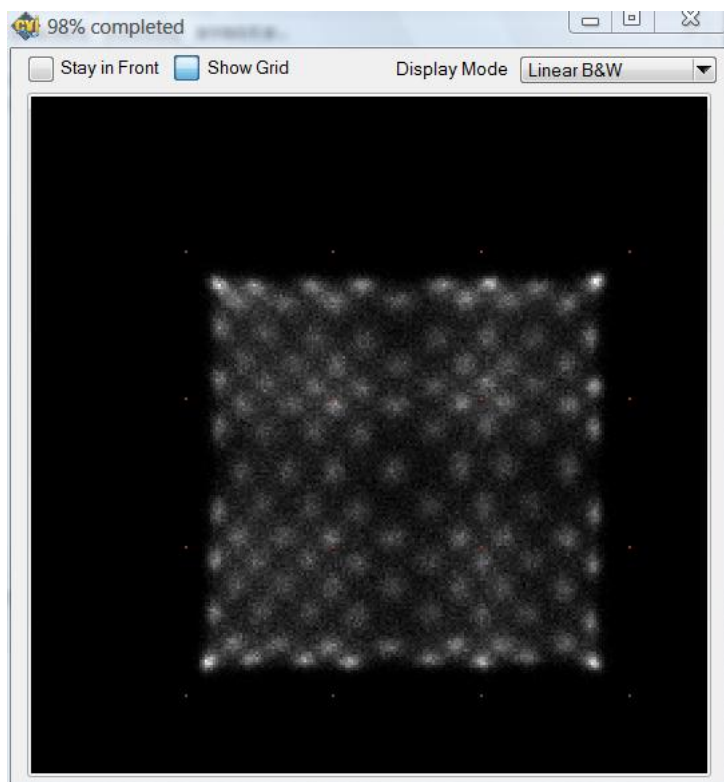
Figure 3-26 7 × 7/ 8 × 8 dual layer array. The idling SiPM arrays are on the low bias voltage setting, 33 V.
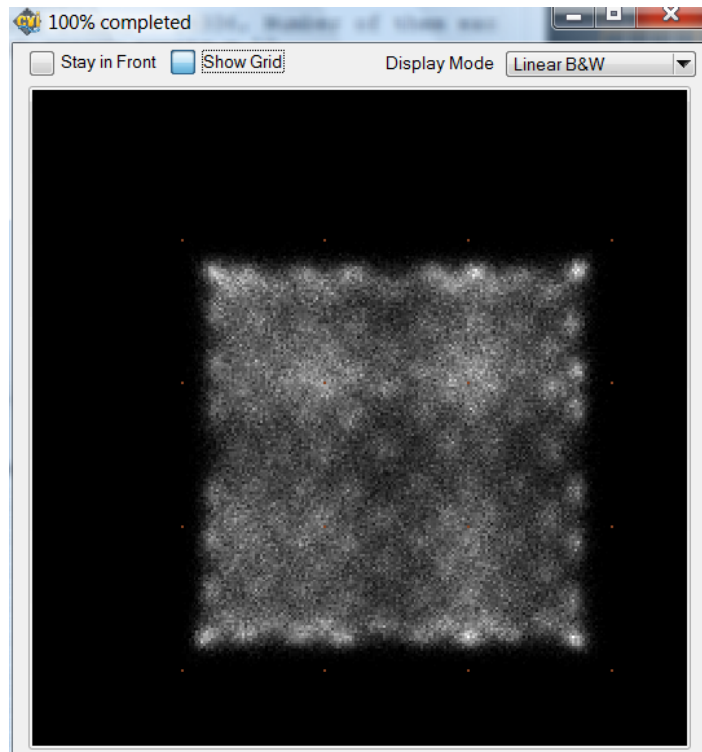
Figure 3-27 When the bias voltage of the idling arrays are turned up to the same level as the test array, the noise from them reduces the clarity of the flood histogram.

3.8 Summary

A computer program was written to control the SPMMatrix system and to retrieve and process the SiPM data. An algorithm was developed to calculate the location of scintillation. The system achieved a 17.1±0.6% energy resolution when reading LYSO scintillator crystals.

The SPMMatrix is suitable for a pixellated scintillator array and not a monolithic scintillator slab. Due to the multiplexing method, it is better to confine the scintillation light to one SiPM array only. If one needs to boost gamma ray detection efficiency by filling the inter-array gaps with crystals, it is better to have a light guide that channels light to one SiPM array on either side of the gap but not both.

The crystal elements in the scintillator array also needs to be sufficiently large, otherwise the crystals will not be resolved due to the excessive noise from multiplexing. Using large crystals implies a poorer spatial resolution for the system.

4 Multiplexing a 12 × 4 SiPM Array with a Charge Division Network

4.1 Introduction

The SensL SPMMatrix is suitable for reading scintillator crystals within the active area of each sensor. However, as was discussed in the previous chapter, it is difficult to use the SPMMatrix to read crystals in the dead space between two sensors. This led us to investigate another signal multiplexing approach that is easier to use to decode crystals between sensors.

The charge division resistor network was chosen as the multiplexing method for the new gamma ray detector. The detector has a 12×4 array of SiPMs made from tiling 3 SensL SPMArray4 detectors. The energy and timing resolution of this detector will be discussed in this chapter along with how these measurements were done. The last part of this chapter looks at the effect of dark current noise in this multiplexing method.

4.2 Design of the multiplexing circuit

The new gamma ray detector is based on the DPC multiplexing circuit, which is essentially a charge division resistor network [28]. The circuit board was designed to hold 3 of the SPMArray4 detectors side by side. The resistor chain of the DPC circuit reduces the number of output channels from 48 (3 arrays $\times$ 16 outputs/array = 48) to only 4 (Figure 4-1).
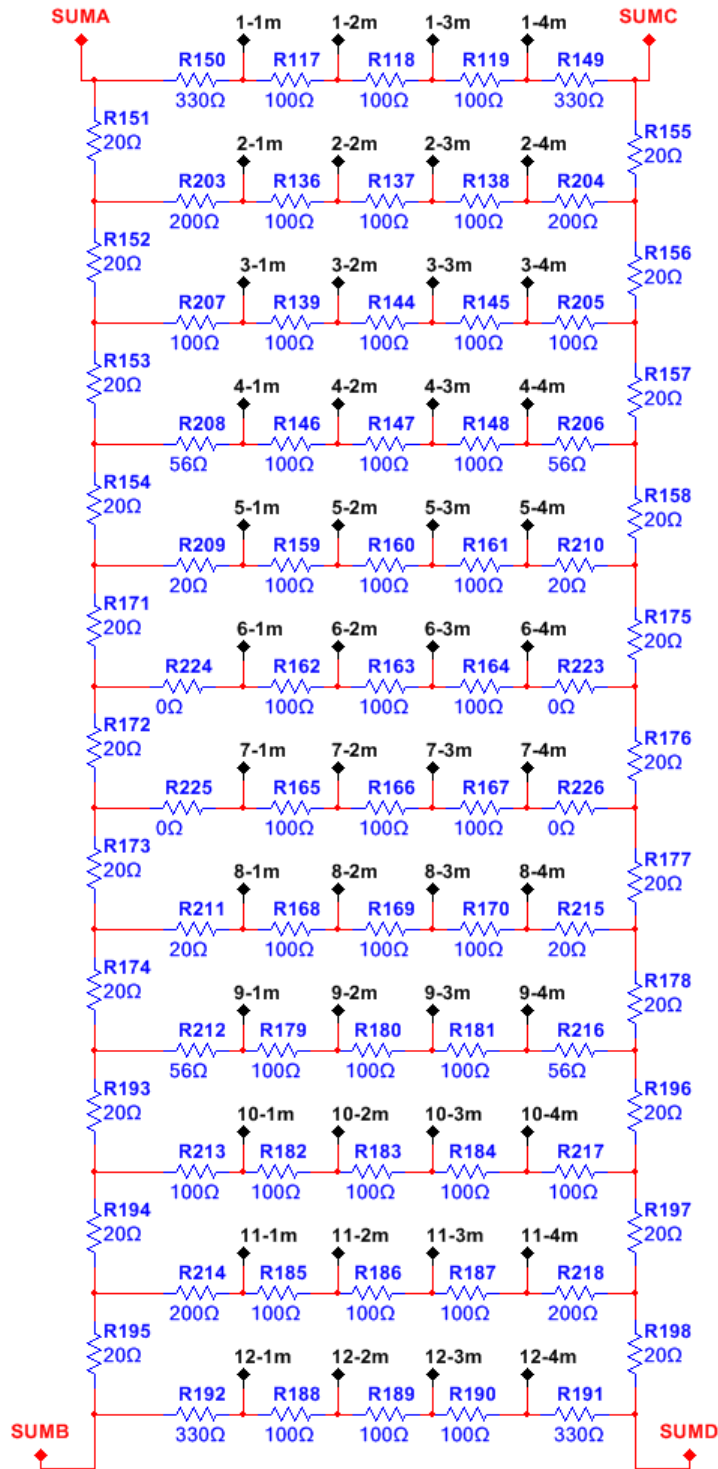
Figure 4-1 The charge division resistor network, a.k.a. DPC circuit, multiplexes the 12 × 4 SiPM signals to 4 channels. The # - # m connectors are the input points for the SiPM output. The SUM A/B/C/D points contain the multiplexed signals.

The resistor values in the resistor network are based on previous work done for a single 4×4 SiPM array (Figure 4-2) [34]. Expanding the network to accommodate three SiPM arrays required some adjustment to the resistor values. The appropriate resistor values were found by performing SPICE (simulation program with integrated circuit emphasis) simulations in the software Multisim (National Instruments, Austin, TX). The goal of the SPICE simulation is to find out the resister values that will make the multiplexed signals occupy the full dynamic range of the electronics while giving a rectangular flood histogram with large spacing between crystals. After the circuit schematic was determined, the layout for a double sided printed circuit board was drawn with the software Ultiboard (National Instruments, Austin, TX) (Figure 4-3). Figure 4-4 and Figure 4-5 are photographs of the completed gamma ray detector.
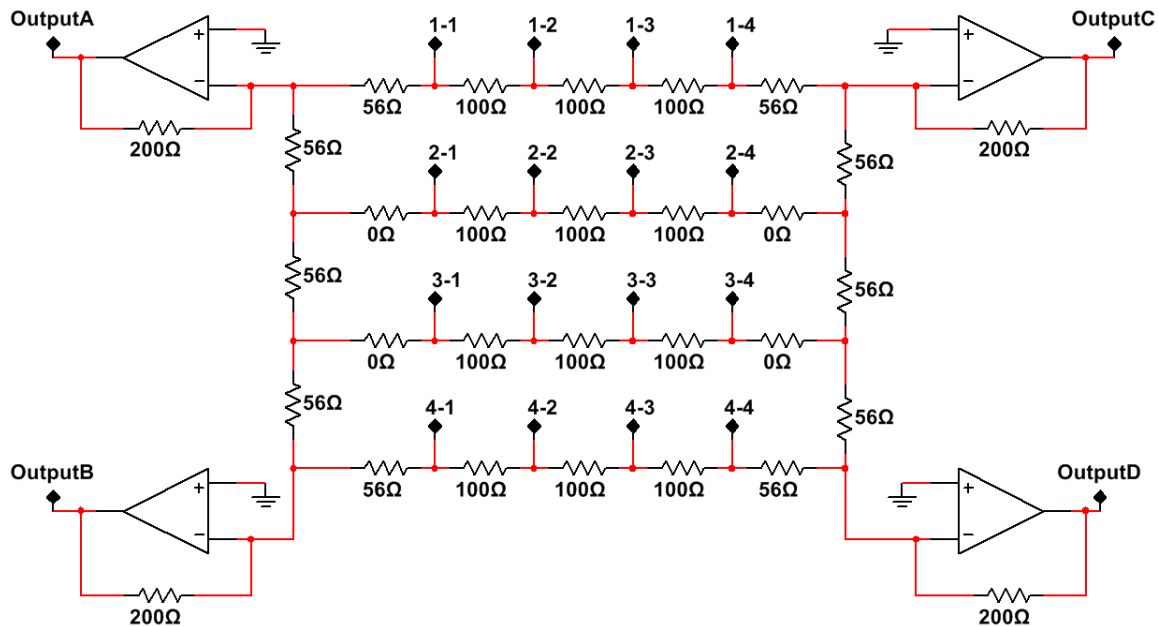
Figure 4-2 The charge division resistor network previously developed for a 4×4 array of SiPMs.
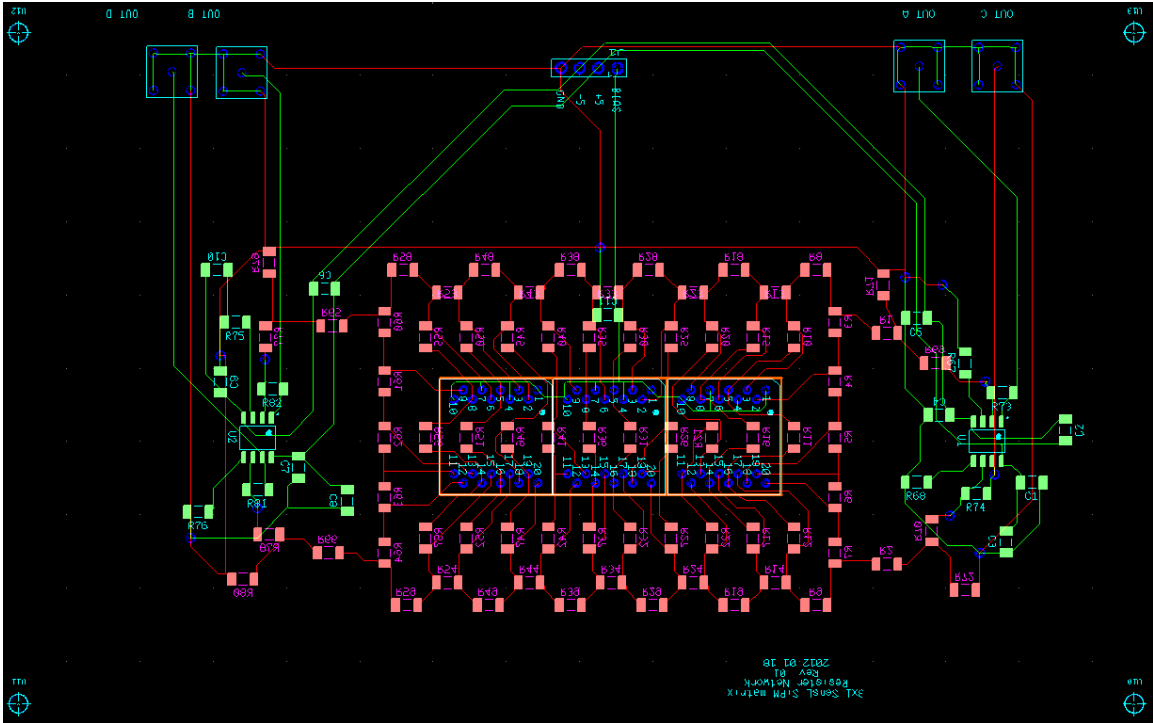
Figure 4-3 The layout of the printed circuit board drawn in Ultiboard. The colour green indicates that the components are on the top side of the board, and red the underside of the board.
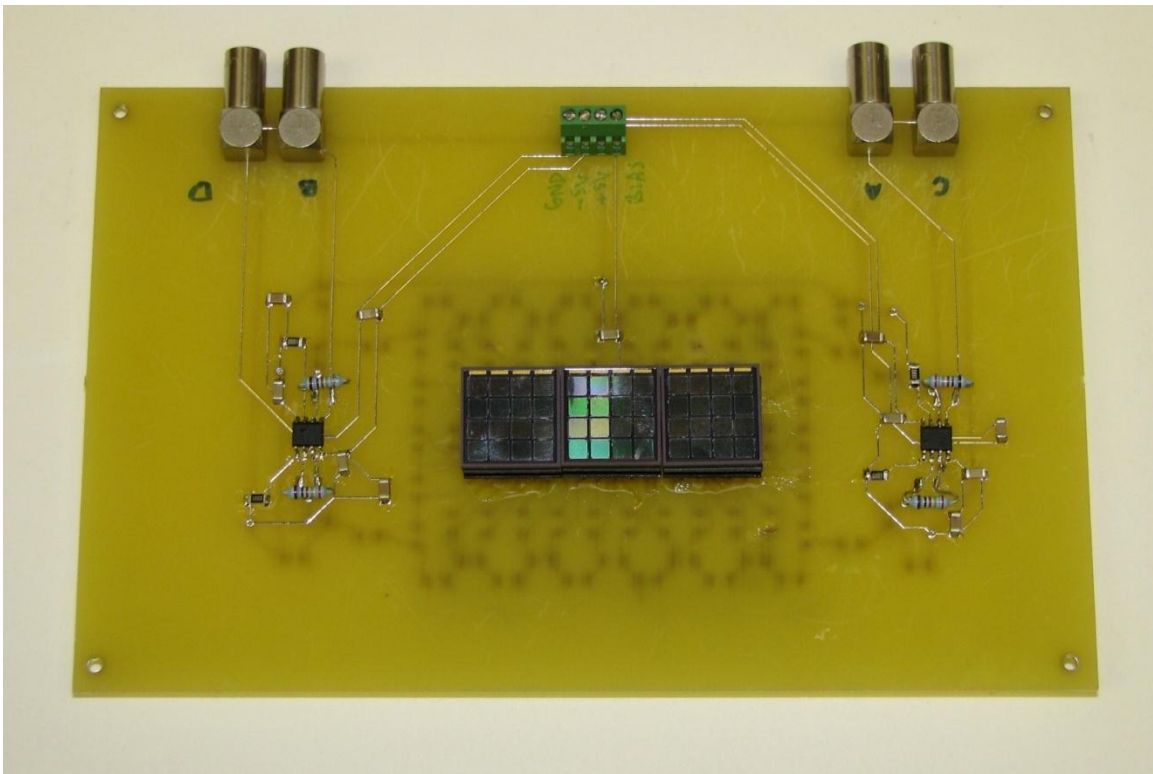
Figure 4-4 Photograph of the completed circuit board with 3 SensL SPMArray4 detectors.
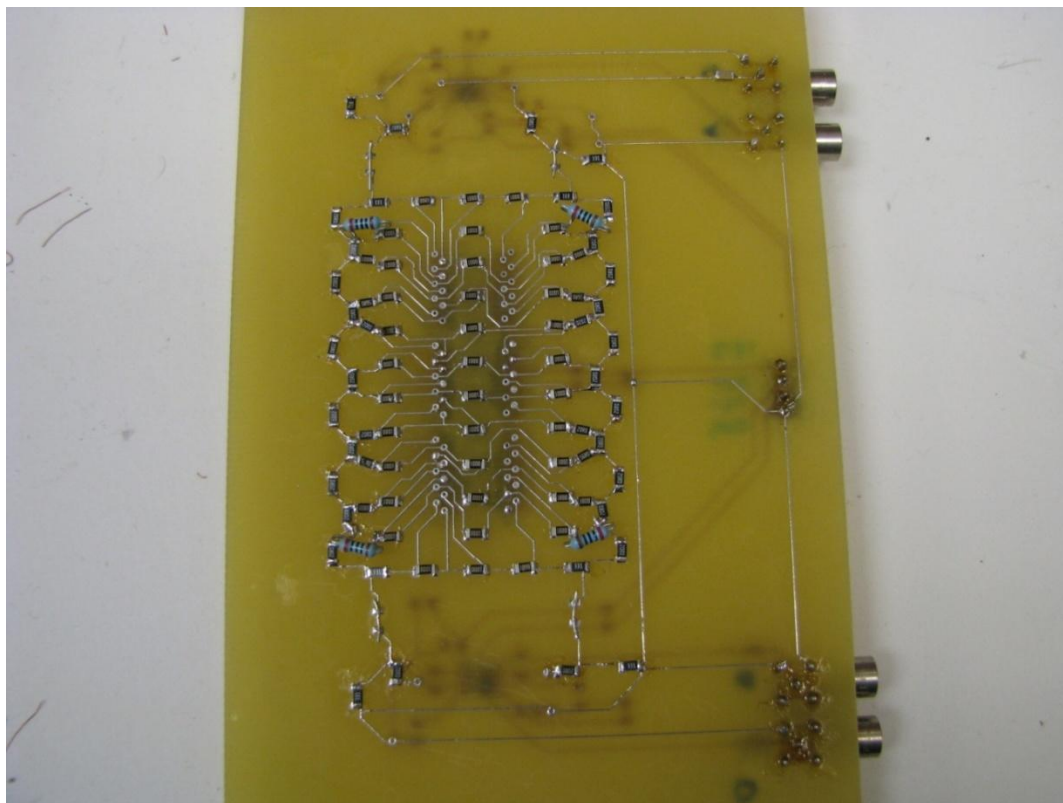
Figure 4-5 The back side of the circuit board has the resistor network.

The four outputs of the resistor network are amplified by Texas Instruments OPA2690ID op-amps (Texas Instruments, Dallas, TX) configured as inverting operational amplifiers (Figure 4-6). The amplified signals leave the multiplexing board through LEMO 00 connectors and 50Ω coaxial cables (Figure 4-7).
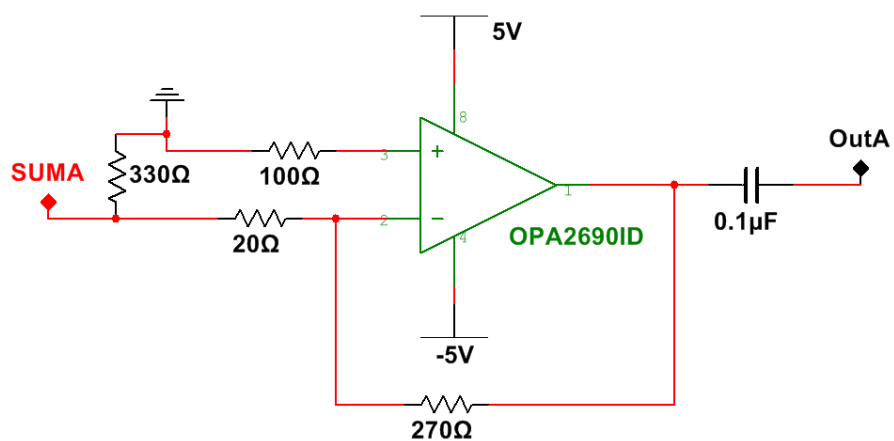
Figure 4-6 The multiplexed signals are amplified with OPA2690 op-amps configured as in this diagram.

62
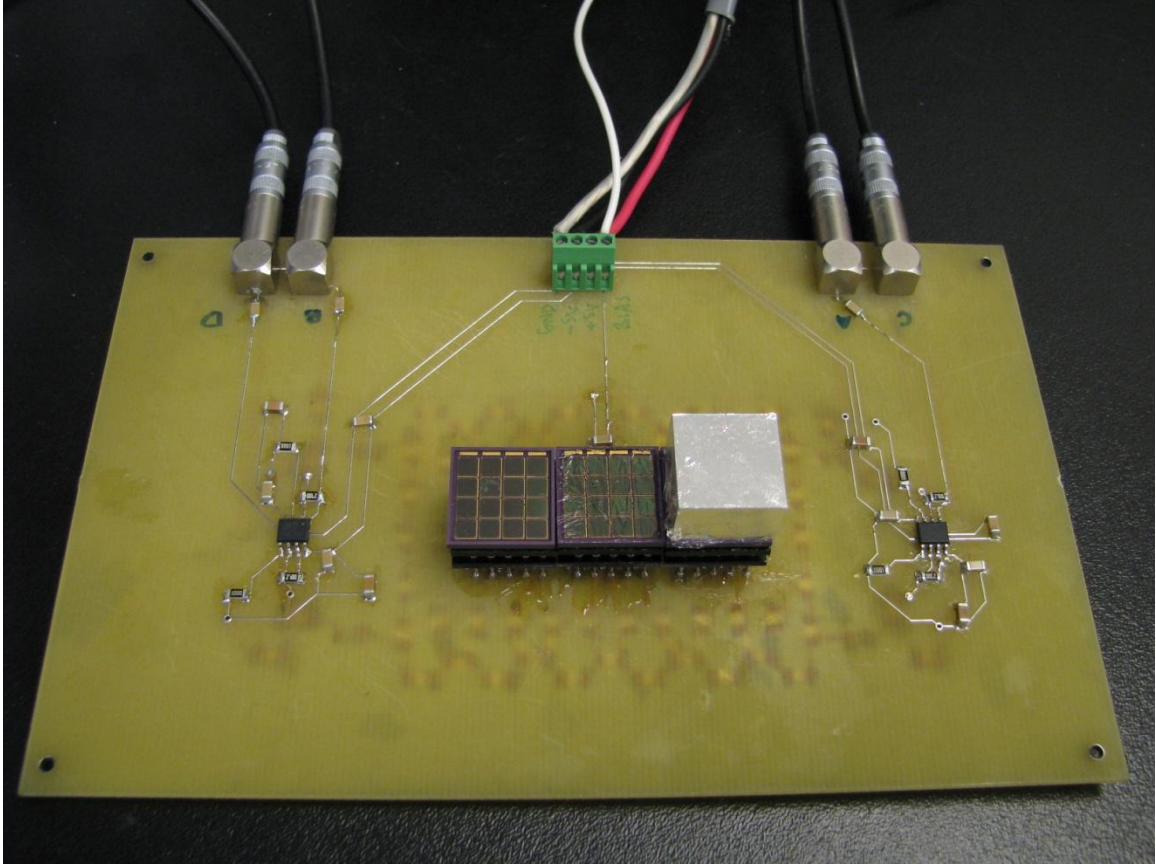
Figure 4-7 The four multiplexed signals leave the detector through coaxial cables. The +/- 5 V power for the amplifiers and the 30.2 V bias voltage for the SiPMs are provided by regular wires.

4.3   Experimental setup for measuring detector performance

4.3.1   NIM pulse processing electronics

The outputs of the multiplexing circuits are sent via 50Ω coaxial cables to Nuclear Instrumentation Module (NIM) based processing electronics. First, the four signals are input to Phillips Scientific 778 fast amplifiers (Philips Scientific, Mahwah, NJ) to split each signal into two paths, one for energy and one for timing (Figure 4-8).

The pulses in the energy path are shaped with a Mesytec MSCF-16 shaping amplifier with a 0.25 μs time constant (Mesytec, Putzbrunn, Germany). The shaped signals are

sampled and digitized at the peak of the pulse using a custom built sample-and-hold

module and a National Instruments PCI-6133 analog to digital converter card (National

Instruments, Austin, TX).

The timing path includes a Phillips Scientific 740 fan-in fan-out amplifier to sum the

four signals for input to a Phillips Scientific 715 constant fraction discriminator (CFD).
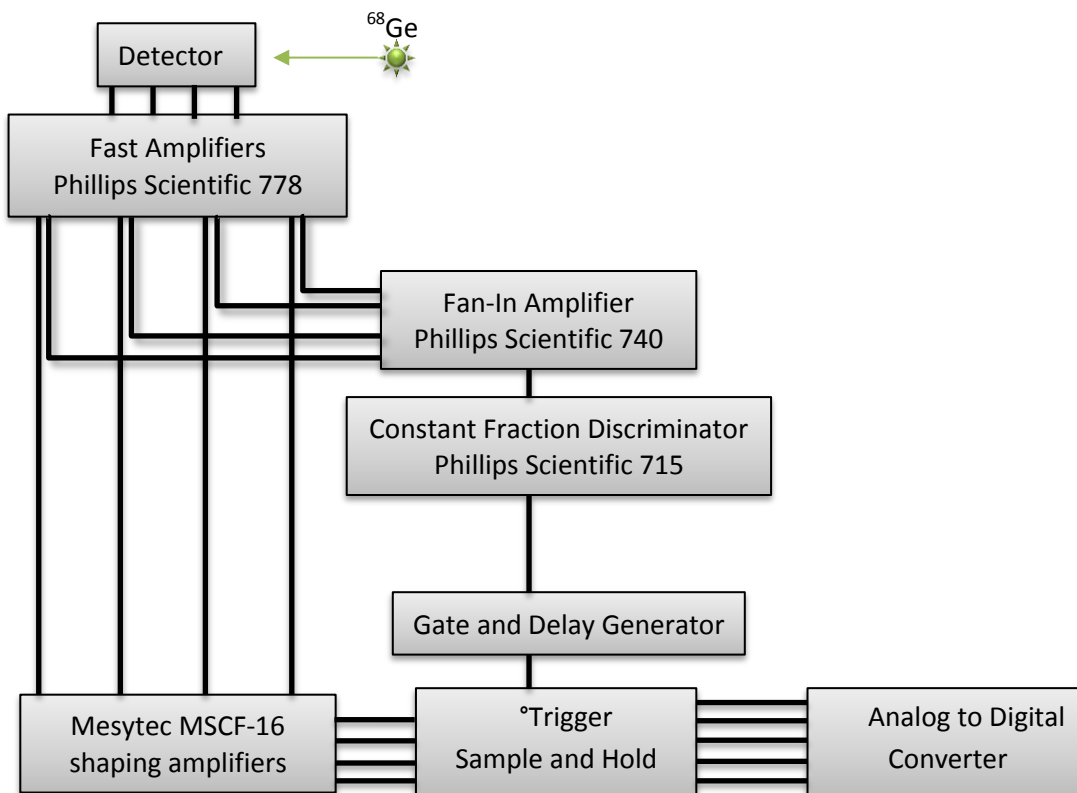
Figure 4-8 The setup of the NIM when measuring the flood histogram, energy resolution, and spatial resolution of the detector.
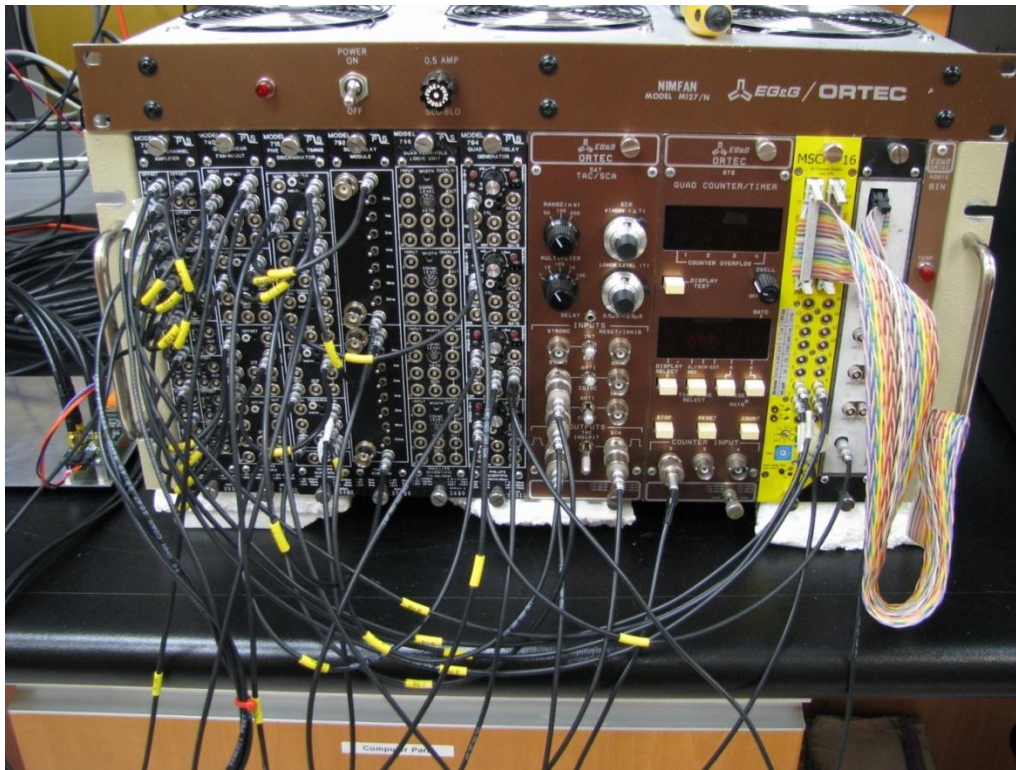
Figure 4-9 The NIM electronics and the cables connecting the modules.

4.3.2   Timing resolution measurement

The timing resolution of the detector was measured using a Scanwell Systems Timing

Probe (Scanwell Systems, Montréal, QC), which has a ^{22}Na radioactive source built in a

plastic scintillator that is coupled to a photomultiplier tube (Figure 4-10) [35]. The output

of the photomultiplier tube is input directly into another channel in the Phillips Scientific

715 CFD which uses a 0.5 ns delay line, and the resulting trigger is used as the START

signal for a time-to-amplitude converter and single channel analyzer (TAC/SCA) (either

an Ortec 467 or 567, Ortec Advanced Measurement Technology, Oak Ridge, TN). The

STOP signal to the timer is the CFD trigger based on the summed SiPM signal.
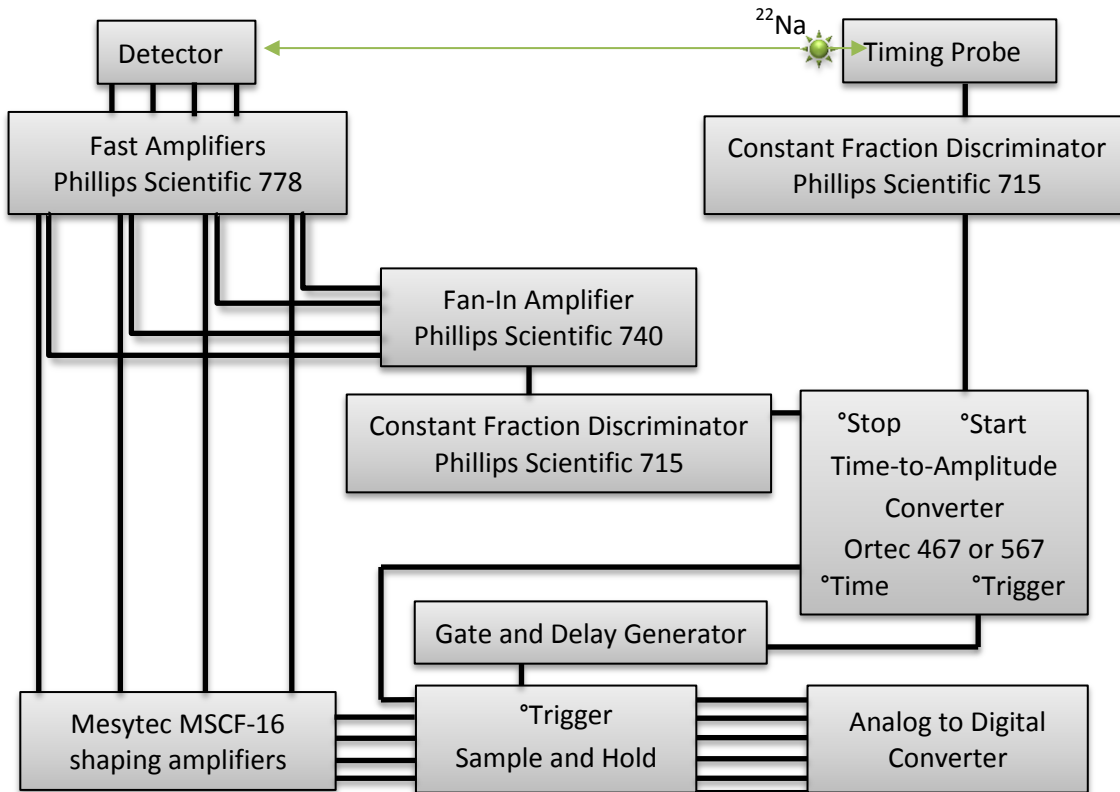
Figure 4-10 The setup of the NIM when measuring the timing resolution of the detector.

The time to amplitude converter is calibrated to give a correlation between time and the output pulse height. The calibration was done by introducing a known delay in the STOP signal line. The subsequent change in the output amplitude was then measured. This measurement provided the information on the amount of time per millivolt of output signal.

For timing resolution measurements, the time constant of the Mesytec MSCF-16 shaping amplifier was increased from 0.25 μs to either 0.5 μs or 1 μs. This was done to delay the shaped pulses enough to make them peak at the same time as the time-to-amplitude converter output pulses. One disadvantage of using a longer shaping time is that the charge integration process adds unnecessary noise into the pulse. The extra noise will worsen the energy resolution and position accuracy. Therefore, the long integration

66

time is only used when performing timing resolution measurements, where the focus is on the timing signal and not on the shaped signal.

4.3.3 Data acquisition

The flood histogram, energy and timing resolution measurements were performed using a 4×4 LYSO scintillator array (Proteus Inc., Chagrin Falls, OH) coupled with optical grease to one of the three SensL SPMArray4 detectors. The individual crystal element size matches the surface area of a single SiPM. The cross section of each crystal element is 3.17 mm $\times$ 3.17 mm, and the height is 10 mm.

There was only one 4×4 scintillator array available at the time of testing. Thus, the other two SPMArray4 detectors were left without crystals but were still plugged into their sockets (Figure 4-11). After data collection at the first position, the scintillator coupled SPMArray4 was unplugged and swapped position with another one. Then, another set of data were collected. After moving the crystal bonded SPMArray4 through the three sockets, the three list mode data sets were combined and analyzed as if it were a single measurement. One consequence of this method is that there will be no inter-crystal scatter events between the 4th and the 5th rows, and between the 8th and the 9th rows of crystals in the flood histogram.
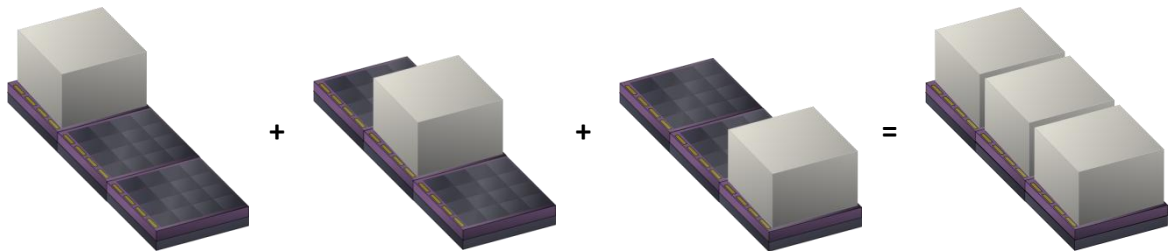
Figure 4-11 Rotating the scintillator crystal block and its SPMArray4 through the three positions and combine the collected data to form a large single data set.

4.3.4 Flood histogram generation and segmentation

Once the four signals are digitized, the position of the scintillation event and the corresponding energy are calculated as follows.

$$x = \frac{(C + D) - (A + B)}{A + B + C + D} \tag{4.1}$$

$$y = \frac{(A + C) - (B + D)}{A + B + C + D} \tag{4.2}$$

$$Energy = A + B + C + D \tag{4.3}$$

The A, B, C, and D are the amplitude of the 4 multiplexed signals. Their relative amplitudes provide information on the position of the scintillation event, and the sum of the four signals gives the amount of energy that was deposited in the scintillator.

Once the position is calculated, the events are sorted into a flood histogram. The flood histogram is then segmented with custom software in Matlab to generate energy and timing spectrum of each crystal.

4.4 Flood histogram

The flood image shows distinct crystals (Figure 4-12). The individual crystals can be resolved, indicating that it is possible to decode 48 SiPMs using just 4 signals. The flood histogram also has a rectangular shape, which will facilitate image segmentation. Having this rectangular shape means the resistor values are suitable for multiplexing a 12×4 SiPM array.
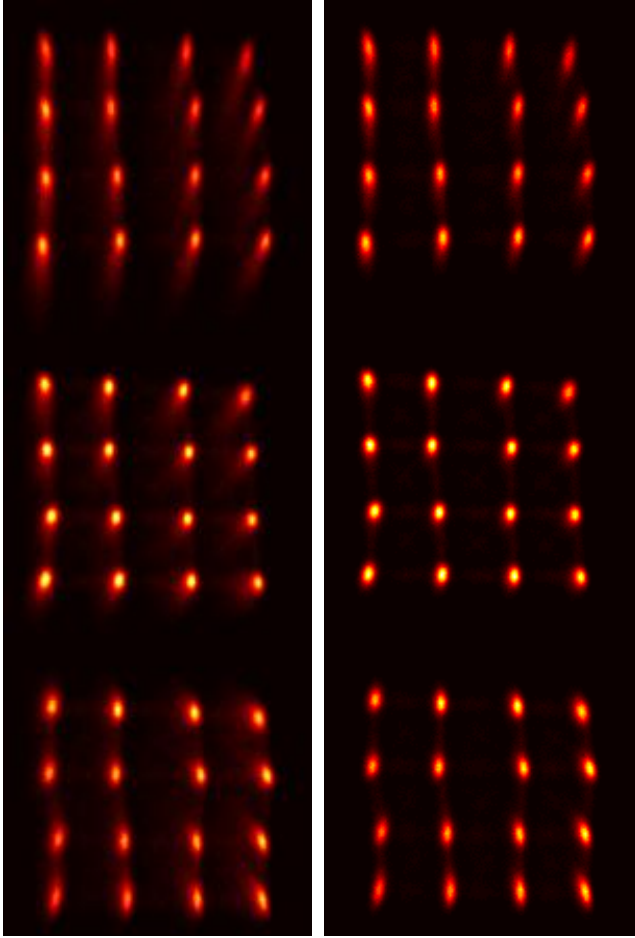
Figure 4-12 (Left) The flood histogram shows the events fall into 48 clusters, the 48 positions in the 12×4 SiPM array. (Right) The flood histogram after applying a low energy cutoff at 250 keV. The faint streaks seen in the original flood histogram are due to low energy Compton scattering events, events that occurred when only part of the 511 keV photon's energy is deposited in the crystal. Due to their low signal level, the pulses of low energy events are prone to electronic noise and statistical variation in photon sensing. Applying the energy cutoff removes those events from the flood histogram.

4.5   Energy resolution

Figure 4-13 to Figure 4-15 show the energy spectrum of ^{68}Ge measured by each

crystal in the detector. All spectra show a well defined photopeak of the 511 keV photon,

indicating the detector has a good energy resolution. When used in a PET system, the

detector will be able to tell if the annihilation photon has been scattered by the test

subject. The photopeaks are also at approximately the same position in the energy

spectrum. This uniform energy response will simplify the design of the pulse processing

electronics.
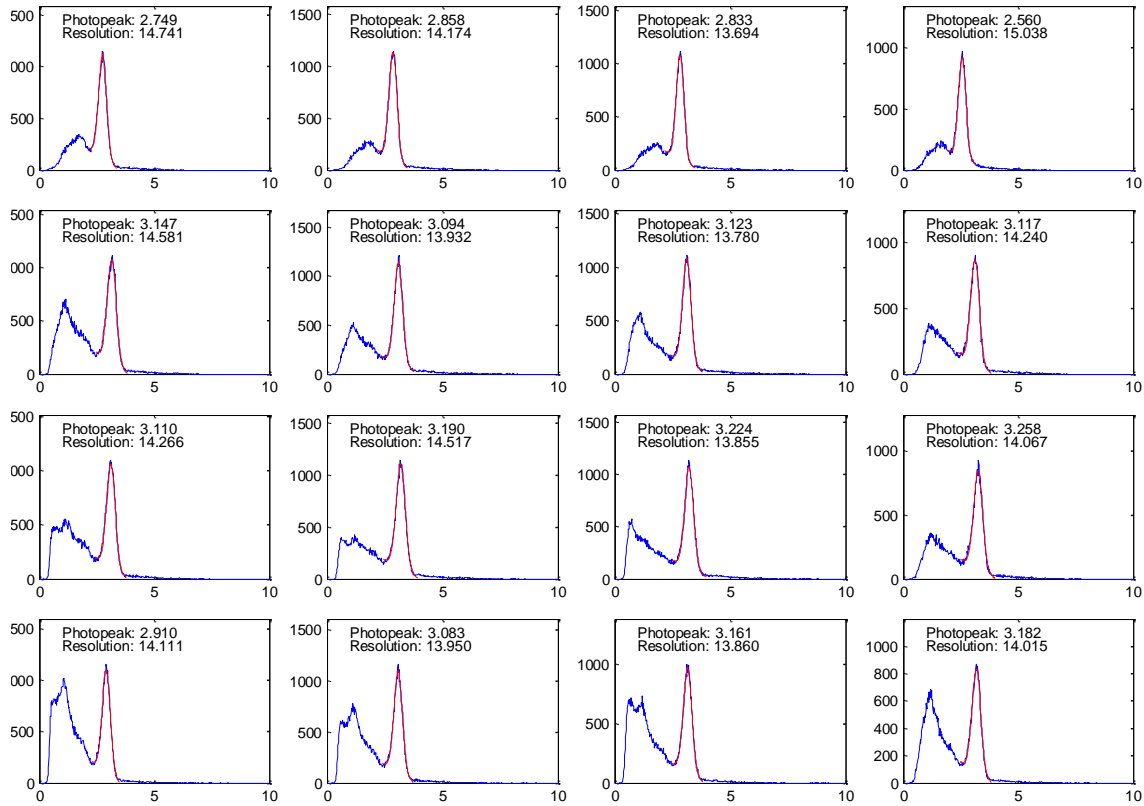
Figure 4-13 Energy spectrum of ^{68}Ge as measured by the top 4x4 crystals and SiPMs in the detector. The x-axis represents energy and is the sum of the 4 multiplexed signals. The units are in volt. The y-axis is the number of events. Energy resolutions are quoted in percentage.
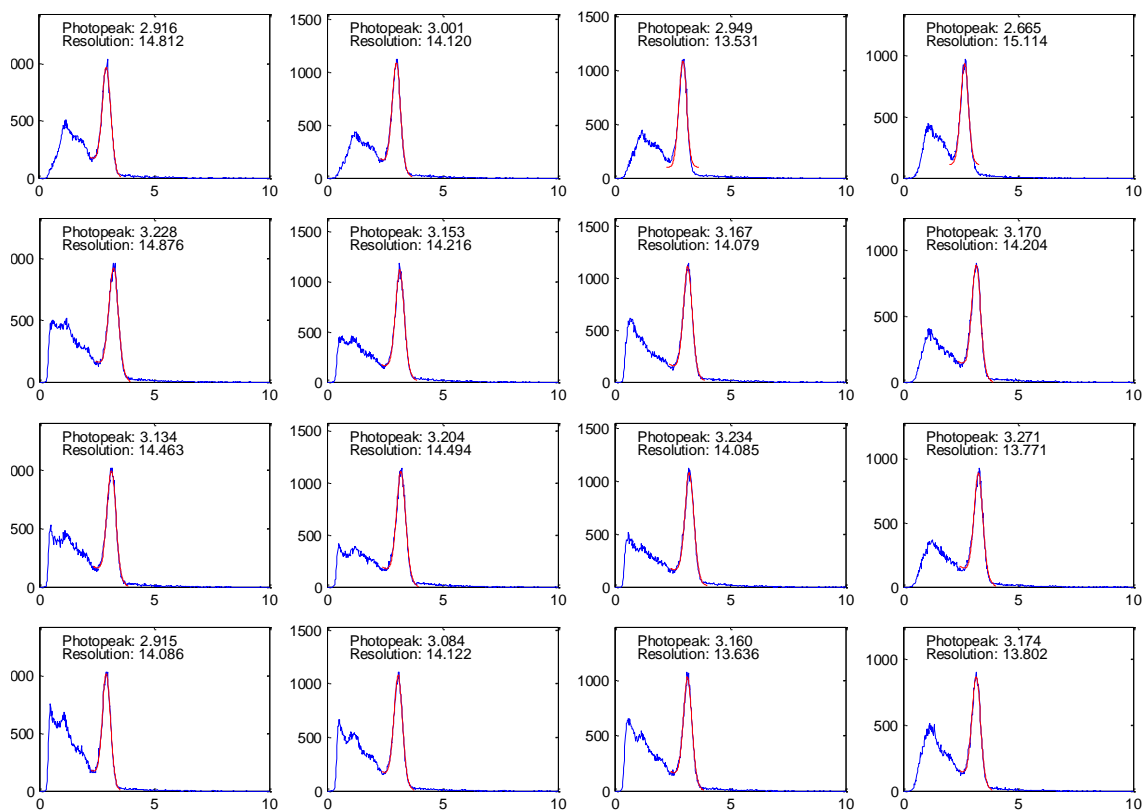
Figure 4-14 Energy spectrum of ⁶⁸Ge as measured by the middle 4x4 crystals and SiPMs in the detector.
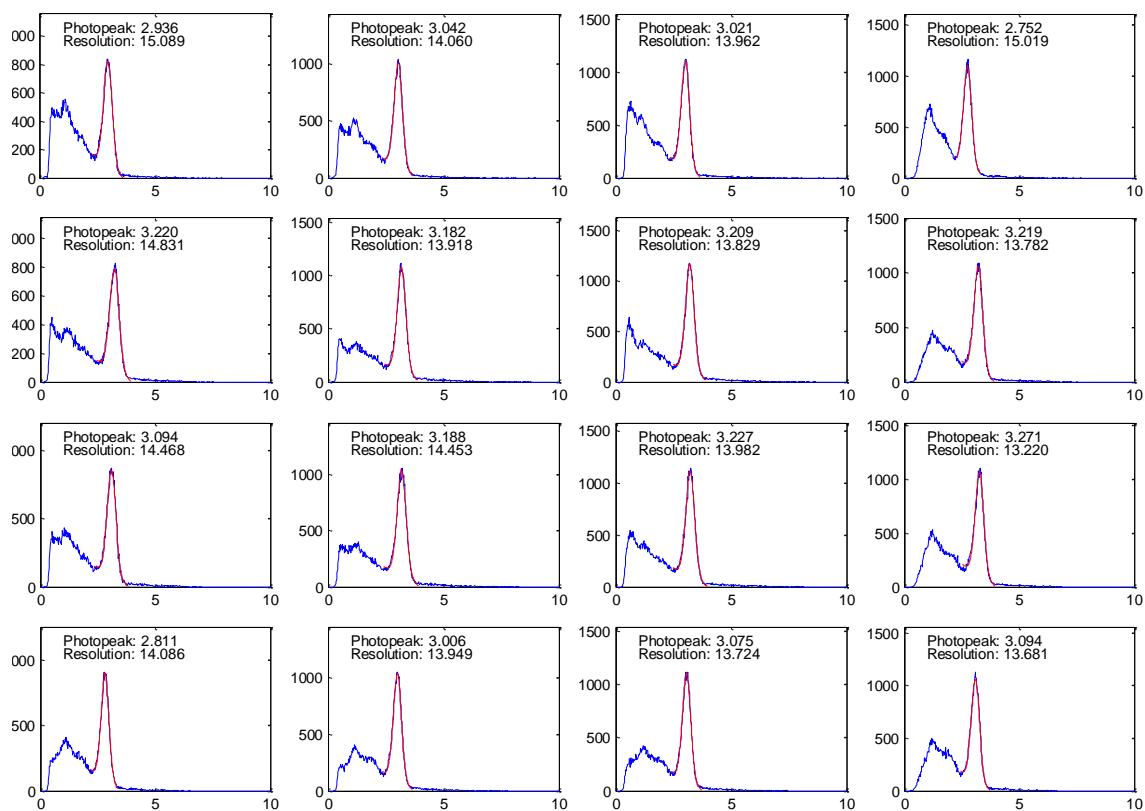
Figure 4-15 Energy spectrum of ^{68}Ge as measured by the bottom 4x4 crystals and SiPMs in the detector.

Figure 4-16 compares the position/voltage of the photopeak in the spectra. The photopeak position is quite uniform across the array with an average position of 3.1±0.2 V. Figure 4-17 shows the energy resolution of each crystal. The energy resolution is also uniform across the array with an average value of 14.2±0.4%.
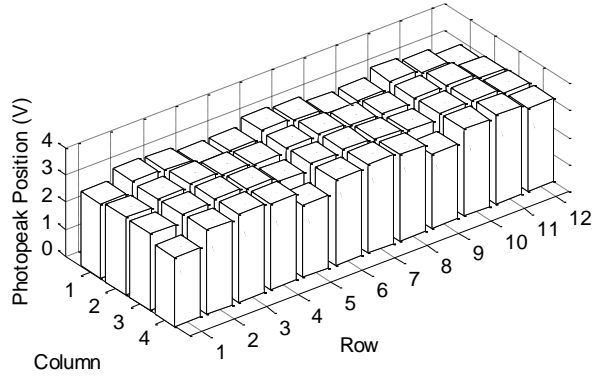
Figure 4-16 Plot of the photopeak position of 511 keV photon in the energy spectrum.
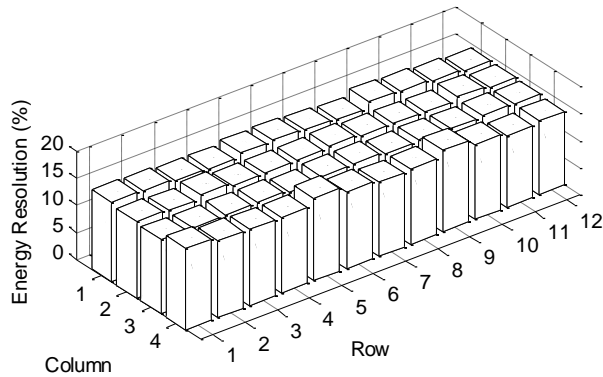
Figure 4-17 Plot of the energy resolution at 511 keV.

4.6 Timing resolution

Using the method described in section 4.3.2, we obtained the timing spectra in Figure 4-18 to Figure 4-20. These are histograms displaying the trigger time of events in each SiPM. On the individual SiPM level, a narrow peak in the histogram indicates high precision and good timing resolution for that SiPM. On the detector level, if the peaks in all histograms are located at the same position, the detector has a good timing resolution for the entire block of SiPMs. The timing resolution on the detector level is called the block timing resolution. Having a good block timing resolution allows the system to apply a single timing window to all crystals within the detector module, simplifying the system design.
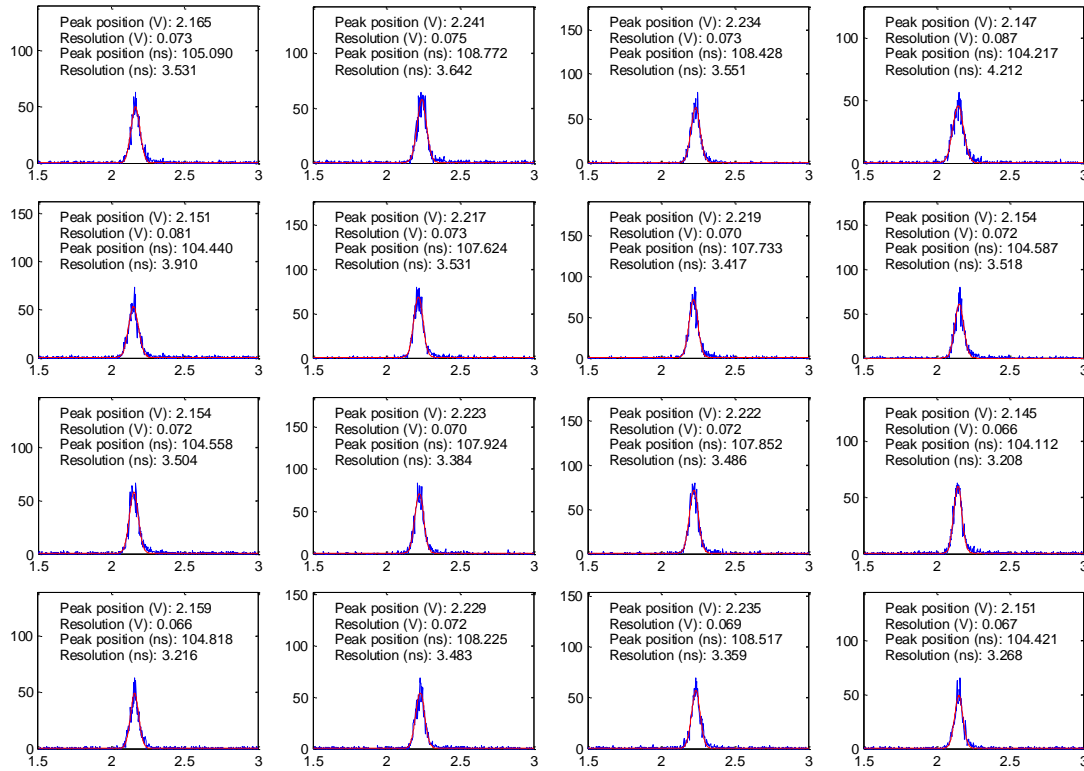
Figure 4-18 Timing spectrum of the top 4×4 crystals. The x-axis is time, measured in volts. The y-axis is the number of events. The peaks are fitted with a Gaussian curve to find the peak position and full-width-at-half-maximum. Peak position defines the trigger time of that crystal, and the full-width-at-half-maximum defines the timing resolution. Time is converted from voltage to nanoseconds using the conversion factor 20.6 mV/ns.

74
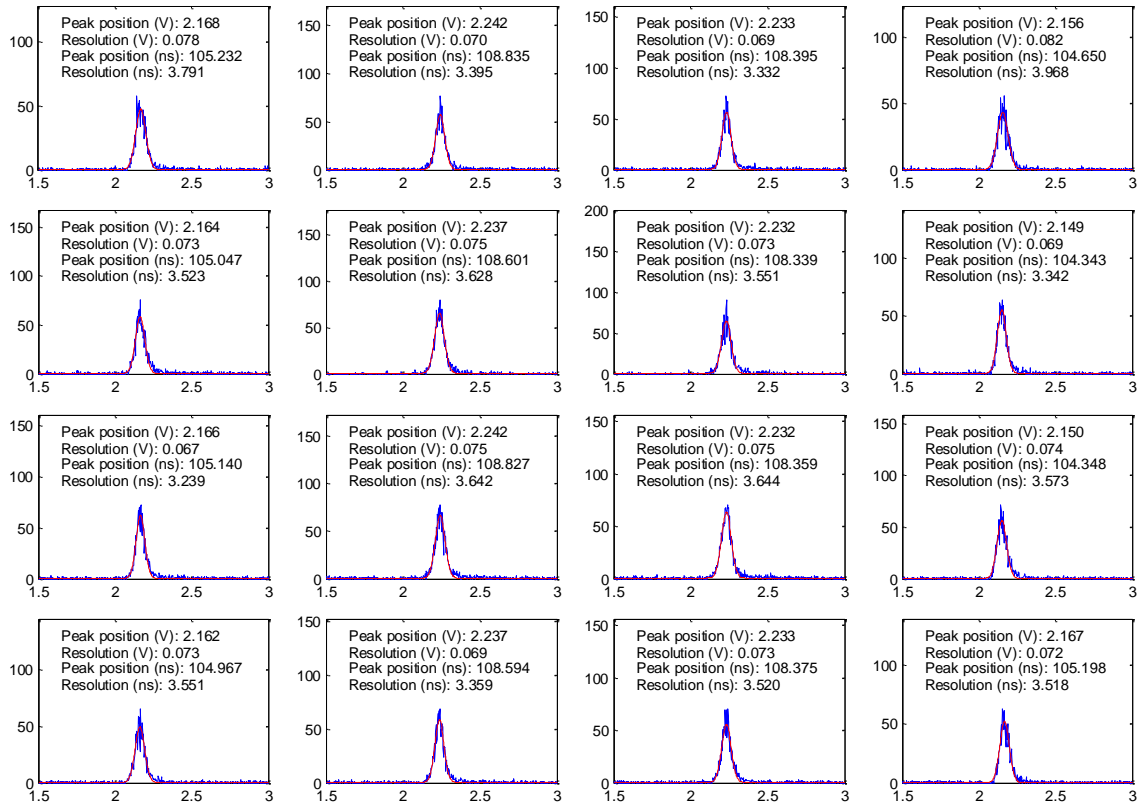
Figure 4-19 Timing spectrum of the middle 4×4 crystals.
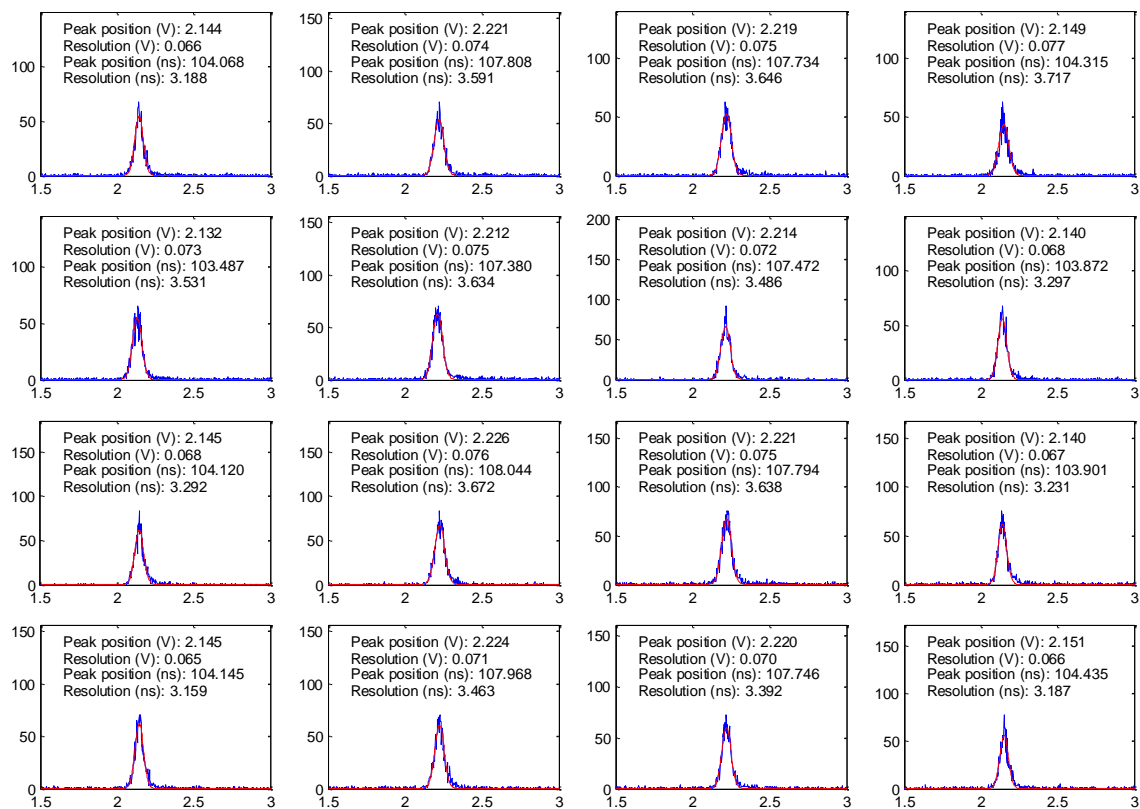
Figure 4-20 Timing spectrum of the bottom 4×4 crystals.

Figure 4-21 summarizes the peak position in a bar graph, and Figure 4-22 shows the timing resolution of every crystal. Even though the individual crystal timing resolution is on average 3.5±0.2 ns for events within the energy window 350 – 650 keV, the 3 – 4 ns difference in trigger time between different crystals degrades the collective block timing performance to 6.6 ns, which is shown in Figure 4-23.
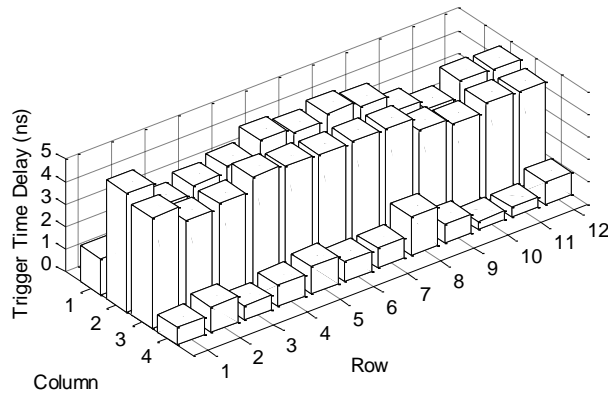
Figure 4-21 The relative position of the timing peaks. The values are relative to the crystal that has the earliest trigger time, which is artificially set to zero in this graph.
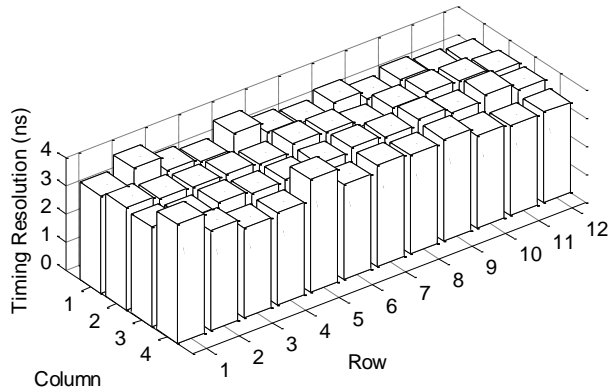
Figure 4-22 Timing resolution calculated for each crystal in the detector.
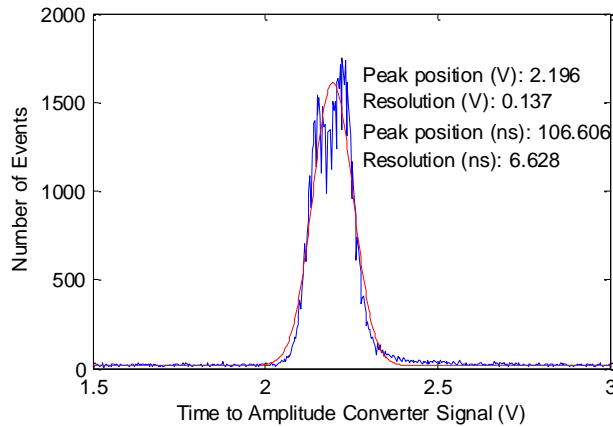
Figure 4-23 Block timing resolution of the detector. The two peaks representing the two general trigger times are evident in this plot. The red curve is a Gaussian fit of the experimental data shown in blue.

The timing performance of this detector is rather limited, with two potential factors contributing to this result. First is the slow 100 ns rise time of the pulse as shown in Figure 4-24. A pulse with a steeper rise would give a better timing resolution. The slow rise of the pulse is due to the coupling of the SiPM capacitance to the resistor network and the limited bandwidth of the amplifiers. The capacitance of a SiPM can be several hundred picofarads. This capacitance will combine with the resistors in the charge division network to form a time constant approximately several tens of nanoseconds. The bandwidth of the amplifier will also have an impact on the timing resolution of the detector, as shown by Wang [36]. The bandwidth for this circuit is estimated to be around 22MHz. This low bandwidth will eliminate high frequency components of the pulse and thus increase the pulse rise time.

Secondly, the SiPMs also exhibit two categories of trigger time. The pulses from SiPMs that reside in the inner two columns trigger approximately 3 – 4 ns later than those from SiPMs that sit in the left and right most columns (Figure 4-21). The delayed trigger

78

of pulses from the inner SiPMs is probably due to the extra resistors and the intrinsic

SiPM capacitance that these pulses need to go through. This delay contributes to the large

6.6 ns block timing resolution of the detector. Otherwise, the average timing resolution

for all 48 crystals is 3.5±0.2 ns if calculated individually.
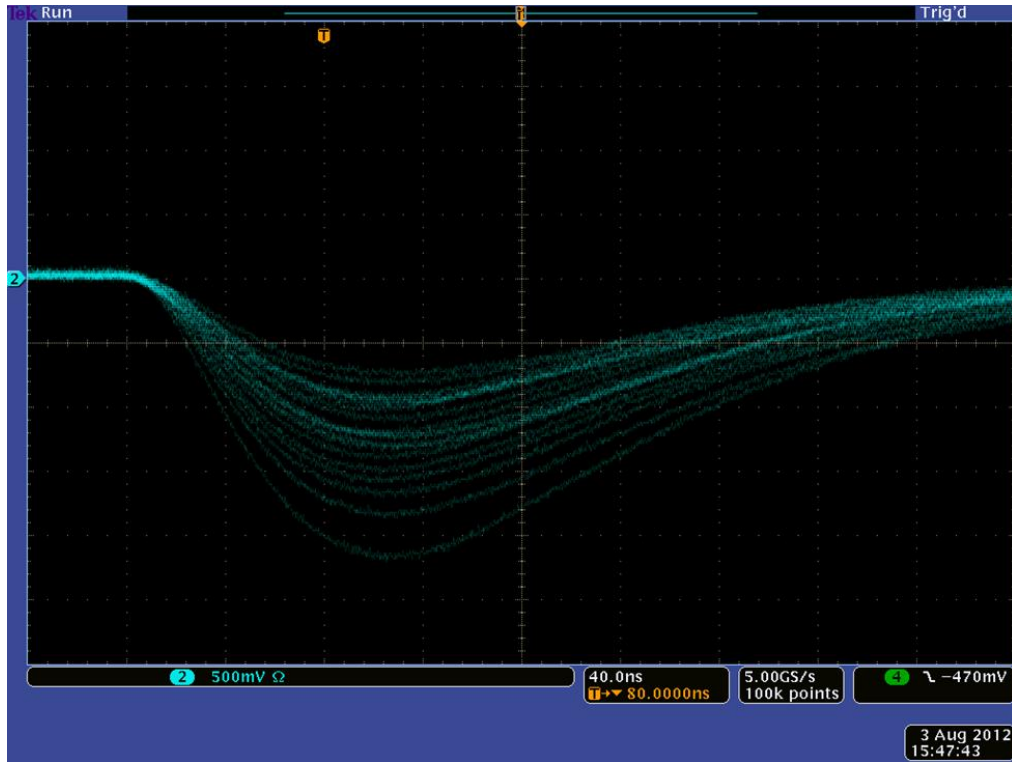
Figure 4-24 A screenshot of the oscilloscope showing the sum of four output channels from the fan-in amplifier, and this is the signal that goes to the constant fraction discriminator (CFD). The CFD produces at its output a trigger pulse when the input pulse reaches a certain fraction of its maximum amplitude. Although the pulses shown here have a negative polarity, it is customary to call the leading edge the 'rising' edge, and the tail part the 'falling' edge.

4.7 Effect of multiplexing multiple SiPMs on resolving small crystals

4.7.1 Introduction

The crystals in the 4×4 scintillator array can be resolved easily, as was seen in Figure

4-12. However, to make a gamma ray detector with better spatial resolution, an array

with smaller crystals will need to be used. A potential problem with using smaller crystals is that the centre to centre spacing between crystals will be smaller. Therefore, light from adjacent crystals may have similar light spread patterns on the SiPM array below. As a result, the detector may not be able to distinguish events from adjacent crystals. In this situation, the flood histogram will display clusters that are merged.

Previous work in our lab has shown that a 4×4 SiPM array with a similar multiplexing circuit could resolve crystals smaller than 2 mm [34]. However, the amount of dark current noise from a 12×4 array of SiPMs will be larger than the noise from a 4×4 array. Any noise in the multiplexed signals will mask the subtle difference in amplitude between signals from adjacent crystals. In this section, the effect of this noise on crystal resolvability is examined.

4.7.2 Methods

The test was carried out as follows. We started by plugging only one SPMArray4 into the multiplexing circuit. Then we put in the other two SPMArray4 detectors one by one to see if the flood histogram changes as a result of the presence of these additional SiPMs. In this test, we used a 10×10 LYSO scintillator array with an element size of 1.5 mm $\times$ 1.5 mm $\times$ 10 mm. The 10×10 crystal array was chosen instead of the 4×4 array because the change in flood histogram will be more noticeable with smaller crystals. The 511 keV photon source for this part of the experiment was [68]Ge.

4.7.3 Results

Figure 4-25 shows the flood histogram when there are 1, 2, and 3 SPMArray4 detectors in the circuit. The size of the 10×10 scintillator array covers an area of 15 mm

$\times$ 15 mm, so crystals on the edge of the array fall outside the sensitive area of the SiPM array. As a result, only an 8×8 array of crystal blobs showed up clearly in the flood histograms.
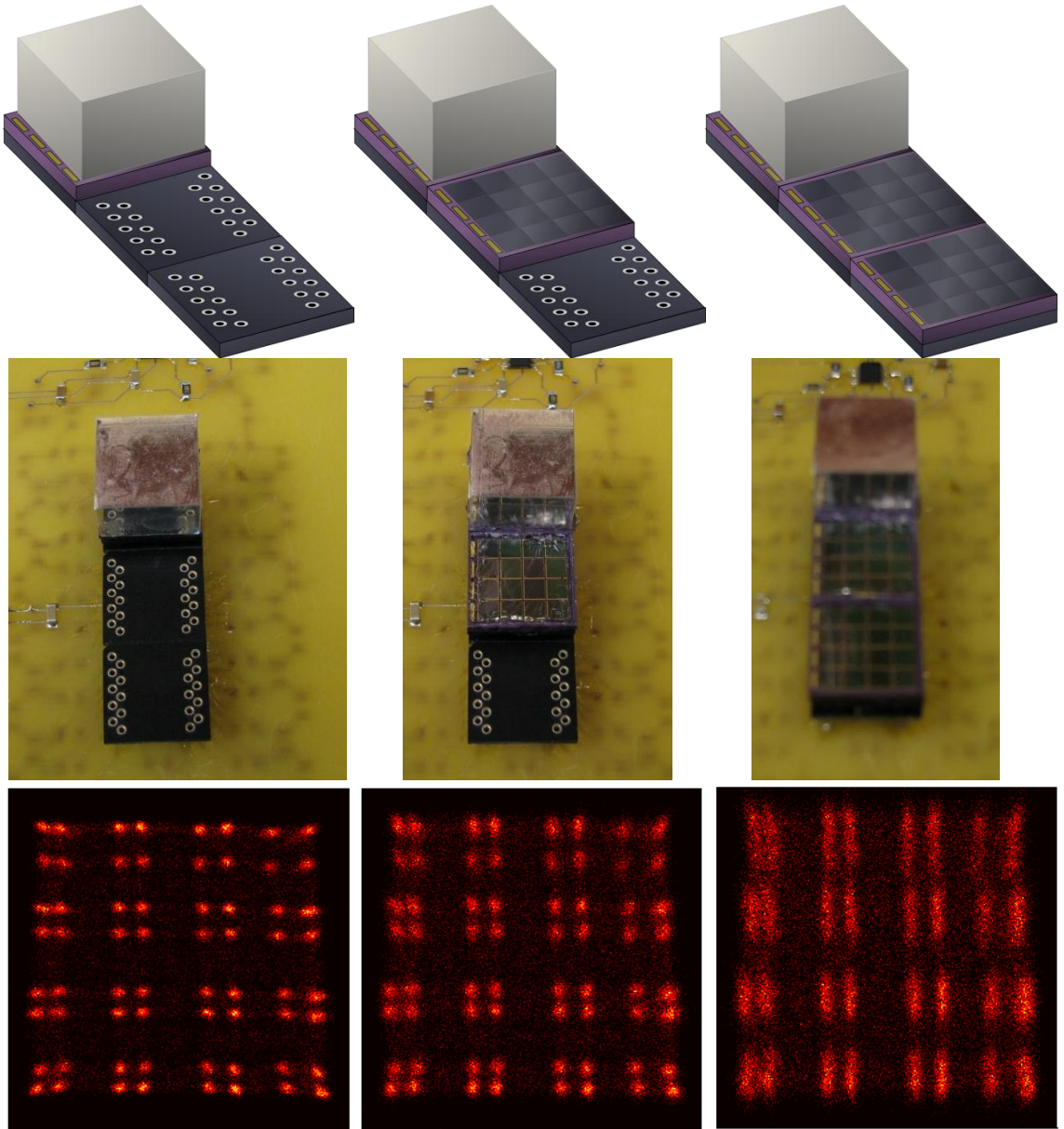
Figure 4-25 The gradual degradation in flood histogram quality when more SiPMs are added to the circuit. The low energy events are excluded from the flood histograms shown here because many of those low energy events come from the edge crystals that fall outside the sensitive area of the SPMArray4.

When there was only one SiPM array in the circuit, the crystal blobs were sharp and clear. But when the second SiPM array was added, there was a visible size increase in the blobs, meaning that the position information was less accurate. Despite this, the crystals in the flood image were still distinguishable. However, when the third SiPM array was added, the flood image exhibited a noticeable blur in the tiling direction, the vertical direction in the image. The crystal blobs were no longer distinct.

The measurements were all done in a light tight box, so the noise seen here is the dark current noise and not the stray photons from ambient light. There could be fluorescent light from materials inside the dark box. It was not clear whether the circuit board, cables, or the dark box itself fluoresces. This was not investigated and will need to be examined to see how much fluorescent light contributes to the noise seen here.

The dark current noise of all three arrays reduced the positioning accuracy of the multiplexed signal. This result tells us that it will be impractical to add additional SiPMs to make, for example, a 64×64 SiPM array. Without a mechanism to reduce the dark current noise, we can only decode scintillator arrays with large crystals. If one wants to make a large surface area detector using this multiplexing technique, the spatial resolution of the detector will be poor.

4.8   Crystals between sensors

To increase the detector sensitivity and efficiency, it is beneficial to populate the gap between SiPM arrays with scintillator crystals. However, this is only feasible if the SiPM arrays are able to read the light produced by these crystals. Reading crystals between sensors is rather simple with the multiplexing circuit. The position calculation for this

detector is relatively easy, unlike the pixel/array multiplexing used in the SensL SPMMatrix. The flood images in Figure 4-26 and Figure 4-27 were obtained by putting a 10×10 scintillator array half way between two SPMArray4 detectors. Sandwiched between the crystals and the SiPM was a piece of microscope slide serving as a light guide to diffuse light (Figure 4-28). The light guide was only necessary because there were crystals sitting above the inter-array area. Without a light guide, events from those crystals would not show up in the flood histogram.
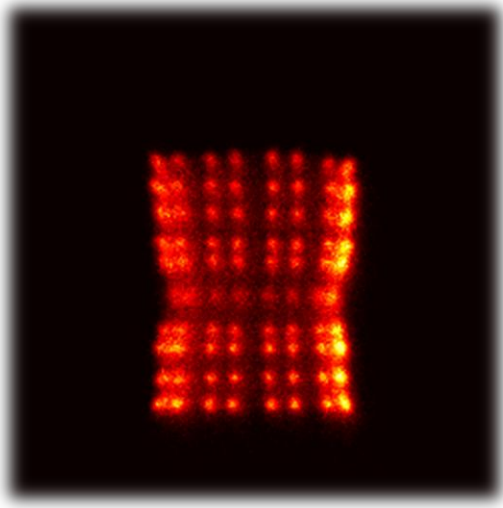
Figure 4-26 The sixth row of crystals is above the gap between two SiPM arrays.
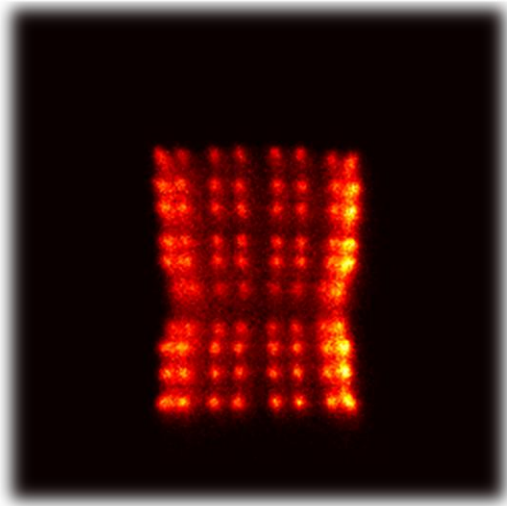
Figure 4-27 This time the sixth and the seventh rows are both above the gap.
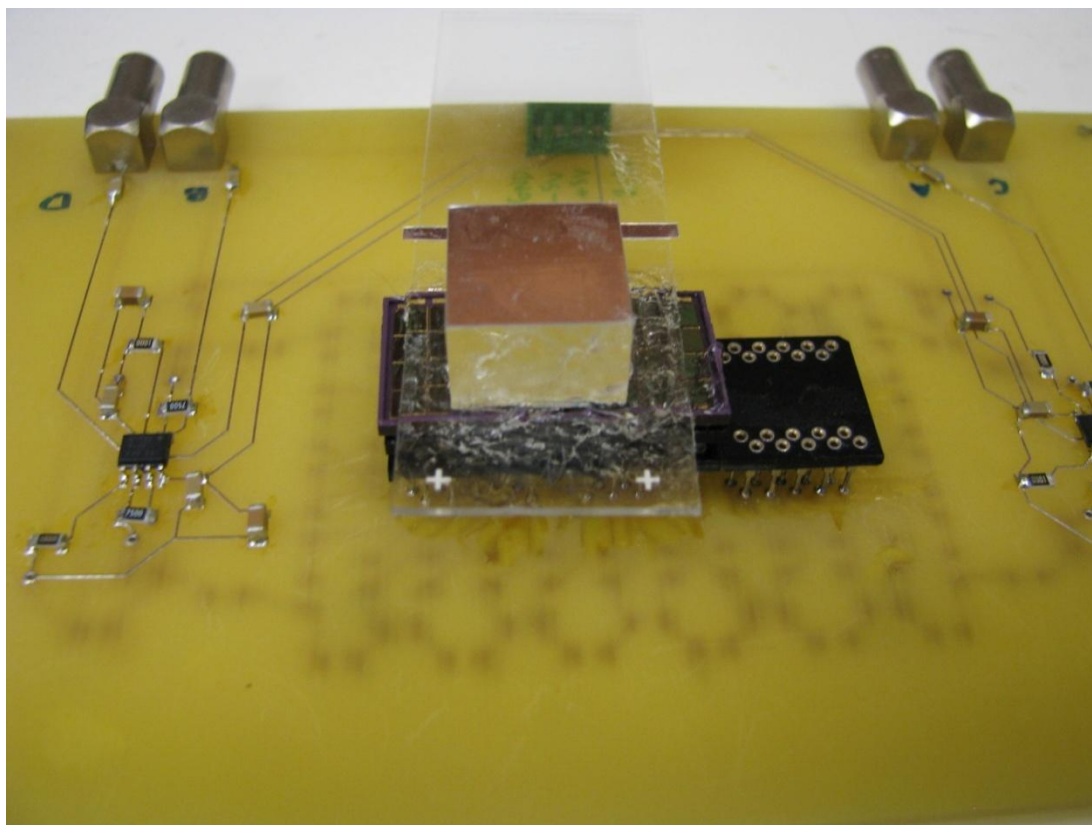
Figure 4-28 The crystal block is between two SiPM arrays. The glass diffuses scintillation light so some of it can reach the detectors.

The flood image in Figure 4-26 was segmented to get the energy spectra from the center 4 columns of crystals. For crystals in the sixth row, the photopeak is lower because it is the row where crystals are directly above the gap between detectors (Figure 4-29). The low signal amplitude is due to the difficulty in measuring light from these crystals. A better light guide design, perhaps one that directs light away from the gap, may improve light collection efficiency and signal strength. The low light collection also has an effect on energy resolution. As Figure 4-30 shows, the energy resolution is slightly poorer for crystals near or within the gap.
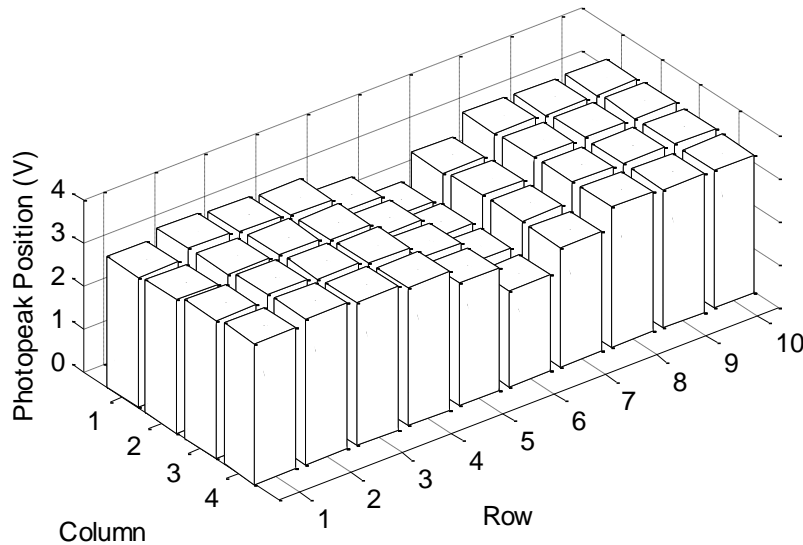
Figure 4-29 Photopeak positions of the 40 crystals in the center 4 columns of the 10 × 10 scintillator array.
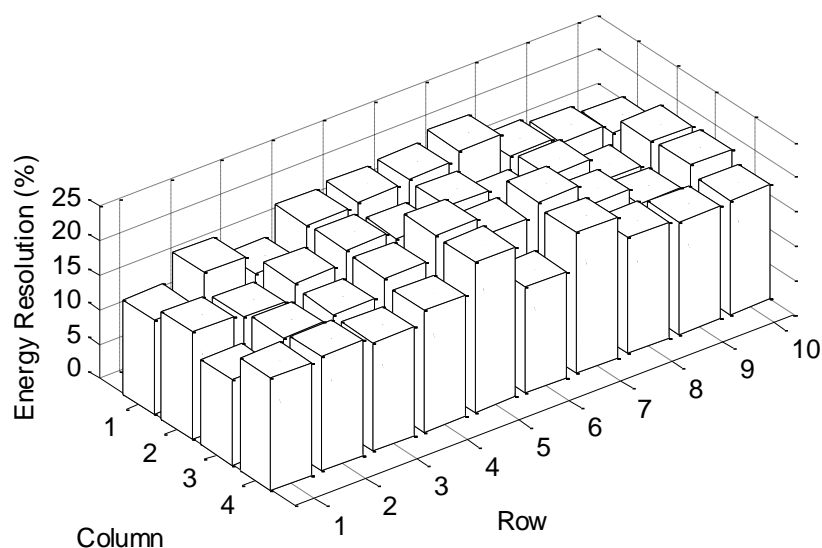
Figure 4-30 The energy resolution of the 40 crystals in the center 4 columns of the 10 × 10 scintillator array.

4.9 Summary

A gamma ray detector was designed and built. The detector employs the charge division resistor network to multiplex signals from a 12 × 4 array of SiPMs. The average energy resolution of the detector is 14.2±0.4%. The timing resolution is 3.5±0.2 ns on the individual crystal level and 6.6 ns on the detector module level. With the help of a light guide, the detector can resolve crystal elements situated in the insensitive area between the SPMArray4 detectors. In addition, a test was conducted to show that the SiPM dark current limits the number of SiPMs that can be multiplexed with the resistor network.

5   12 × 4 SiPM Array Detector with Individual SiPM Buffer Amplifiers

5.1   Introduction

In the previous detector, it was found that there was a large difference in trigger time between crystals. The large difference degraded the overall timing resolution of the detector. Therefore, another detector was designed and made to resolve this problem. The detector was tested for its energy and timing resolution.

5.2   Circuit design

This version included a non-inverting voltage feedback op-amp at each SiPM output, so the signal was amplified before being sent to the DPC circuit (Figure 5-1 and Figure 5-2). The op-amp also served to isolate the SiPM capacitance from the DPC circuit. This buffer amplifier was based on the design described by Huizenga et al. and Kolb et al. [20][37].
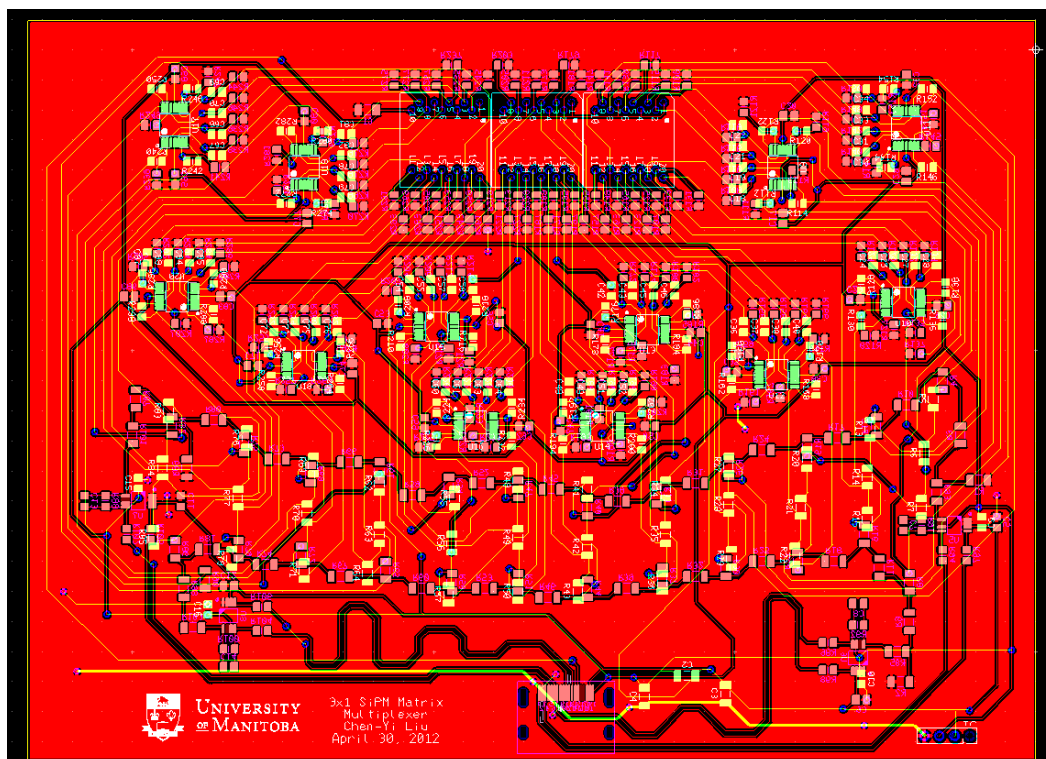
Figure 5-1 Layout of the circuit board in Ultiboard.
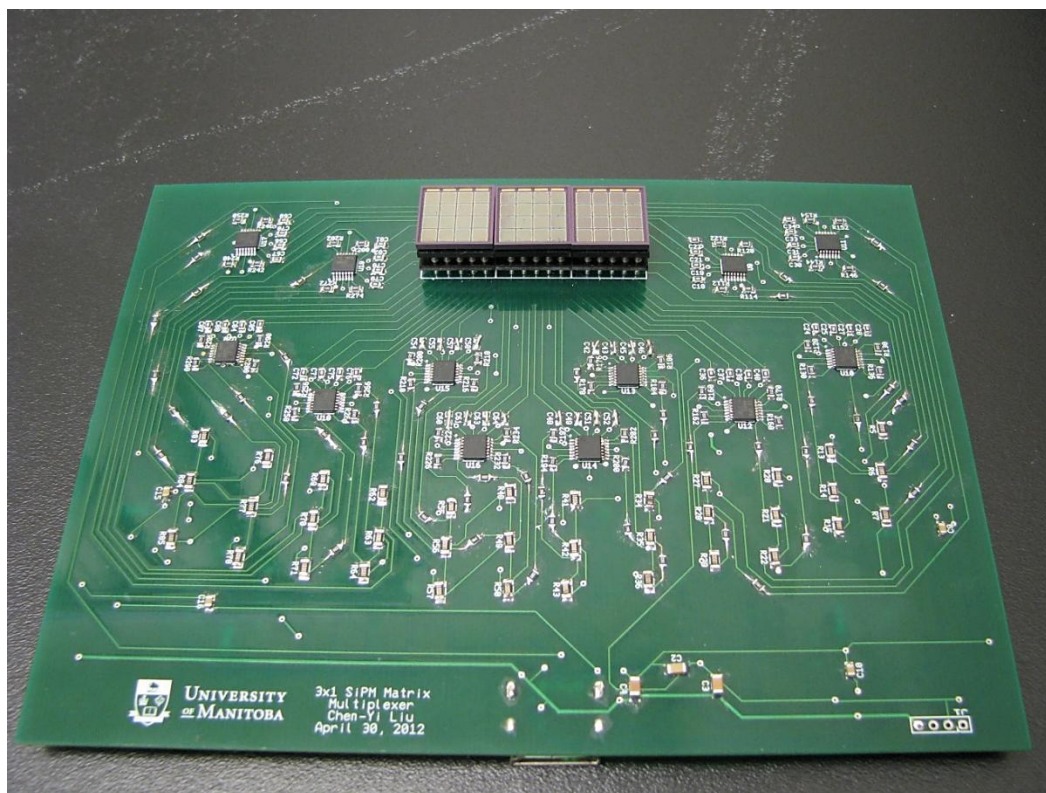
Figure 5-2 The actual circuit board. The SiPMs are on the far end of the board, followed by a cluster of operational amplifiers buffering the SiPM signals before sending them to the resistor network at the near end of the board.

88

In this circuit, the SiPM signal takes the following path. First, the output of the SiPM is connected to a 50 Ω resistor to ground (Figure 5-3). This resistor converts the output current of the SiPM to a small voltage. This voltage is in turn amplified by a voltage feedback op-amp, and the amplified pulse is then forwarded to the multiplexing circuit.

The Texas Instruments OPA4820 voltage feedback operational amplifier was chosen for its quad amplifier package. Every OPA4820 integrated circuit contains 4 op-amps. Since there is a total of 48 SiPM outputs to buffer, the circuit requires 48 op-amps. Using a high density integrated circuit such as the OPA4820 will minimize the number of electrical components on the circuit board, thus reducing the size of the detector.

The resistors in the resistor network are also modified to create a greater inter-row distance in the flood histogram between the first four and the last four rows of SiPMs (Figure 5-4). Even though this distorts the flood histogram, it makes resolving crystals in the top and bottom areas easier.
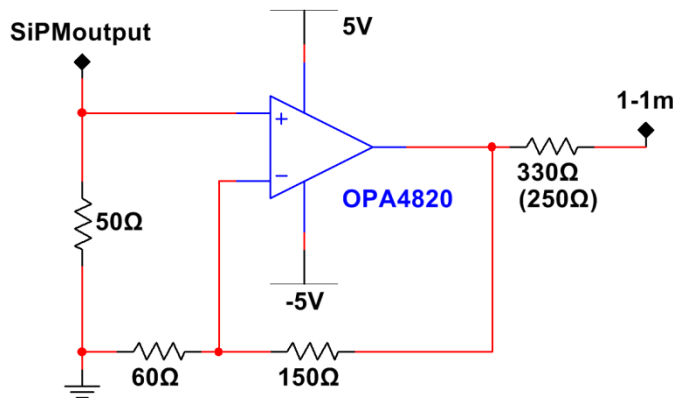
Figure 5-3 The configuration of the buffer amplifier (OPA4820, Texas Instruments, Dallas, TX) for the SiPM in the 1st row and the 1st column. The configuration for other SiPMs is the same except that for those in the 2nd and the 3rd columns, the output resistor on the amplifier is 250Ω instead of 330Ω. This change in resistance makes signal amplitude more uniform across the SiPM array.
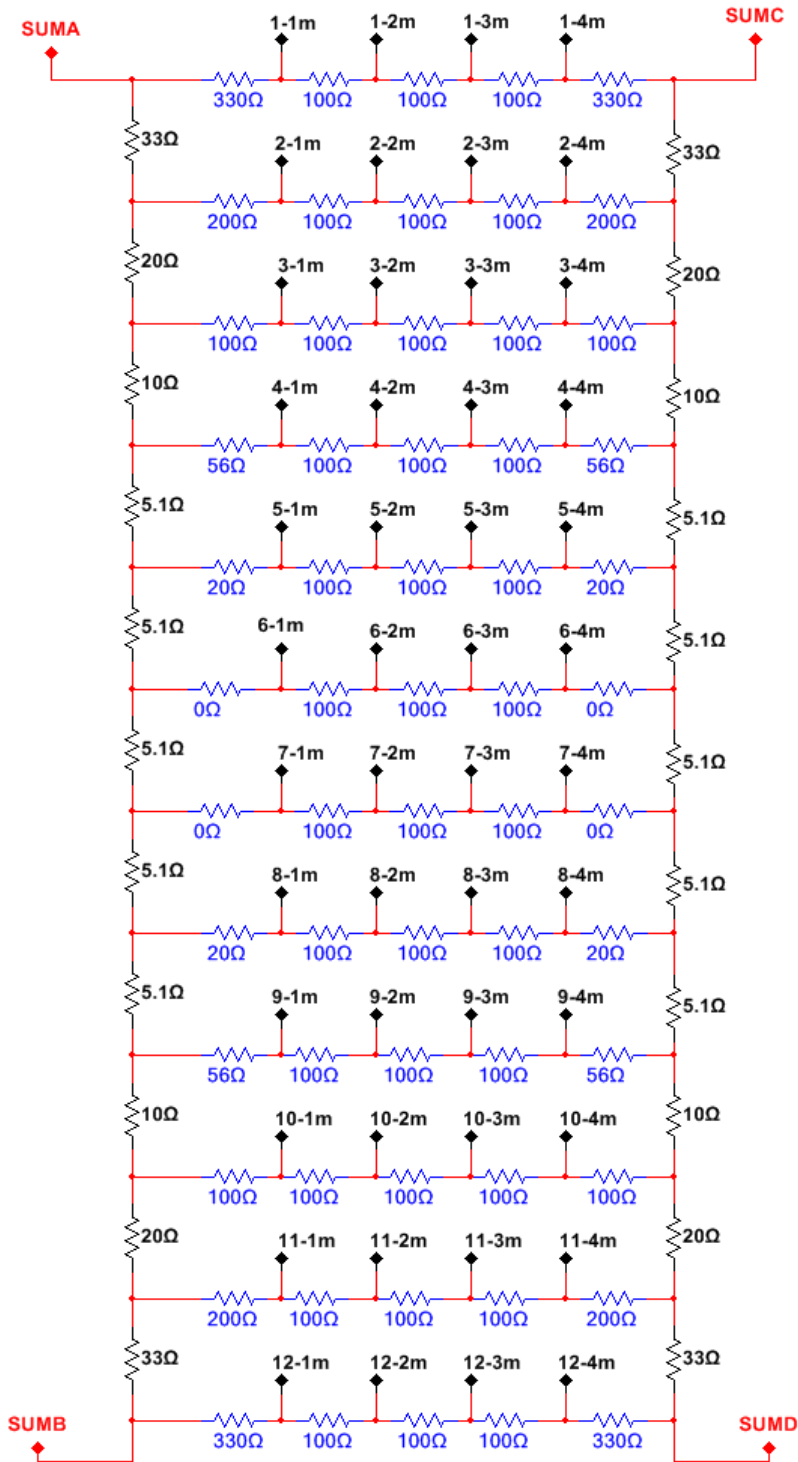
Figure 5-4 The resistor network used in this detector. The buffer amplifiers send out the amplified signals to the #-#m points in this diagram. The SUM A/B/C/D are the four outputs containing the multiplexed signals.

90
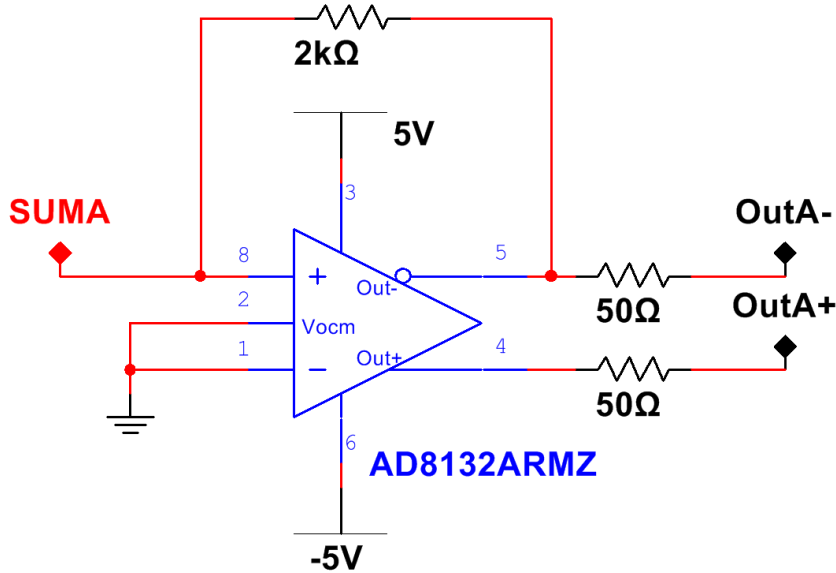
Figure 5-5 Each of the multiplexed signal is amplified with AD8132 configured as shown here.

The four multiplexed outputs are further amplified with AD8132 (Analog Devices, Norwood, MA) and then sent out via High-Definition Multimedia Interface (HDMI) cable (Figure 5-5). Another adaptor board then connects the negative end of the differential HDMI signal line to a LEMO 00 connector (Figure 5-6). The signal leaves the connector via a 50 Ω coaxial cable to the NIM electronics described in the previous chapter, in section 4.3. We used the same procedure described in section 4.3 to measure the flood histogram, energy resolution, and timing resolution of this multiplexing circuit.
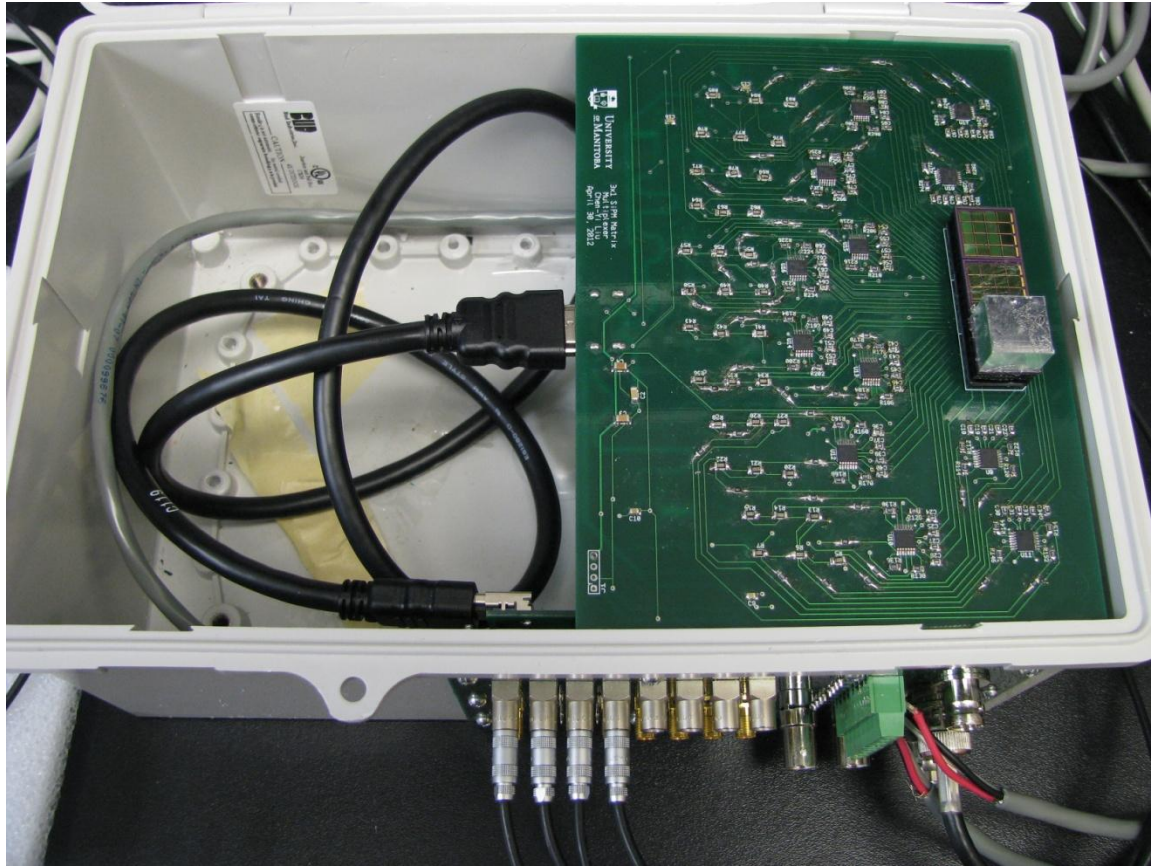
Figure 5-6 The detector is connected to an HDMI cable, which bundles the signal lines and the power lines together. A converter board mounted on the front of the dark box splits the signal lines to coaxial cables and the power lines to regular wires.

5.3 Flood histogram

The flood image in Figure 5-7 shows distinct crystals. The flood histogram is obtained with a 4×4 LYSO scintillator array. The detailed procedure of the measurement can be found in section 4.3.3. The flood histogram is fairly rectangular, which means the resistor values are suitable for multiplexing a 12×4 SiPM array.

92
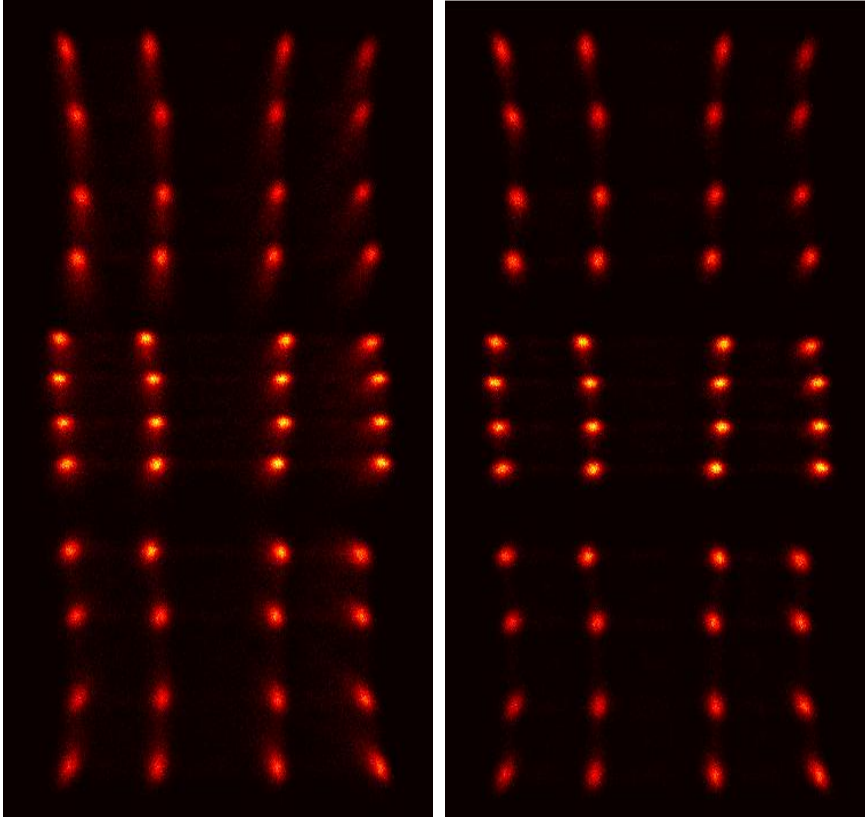
Figure 5-7 The flood histogram obtained with this detector. This detector utilizes a resistor network that expands the top and bottom four rows and compresses the middle rows. (Left) The flood histogram showing events of all energies. (Right) The flood histogram after applying a low energy cutoff at 1.41 V, which corresponds to around 250 keV.

The inter row spacing in the top and bottom four rows are wider. This is done purposefully to give more space to events from those crystals. Distortion in the flood histogram is acceptable, providing that all crystal elements can be clearly identified such as in Figure 5-7.

It was found with the previous detector that events at the top and bottom ends are more prone to noise than events in the middle are. The event clusters will grow bigger if there is more noise. A larger inter-row spacing will prevent events in neighbouring crystals from merging. The merging effect is less obvious for large crystals such as the

4×4 scintillator array, where each crystal is 3 mm in size, but the effect will be visible for small crystals, like the 1.5 mm ones in the 10×10 array described in the previous chapter.

5.4 Energy resolution

Figure 5-8 to Figure 5-10 shows the energy spectrum of ^{68}Ge measured by each crystal in the detector. All spectra show a well defined photopeak of the 511 keV photon.
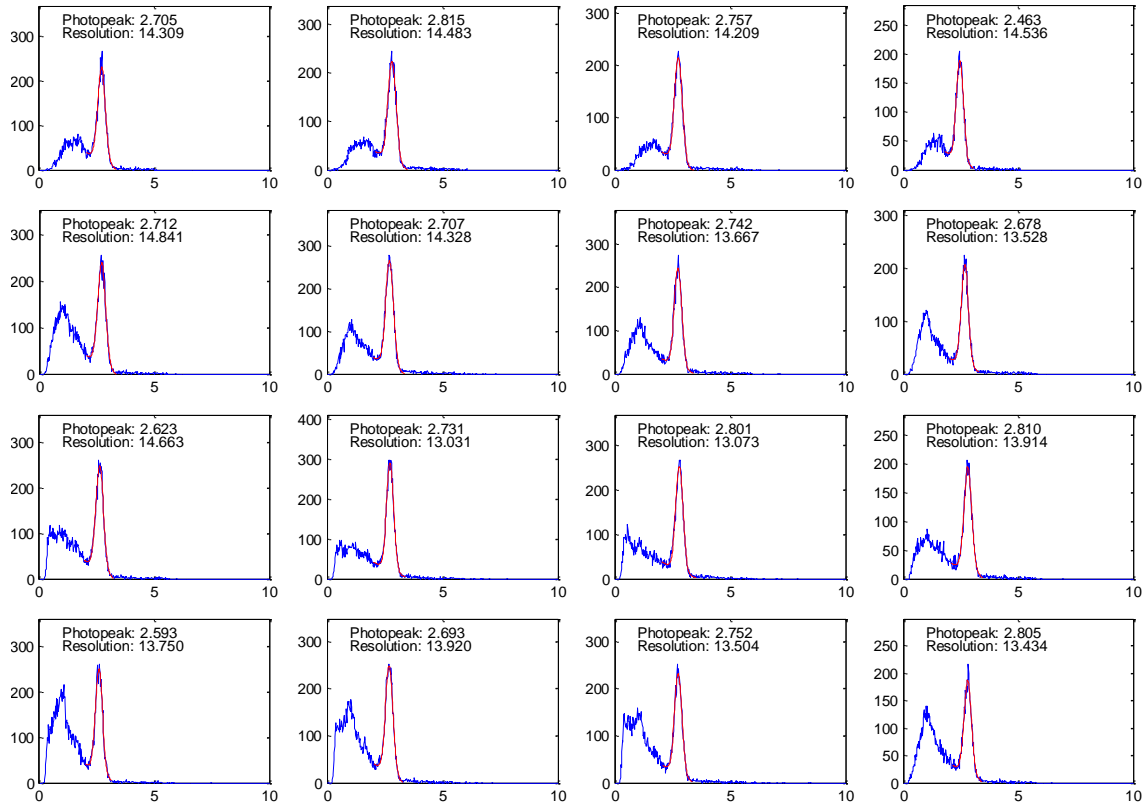
Figure 5-8 Energy spectrum of ^{68}Ge as measured by the top 4x4 crystals in the detector. The x-axis represents energy and is the sum of the 4 multiplexed signals. The units are in volts. The y-axis is the number of events.
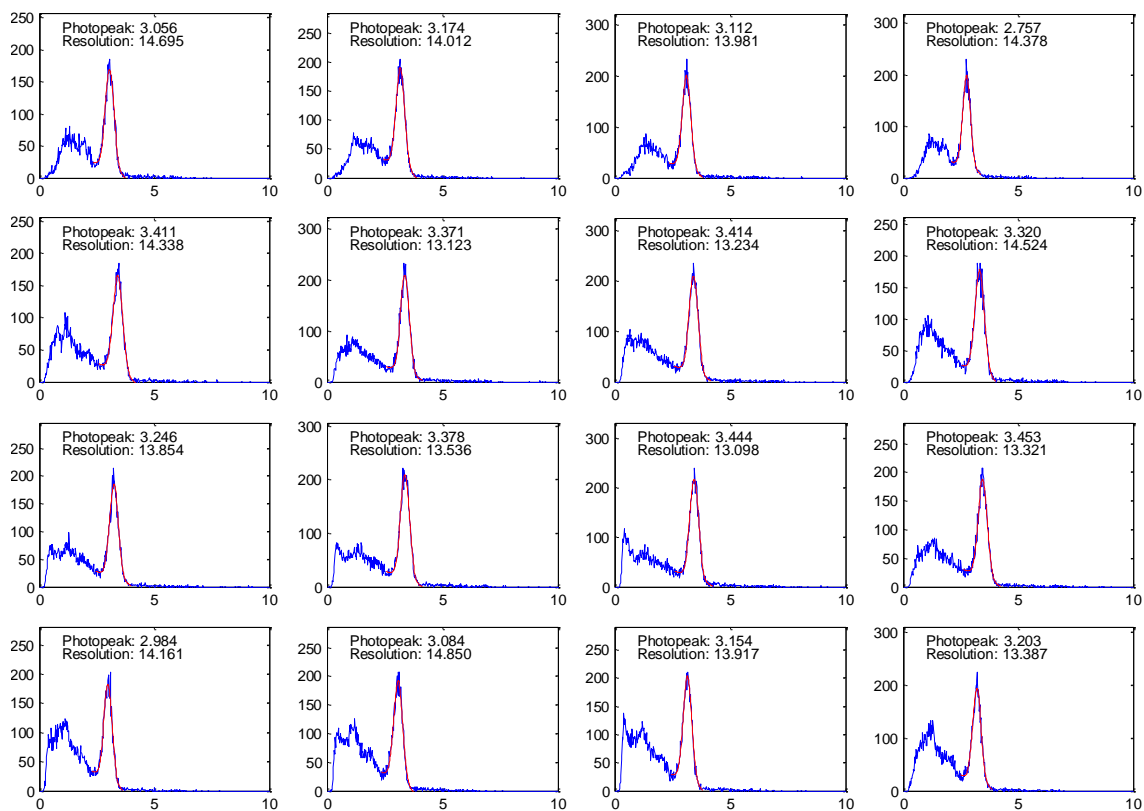
Figure 5-9 Energy spectrum of ^{68}Ge as measured by the middle 4x4 crystals in the detector.
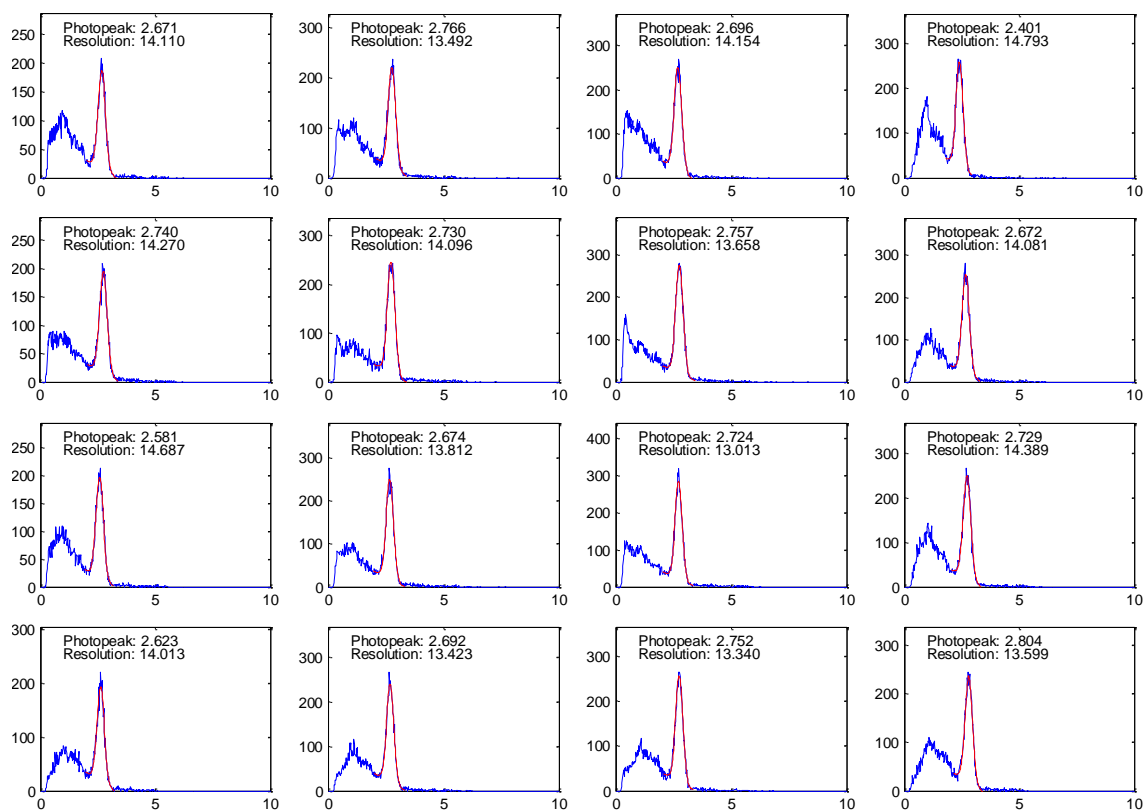
Figure 5-10 Energy spectrum of ^{68}Ge as measured by the bottom 4x4 crystals in the detector.

Figure 5-11 lists the photopeak position of all spectra. The average value is 2.9±0.3 V. Figure 5-12 lists the energy resolution of each crystal, and the average is 13.9±0.5%. The energy resolution of this detector is similar to the 14.2±0.4% achieved with the previous detector.
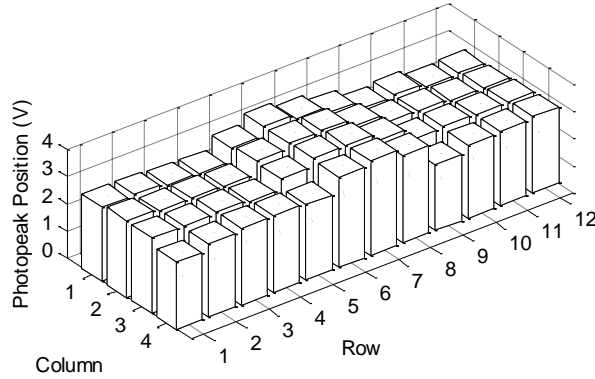
Figure 5-11 Plot of photopeak positions in the energy spectra.
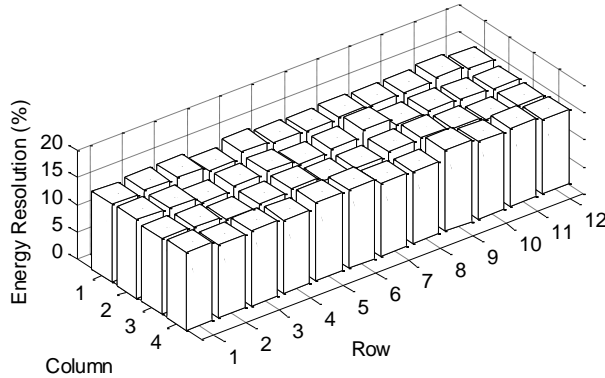
Figure 5-12 Plot of energy resolution of 511 keV photon.

5.5   Timing resolution

Figure 5-13 shows the relative trigger time for each crystal in this detector. There is less difference in trigger time than what was seen in the previous detector. The $1 - 2$ ns difference in trigger time of different SiPMs is probably caused by the uneven signal path length on the printed circuit board. The extra op-amps and the associated resistors and

capacitors made routing the signal paths a challenge in a confined space. Routing traces

in the other detector was a much simpler problem because of the smaller number of

electrical components on the board, making the trace length difference easier to

minimize.

Figure 5-14 shows the timing resolution of the crystals. The average value is 2.7±0.2

ns for events within the 350 – 650 keV energy window, slightly better than the 3.5±0.2 ns

of the previous detector.
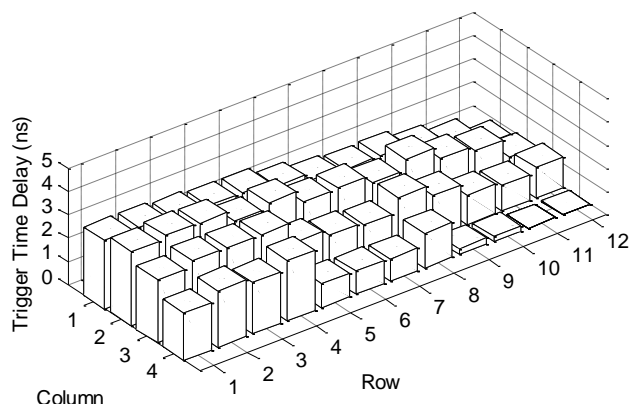
Figure 5-13 The trigger time of each crystal in the detector. The values are relative to the crystal that has the earliest arrival time, which is artificially set to zero. The values shown here are calculated using events that fall within the 350 – 650 keV energy window.
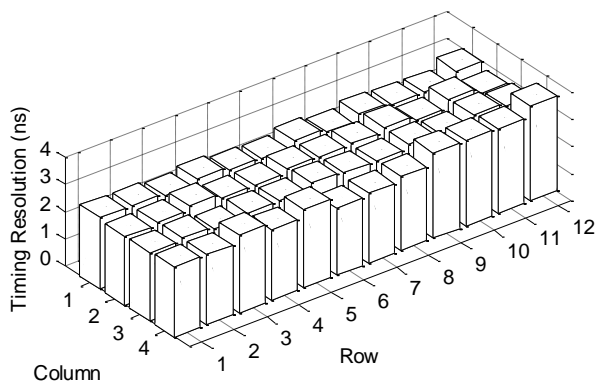
Figure 5-14 Timing resolution for the individual crystals, calculated using events in the 350 – 650 keV energy window.

98

Figure 5-15 shows the timing resolution calculated for the whole array block as a single unit. The 3.4 ns block timing resolution is now much closer to the 2.7±0.2 ns per crystal timing resolution.
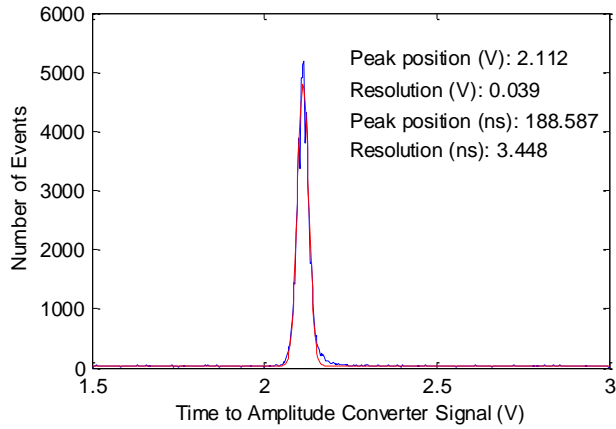
Figure 5-15 Block timing resolution of the detector, calculated with events in the 350 – 650 keV energy window. The red curve is a Gaussian fit of the experimental data shown in blue.

This detector does not have the issue of SiPM capacitance coupling to the resistor network. The op-amp at the output of each SiPM forms a barrier between the SiPM and the resistor network. As a result, the multiplexed signals have a more even trigger time. The pulses also have a shorter rise time as shown in Figure 5-16.

Figure 5-16 The sum of four output channels from the fan-in amplifier. The pulse rise time is 60 ns, shorter than the 100 ns of the previous detector.

5.6 Effect of multiplexing multiple SiPMs on resolving small crystals

The same test described in section 4.7.2 was performed on this detector as well. Figure 5-17 shows the flood histograms with different number of SiPMs in the multiplexing circuit.

Similar to the other detector, we observed that adding more SiPMs to the multiplexing circuit deteriorated the flood image. This is again due to the added dark current noise from the additional SiPMs. The noise decreases the position accuracy primarily in the vertical direction in the flood image.

100
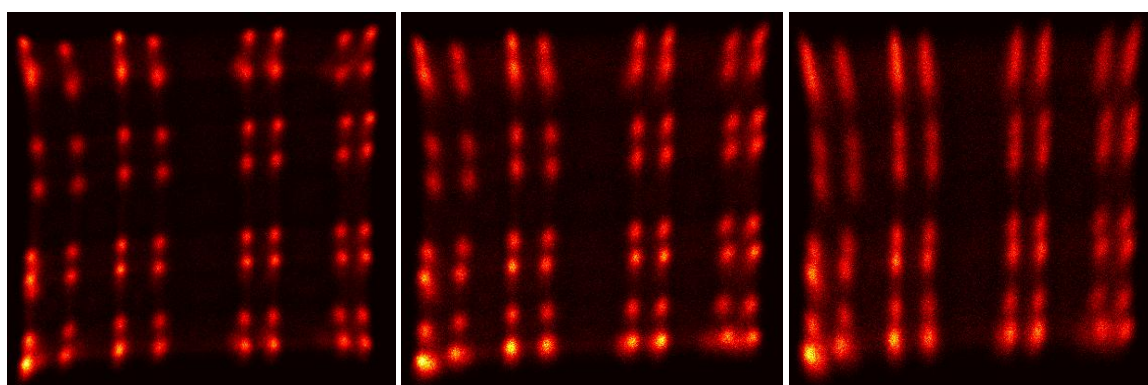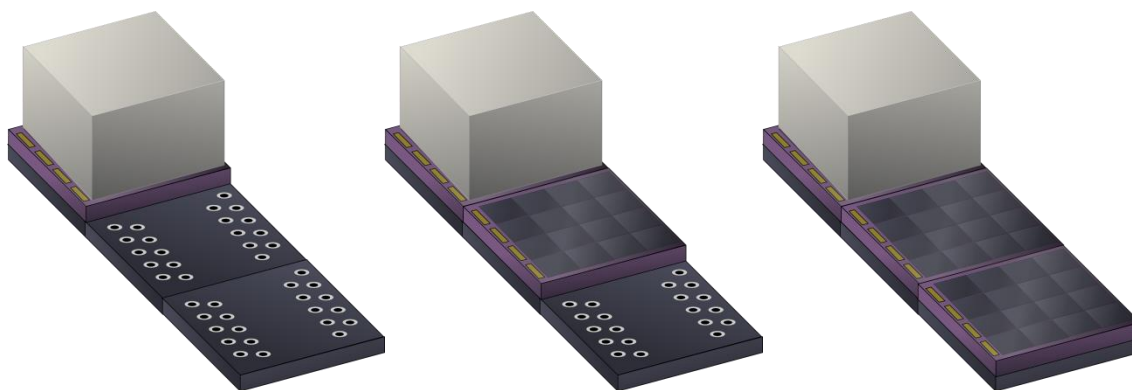
Figure 5-17 Adding SiPMs to the multiplexing circuit introduces noise that degrades the quality of a flood histogram. These flood histograms show only events that are above 350 keV to exclude events from the edge crystals.

5.7   Summary

The second version of the multiplexing circuit has a better timing resolution. The

buffer amplifiers separate the SiPM capacitance from the resistor network, allowing the

signal pulses to travel in the network without much delay. The uniform trigger time of

this detector allows a simpler design of pulse processing electronics. However, the

additional buffer amplifiers are a burden to the detector. When the detector is used in a

PET/MRI system, the amplifiers will generate heat and take up valuable space inside the

scanner bore.

6 Summary and Future Direction

6.1 Iterative positioning algorithm

An iterative positioning algorithm was developed for scintillator based gamma ray detectors. The algorithm improved the event positioning accuracy by weighting the sensor signals with a Gaussian weight function.

The iterative algorithm for event positioning can be applied to detector designs that digitize light sensors individually such as digital silicon photomultipliers. The algorithm is particularly useful for designs that cast scintillation light only on a small subset of light sensors in the array, for example, designs that couple a high density pixilated scintillator array to a digital SiPM array. By switching to the iterative algorithm from the standard center of gravity, detectors will be able to resolve smaller crystals and have higher intrinsic spatial resolution.

6.2 Multiplexing SiPM signal

The three gamma ray detectors mentioned in this thesis are all capable of multiplexing SiPM signals. The SensL SPMMatrix employs a pixel/array approach to multiplex signals from 256 SiPMs in 32 channels. This approach is difficult for reading scintillator crystals between sensors. On the other hand, the reading of crystals between sensors is relatively easy when signals are multiplexed using a resistor network approach.

Although it is not mandatory to place crystals between SiPM arrays, filling the gap with crystals improves the gamma ray sensitivity of the detector. The detector simply has a larger volume that is capable of detecting gamma rays. Filling the gap with crystals also improves the spatial sampling density of a PET system, leading to better image quality.

102

All three detectors have adequate energy resolution to be used as detectors for PET. The SPMMatrix has an energy resolution of 17.1±0.6% at 511 keV, whereas the 12×4 SiPM array multiplexed with a resistor network has an energy resolution of 13.9±0.5% when used with, and 14.2±0.4% when used without buffer amplifiers.

6.3   Buffering SiPM signal

The buffer amplifiers significantly improved the block timing resolution of the 12×4 SiPM array detector. The block timing resolution is 3.4 ns, compared with 6.6 ns without the buffer amplifiers. The improvement is likely due to the amplifiers isolating the SiPM intrinsic capacitance from the resistor network.

The per crystal timing resolution of the 12×4 SiPM array detectors is 2.7±0.2 ns with and 3.5±0.2 ns without buffer amplifiers. Using higher bandwidth amplifiers may further improve the timing resolution of these detectors.

6.4   Dark current

All three detectors have problems with dark current noise from the SiPMs. The noise reduces the detector's ability to decode small crystals, restricting the spatial resolution of the detectors to above 1.5 mm. When designing a PET detector, one will need to consider the trade-off between channel reduction and the amount of noise in the signals. Multiplexing reduces the amount of electronic components at the expense of signal clarity. Individual readout of light sensors without any multiplexing offers the best signal quality.

For detector designs that feature individual readout of light sensors, the iterative positioning algorithm solves the dark current problem by excluding sensors with low

signal to noise ratios from the position calculation. Less noise in the calculation leads to more accurate position and higher spatial resolution of the detector.

Cooling the SiPMs is a possible solution to the dark current problem. The final detector design for our PET system may feature an active cooling mechanism to reduce the amount of dark current and as a way to control the SiPM temperature.

6.5 Future direction

For the MRI compatible small animal PET system being developed in our lab, instead of a 12×4 array, we plan to multiplex an 8×4 array of SiPMs using the charge division resistor network without buffer amplifiers. This number of SiPMs yields a reasonably clear flood histogram, and at the same time, reduces the number of data channels of each detector from 32 to 4. The channel reduction ratio is not as great as that of a 12×4 array, but we will be able to use smaller crystals to build detectors with a high spatial resolution. Early measurements show that this configuration gives a 13.7±0.6% energy resolution, and 2.9±0.1 ns per crystal and 6.0 ns per block timing resolution.

The block timing performance could be improved with an additional buffer amplifier at the output of each SiPM. However, because of the space constraint inside the MRI scanner bore, we decided not to add those buffer amplifiers to our detectors. By keeping the size of the detector small, we can leave more room for the animal to be scanned. One possible way to resolve the problem in trigger time discrepancy among SiPMs is to compensate for this discrepancy in real time in the system software.

104

7 References

[1]   K. W. D. Ledingham, P. McKenna, T. McCanny, S. Shimizu, J. M. Yang, L. Robson, J. Zweit, J. M. Gillies, J. Bailey, G. N. Chimon, R. J. Clarke, D. Neely, P. a Norreys, J. L. Collier, R. P. Singhal, M. S. Wei, S. P. D. Mangles, P. Nilson, K. Krushelnick, and M. Zepf, "High power laser production of short-lived isotopes for positron emission tomography," *Journal of Physics D: Applied Physics*, vol. 37, no. 16, pp. 2341–2345, Aug. 2004.

[2]   T. Torizuka, N. Tamaki, T. Inokuma, Y. Magata, S. Sasayama, Y. Yonekura, a Tanaka, Y. Yamaoka, K. Yamamoto, and J. Konishi, "In vivo assessment of glucose metabolism in hepatocellular carcinoma with FDG-PET.," *Journal of nuclear medicine : official publication, Society of Nuclear Medicine*, vol. 36, no. 10, pp. 1811–7, Oct. 1995.

[3]   K. Yanai, J. H. Ryu, T. Watanabe, R. Iwata, T. Ido, Y. Sawai, K. Ito, and M. Itoh, "Histamine H1 receptor occupancy in human brains after single oral doses of histamine H1 antagonists measured by positron emission tomography.," *British journal of pharmacology*, vol. 116, no. 1, pp. 1649–55, Sep. 1995.

[4]   H. Hong, G. W. Severin, Y. Yang, J. W. Engle, Y. Zhang, T. E. Barnhart, G. Liu, B. R. Leigh, R. J. Nickles, and W. Cai, "Positron emission tomography imaging of CD105 expression with 89Zr-Df-TRC105.," *European journal of nuclear medicine and molecular imaging*, vol. 39, no. 1, pp. 138–48, Jan. 2012.

[5]   S. R. Cherry, J. A. Sorenson, and M. E. Phelps, *Physics in Nuclear Medicine*, 3rd ed. Philadelphia: Saunders, 2003.

[6]   H.-P. Schlemmer, B. J. Pichler, R. Krieg, and W.-D. Heiss, "An integrated MR/PET system: prospective applications.," *Abdominal imaging*, vol. 34, no. 6, pp. 668–74, Nov. 2009.

[7]   H. Peng, W. B. Handler, T. J. Scholl, P. J. Simpson, and B. a. Chronik, "Proof-of-principle study of a small animal PET/field-cycled MRI combined system using conventional PMT technology," *Nuclear Instruments and Methods in Physics Research Section A: Accelerators, Spectrometers, Detectors and Associated Equipment*, vol. 612, no. 2, pp. 412–420, Jan. 2010.

[8]   H. Zaidi and A. Del Guerra, "An outlook on future design of hybrid PET/MRI systems.," *Medical physics*, vol. 38, no. 10, pp. 5667–89, Oct. 2011.

[9]   G. F. Knoll, *Radiation Detection and Measurement*, 3rd ed. New York: John Wiley and Sons, Inc., 2000.

[10]   C. Pepin, P. Bérard, and A. Perrot, "Properties of LYSO and recent LSO scintillators for phoswich PET detectors," *IEEE Transactions on Nuclear Science*, vol. 51, no. 3, pp. 789–795, 2004.

[11] E. V. D. van Loef, P. Dorenbos, C. W. . . van Eijk, K. W. Kramer, and H. U. Gudel, "Scintillation properties of LaBr 3: Ce 3+ crystals: fast, efficient and high-energy-resolution scintillators," *Nuclear Instruments and Methods in Physics Research Section A: Accelerators, Spectrometers, Detectors and Associated Equipment*, vol. 486, pp. 254–258, 2002.

[12] I. Valais, C. Michail, and S. David, "Comparative Investigation of Ce3+ Doped Scintillators in a Wide Range of Photon Energies Covering X-ray CT, Nuclear Medicine and Megavoltage," *IEEE Transactions on Nuclear Science*, vol. 57, no. 1, pp. 3–7, 2010.

[13] P. a Dokhale, R. W. Silverman, K. S. Shah, R. Grazioso, R. Farrell, J. Glodo, M. a McClish, G. Entine, V.-H. Tran, and S. R. Cherry, "Performance measurements of a depth-encoding PET detector module based on position-sensitive avalanche photodiode read-out," *Physics in Medicine and Biology*, vol. 49, no. 18, pp. 4293–4304, Sep. 2004.

[14] D. Renker, "Geiger-mode avalanche photodiodes, history, properties and problems," *Nuclear Instruments and Methods in Physics Research Section A: Accelerators, Spectrometers, Detectors and Associated Equipment*, vol. 567, no. 1, pp. 48–56, Nov. 2006.

[15] B. Dolgoshein, V. Balagura, P. Buzhan, M. Danilov, L. Filatov, E. Garutti, M. Groll, a. Ilyin, V. Kantserov, V. Kaplin, a. Karakash, F. Kayumov, S. Klemin, V. Korbel, H. Meyer, R. Mizuk, V. Morgunov, E. Novikov, P. Pakhlov, E. Popova, V. Rusinov, F. Sefkow, E. Tarkovsky, and I. Tikhomirov, "Status report on silicon photomultiplier development and its applications," *Nuclear Instruments and Methods in Physics Research Section A: Accelerators, Spectrometers, Detectors and Associated Equipment*, vol. 563, no. 2, pp. 368–376, Jul. 2006.

[16] I. Britvitch, Y. Musienko, and D. Renker, "Investigation of a photon counting avalanche photodiode from Hamamatsu photonics," *Nuclear Instruments and Methods in Physics Research Section A: Accelerators, Spectrometers, Detectors and Associated Equipment*, vol. 567, no. 1, pp. 276–280, Nov. 2006.

[17] P. S. Marrocchesi, M. G. Bagliesi, K. Batkov, G. Bigongiari, M. Y. Kim, T. Lomtadze, P. Maestro, F. Morsani, and R. Zei, "Active control of the gain of a Silicon PhotoMultiplier," *Nuclear Instruments and Methods in Physics Research Section A: Accelerators, Spectrometers, Detectors and Associated Equipment*, vol. 602, no. 2, pp. 391–395, Apr. 2009.

[18] C. R. Crowell, "Temperature Dependence of Avalanche Multiplication in Semiconductors," *Applied Physics Letters*, vol. 9, no. 6, p. 242, 1966.

[19] S. Cherry and M. Dahlbom, *PET: physics, instrumentation, and scanners*. New York, NY: Springer Science, 2006.

[20] J. Huizenga, S. Seifert, F. Schreuder, H. T. van Dam, P. Dendooven, H. Löhner, R. Vinke, and D. R. Schaart, "A fast preamplifier concept for SiPM-based time-of-flight PET

detectors," *Nuclear Instruments and Methods in Physics Research Section A: Accelerators, Spectrometers, Detectors and Associated Equipment*, Nov. 2011.

[21]   H. S. Yoon, G. B. Ko, S. Il Kwon, C. M. Lee, M. Ito, I. Chan Song, D. S. Lee, S. J. Hong, and J. S. Lee, "Initial results of simultaneous PET/MRI experiments with an MRI-compatible silicon photomultiplier PET scanner.," *Journal of nuclear medicine : official publication, Society of Nuclear Medicine*, vol. 53, no. 4, pp. 608–14, Apr. 2012.

[22]   G. Llosa, N. Belcari, and M. Bisogni, "Energy, timing and position resolution studies with 16-pixel silicon photomultiplier matrices for small animal PET," *IEEE Transactions on Nuclear Science*, vol. 56, no. 5, pp. 2586–2593, 2009.

[23]   S. Seifert, H. T. Van Dam, R. Vinke, P. Dendooven, H. Löhner, F. J. Beekman, S. Member, and D. R. Schaart, "A Comprehensive Model to Predict the Timing Resolution of SiPM-Based Scintillation Detectors : Theory and Experimental Validation," vol. 59, no. 1, pp. 190–204, 2012.

[24]   V. Popov, "Advanced data readout technique for Multianode Position Sensitive Photomultiplier Tube applicable in radiation imaging detectors," *Journal of Instrumentation*, vol. 6, no. 01, pp. C01061–C01061, Jan. 2011.

[25]   V. Popov, S. Majewski, and B. L. Welch, "A novel readout concept for multianode photomultiplier tubes with pad matrix anode layout," *Nuclear Instruments and Methods in Physics Research Section A: Accelerators, Spectrometers, Detectors and Associated Equipment*, vol. 567, no. 1, pp. 319–322, Nov. 2006.

[26]   S. Majewski, J. Proffitt, and A. Stolin, "Development of a ' Resistive ' Readout for SiPM Arrays," *2011 IEEE Nuclear Science Science Symposium Conference Record*, vol. 9059, pp. 3939–3944, 2011.

[27]   Y. Wang, Z. Zhang, D. Li, B. Wang, L. Shuai, B. Feng, P. Chai, S. Liu, H. Tang, T. Li, Y. Liao, X. Huang, Y. Chen, Y. Liu, Y. Zhang, and L. Wei, "Design and performance evaluation of a compact, large-area PET detector module based on silicon photomultipliers," *Nuclear Instruments and Methods in Physics Research Section A: Accelerators, Spectrometers, Detectors and Associated Equipment*, vol. 670, pp. 49–54, Apr. 2012.

[28]   S. Siegel, R. W. Silverman, and S. R. Cherry, "Simple charge division readouts for imaging scintillator arrays using a multi-channel PMT," *IEEE Transactions on Nuclear Science*, vol. 43, no. 3, pp. 1634–1641, Jun. 1996.

[29]   T. Y. Song, H. Wu, S. Komarov, S. B. Siegel, and Y.-C. Tai, "A sub-millimeter resolution PET detector module using a multi-pixel photon counter array.," *Physics in medicine and biology*, vol. 55, no. 9, pp. 2573–87, May 2010.

[30]   T. Nakamori, T. Kato, J. Kataoka, T. Miura, H. Matsuda, K. Sato, Y. Ishikawa, K. Yamamura, N. Kawabata, H. Ikeda, G. Sato, and K. Kamada, "Development of a gamma-ray imager

using a large area monolithic 4 × 4 MPPC array for a future PET scanner," *Journal of Instrumentation*, vol. 7, no. 01, pp. C01083–C01083, Jan. 2012.

[31]   M. Janecek, J. Walder, and P. McVittie, "A High-Speed Multi-Channel Readout for SSPM Arrays," *IEEE transactions on nuclear science*, vol. 59, no. 1, pp. 13–18, 2012.

[32]   T. Xu, P. Fan, T. Ma, S. Wang, Z. Deng, L. Lu, and Y. Liu, "Design and initial performance evaluation of a novel PET detector module based on compact SiPM arrays," *2011 IEEE Nuclear Science Symposium Conference Record*, pp. 3038–3041, Oct. 2011.

[33]   C.-Y. Liu and A. Goertzen, "Evaluation of the SensL SPMMatrix for use as a detector for PET and gamma camera applications," *2011 IEEE Nuclear Science Symposium and Medical Imaging Conference*, 2011.

[34]   A. L. Goertzen, M. M. McClarty, C. J. Thompson, F. Retiere, P. Kozlowski, L. Ryner, G. Storz, and V. Sossi, "Evaluation of a Resistor Network Charge Division Multiplexing Circuit for a 16 Pixel SiPM Array," in *2011 IEEE Nuclear Science Symposium and Medical Imaging Conference*, 2011.

[35]   J. Hancock and C. J. Thompson, "Evaluation of an instrument to improve PET timing alignment," *Nuclear Instruments and Methods in Physics Research Section A: Accelerators, Spectrometers, Detectors and Associated Equipment*, vol. 620, no. 2–3, pp. 343–350, Aug. 2010.

[36]   G.-C. Wang, "Timing Optimization of Solid-State Photomultiplier Based PET Detectors," *IEEE Transactions on Nuclear Science*, vol. 57, no. 1, pp. 25–30, Feb. 2010.

[37]   A. Kolb, E. Lorenz, M. S. Judenhofer, D. Renker, K. Lankes, and B. J. Pichler, "Evaluation of Geiger-mode APDs for PET block detector designs.," *Physics in medicine and biology*, vol. 55, no. 7, pp. 1815–32, Apr. 2010.